



MASTERARBEIT

In-depth analysis of T cell receptor dynamics and intra-complex interactions

Ausgeführt am Institut für
Angewandte Physik
der Technischen Universität Wien

unter der Anleitung von

Univ. Prof. Dipl.-Ing. Dr.techn. Gerhard Schütz
Dipl.- Ing. Benedikt Rossboth

durch

Carina Marie Viehböck, BSc.

02. Mai 2018

Eidesstattliche Erklärung

Ich erkläre, dass die vorliegende Arbeit nach den anerkannten Grundsätzen für wissenschaftliche Abhandlungen von mir selbstständig erstellt wurde. Alle verwendeten Hilfsmittel, insbesondere die zugrunde gelegte Literatur, sind in dieser Arbeit genannt und aufgelistet. Die aus den Quellen wörtlich entnommenen Stellen, sind als solche kenntlich gemacht.

Das Thema dieser Arbeit wurde von mir bisher weder im In- noch Ausland einer Beurteilerin/einem Beurteiler zur Begutachtung in irgendeiner Form als Prüfungsarbeit vorgelegt. Diese Arbeit stimmt mit der von den Begutachterinnen/Begutachtern beurteilten Arbeit überein.

Carina Marie Viehböck, BSc.

Wien, Mai 2018

Acknowledgements

First of all, I would like to thank the whole biophysics group, especially my advisor, Gerhard Schütz, for giving me the opportunity to join his team and work on this project. I am grateful for his insights during the lab meetings and for his comments on this manuscript. His enthusiasm and his immense knowledge have inspired me and showed me how fulfilling working in science can be.

My sincere thanks also goes to Benedikt Rossboth, who taught me much of what I know about single particle tracking, diffusion analysis and cell transfections. He was always there to answer my questions and help me with my experiments when I ran into a troubles. His guidance helped me during my research and writing of this thesis.

A very special gratitude goes to Elena Parkinson for her assistance in the cell culture and to my fellow lab student Joschka Hellmeier who helped me a lot with the micropatterning experiments. I would like to acknowledge Mario Brameshuber for offering valuable advice and always finding the time to discuss my work progress.

A big thank you also goes to the team of MUW for providing murine T cells for the experiments.

Last but not least, I express profound gratitude to my family and to my boyfriend Tom for providing unfailing support and continuous encouragement throughout the years of my study and through the process of composing this thesis.

Abstract

The T cell receptor (TCR) is the key membrane protein that participates in the activation of T cells in response to the recognition of antigens presented by the major histocompatibility complex (pMHC) on the membrane of antigen presenting cells. This binding process is likely to depend on the dynamics of the participating membrane proteins, making the analysis of their diffusion an important task for studying TCR–pMHC interaction. The previously described low mobility of the TCR ($D \sim 0.05 \mu\text{m}^2/\text{s}$) might impair the efficiency of TCR–pMHC engagement, encouraging the task to verify if the slow mobility is indeed inherent to T cells or if it results from external cell treatments required for microscopy approaches.

In this work, single molecule tracking experiments were performed to investigate to which degree the diffusion behavior of the TCR is affected by different experimental conditions. Tracking experiments were done using fluorescently labelled anti-TCR β single chain fragments (scF $_V$) derived from the monoclonal antibody H57. Three different strategies for presenting adhesive surfaces to T cells were compared: (i) the homo-polymer Poly-D-Lysine, (ii) the glycoprotein Fibronectin and (iii) a supported lipid bilayer presenting intercellular adhesion molecule 1 (ICAM-1). Furthermore, Highly Inclined and Laminated Optical Sheet (HILO) microscopy was utilized to compare the diffusion on the apical membrane to the results derived from Total Internal Reflection (TIR) imaging on the basal T cell membrane. To further exclude fluorophore influences on the diffusion measurements, scF $_V$ were conjugated to varying organic dyes and the diffusion results were compared.

Similar diffusion characteristics of the TCR were found on all three coated surfaces, with D ranging from $0.03 - 0.06 \mu\text{m}^2/\text{s}$. Also, different fluorophores attached to the scF $_V$ or the usage of full antibodies instead of the single chain fragment yielded similar results. Furthermore, TCR mobility at the top membrane measured via HiLO microscopy was similar to the mobility at the bottom membrane measured via TIRF microscopy. From this data we conclude that there is no direct influence of the adhesive surfaces on the mobility of the TCR.

In the second part of this work the interaction kinetics of the ζ - and TCR β subunits of the TCR/CD3 complex were measured using different imaging modalities. Recent measurements have indicated discrepancies in the dynamic behavior of these components, reporting a faster diffusion for ζ . To address these findings, diffusion properties were obtained from single particle tracking experiments, and further investigated by combining in vivo micropatterning with Fluorescence Recovery after Photobleaching (FRAP). The diffusion analysis of the tracking measurements hints to a more mobile ζ -chain, highlighting the possibility of TCR/CD3-independent ζ within the T cell membrane. Evaluation of the signal recovery curve from the FRAP experiments indicates a stable interaction between TCR/CD3 subunits. While the FRAP results do not represent a more mobile ζ chain, they also do not exclude the existence of free membrane-bound ζ .

Kurzfassung

Der T Zell Rezeptor (TCR) ist ein membrangebundener Proteinkomplex, der an der Aktivierung von T Zellen beteiligt ist. Antigene werden auf Histokompatibilitätskomplex-Molekülen (pMHC) präsentiert, welche sich auf der Membran von antigenpräsentierenden Zellen befinden. Die Erkennung von Antigenen durch den TCR führt zu einer Interaktion zwischen TCR und pMHC. Dieser Prozess kann von der Dynamik der beteiligten Membranproteine beeinflusst werden, weswegen die Diffusionsanalyse der Proteine eine wichtige Rolle für die Untersuchung der TCR-pMHC Interaktion spielt. Die geringe Mobilität des TCR ($D \sim 0.05 \mu\text{m}^2/\text{s}$) kann die Effizienz der TCR-pMHC-Interaktion beeinträchtigen. Es ist zu überprüfen, ob die niedrige Mobilität für T Zellen charakteristisch ist oder ob sie aus externen Zellbehandlungen resultiert, die für mikroskopische Ansätze erforderlich sind.

In dieser Arbeit wurden Einzel-Molekül-Tracking Experimente durchgeführt, um das Diffusionsverhalten des TCR unter verschiedenen experimentellen Bedingungen zu untersuchen. Tracking-Experimente wurden mit fluoreszenzmarkierten anti-TCR β scFv-Fragmenten durchgeführt und es wurden drei verschiedene Adhäsionsflächen für T Zellen verglichen: (i) das Homopolymer Poly-D-Lysine, (ii) das Glykoprotein Fibronectin und (iii) eine Lipid-Doppelschicht die interzelluläre Zelladhäsionsmoleküle (ICAM-1) aufweist. Darüber hinaus wurde die HILO-Mikroskopie (Highly Inclined and Laminated Optical Sheet) verwendet, um die Diffusion auf der apikalen Membran mit den Ergebnissen der internen Totalreflexionsfluoreszenzmikroskopie (TIRF) auf der basalen T Zellmembran zu vergleichen. Um Einflüsse von Fluorophoren auf die Diffusion auszuschließen, wurden die scFv-Fragmente mit unterschiedlichen organischen Farbstoffen konjugiert und die Diffusionsergebnisse analysiert.

Ähnliche Diffusionseigenschaften des TCR wurden auf allen drei beschichteten Oberflächen mit einer Diffusionskonstante D im Bereich von $0.03 - 0.06 \mu\text{m}^2/\text{s}$ gemessen. Messungen mit verschiedenen Fluorophoren und auch die Verwendung von Vollantikörpern anstelle des scFv-Fragments führten zu ähnlichen Ergebnissen. Die TCR-Mobilität, die mittels HILO-Mikroskopie gemessen wurde, war mit jener mittels TIRF-Mikroskopie vergleichbar. Aus diesen Daten kann geschlossen werden, dass es keinen direkten Einfluss der Adhäsionsflächen auf die Mobilität des TCR gibt.

Im zweiten Teil dieser Arbeit wurde die Interaktionskinetik der ζ - und TCR β Untereinheiten des TCR/CD3-Komplexes mit verschiedenen Methoden gemessen. Bei vorhergehenden Messungen wurden Diskrepanzen im dynamischen Verhalten dieser Komponenten beobachtet und eine schnellere Diffusion für ζ festgestellt. Um diese Diffusionsunterschiede zu untersuchen, wurden Diffusionseigenschaften aus Einzelpartikel-Tracking-Experimenten ermittelt. Weiters wurde die Micropatterning-Technik mit FRAP (Fluorescence Recovery after Photobleaching) kombiniert um die Interaktionskinetik zu bestimmen. Die Diffusionsanalyse deutet auf eine mobilere ζ -Kette hin, die auf die Existenz einer TCR/CD3-

Komplex unabhängigen ζ -Kette innerhalb der Membran weisen könnte. Messungen des Verlaufs der Fluoreszenzintensität über der Zeit aus den FRAP Experimenten deuten auf eine stabile Wechselwirkung zwischen den TCR/CD3-Untereinheiten, schließen aber die Existenz von freien membrangebundenen ζ -Ketten nicht aus.

Contents

1	Introduction.....	9
1.1	Motivation.....	9
1.2	The immune system.....	10
1.2.1	TCR/CD3 complex.....	11
1.2.2	TCR/CD3 complex assembly and expression.....	12
1.2.3	T cell activation.....	14
1.3	Seeing single molecules.....	16
1.3.1	Basics of light microscopy.....	17
1.3.2	Fluorescence microscopy.....	18
1.3.3	Total Internal Reflection Fluorescence Microscopy.....	24
1.3.4	Adhesion surfaces.....	25
1.3.5	Highly Inclined and Laminated Optical sheet illumination.....	28
1.4	Resolution limit.....	28
1.5	Membrane Dynamics.....	29
1.5.1	The composition and organization of the plasma membrane.....	29
1.5.2	Methods to determine diffusion.....	31
1.5.3	Diffusion Analysis from SPT.....	35
2	Materials & Methods.....	40
2.1	Cell Culture.....	40
2.1.1	Transformation of E. coli and Midi Preparation.....	40
2.1.2	T cell Transduction.....	41
2.2	Sample preparation.....	42
2.2.1	Labelling.....	42
2.2.2	Surface preparation.....	42
2.3	Setup.....	44
2.4	Single particle tracking.....	45
2.4.1	Image recording.....	45
2.4.2	Diffusion Data Analysis.....	45
2.5	FRAP experiments.....	46
2.5.1	FRAP data analysis.....	47
3	Results.....	48
3.1	TCR diffusion analysis.....	48
3.1.1	Different t_{lag} measurements.....	48
3.1.2	TCR β diffusion on different adhesion surfaces.....	49
3.1.3	Labelling strategies.....	53
3.2	Interaction kinetics between TCRβ and ζ.....	58
3.2.1	Diffusion properties of ζ	58
3.2.2	Micropatterning & FRAP.....	62
4	Conclusion.....	66
4.1	TCR diffusion analysis.....	66
4.1.1	Surfaces.....	66
4.1.2	Diffusion on the basal and apical membranes of T cells.....	67
4.1.3	Fluorophores.....	68
4.1.4	Label Proteins.....	69
4.2	Interaction kinetics between TCRβ and ζ.....	69

4.2.1	Diffusion analysis	69
4.2.2	Micropatterning and FRAP	70
5	List of Figures	72
6	References	73

1 Introduction

1.1 Motivation

Adaptive immune responses are initiated after T cell receptor (TCR) recognition of antigens presented by the major histocompatibility complex (pMHC) on the membrane of antigen presenting cells (APC) [1]. The conjugation between T cells and APC initiates the movement of TCR, adhesion proteins and costimulatory receptors towards the T cell-APC contact site forming a signaling area at the interface, known as the immunological synapse ([2], [3]).

The reported slow diffusion rate of membrane proteins, including the TCR, has been contributed to various interactions with molecular structures in the crowded membrane environment ([4],[5]). Many studies have investigated mechanisms governing membrane protein kinetics, revealing the dependency of TCR mobility on intracellular Ca^{2+} concentration and on associations to the actin cytoskeleton [5]. While important biological aspects of the diffusion mechanisms have been investigated using single-molecule fluorescence imaging, it is still unclear to which extent the molecular behavior is affected by the imaging conditions.

Over the past decade, a variety of different techniques have been developed to adapt quantitative microscopic analysis for addressing the kinetic processes governing the plasma membrane [6]. The different technical realizations of membrane experiments deviate in sample preparation approaches, image acquisition techniques and data analysis possibilities, raising the question if the heterogeneous protein dynamics could also be attributed to external cell treatments [7].

Since there is a variety of different cell preparation strategies available for examining protein dynamics on plasma membranes, it should be questioned whether some of the applied treatments could affect the diffusional behavior and therefore alter the experimental outcome.

In Total Internal Reflection Fluorescence (TIRF) microscopy molecules at the cell surface are visualized at the interface between cell and glass substrate, a region where they might be exposed to additional interactions with the external environment, including the adhesion surface of the coverslip used for sample mounting. Recent studies have observed immobilizing effects of commonly used adhesion coatings on the TCR, possibly perturbing the diffusional behavior and organization of the signaling proteins and receptors [8]. In addition, the type of fluorescence labelling strategy used to measure diffusion properties may affect membrane constituents or surface treatment material, influencing the actual protein mobility and therefore leading to unrepresentative results ([9], [10]).

A common approach to study the diffusion of the TCR/CD3 complex is through visualization of its subunits, often fusing the ζ chain to a fluorescent protein. However, the association of ζ and the TCR/CD3 complex is still to be elucidated, since recent studies report the existence of independent ζ expressed within the T cell membrane [11]. A faster diffusion has been

observed for ζ compared to TCR β , supporting the existence of a free membrane-bound ζ [12].

Furthermore, a rapid turnover of ζ independent of the TCR/CD3 complex was observed, suggesting a more dynamic interaction between ζ and the remaining TCR/CD3 components [11].

In this work single particle tracking combined with total internal reflection fluorescence microscopy was applied to study the molecular behaviour of the TCR at the basal cell membrane when exposed to different experimental arrangements, i.e. the presence of an adhesion surface. In addition, different labelling strategies were tested to investigate possible interactions influencing TCR mobility.

The second part of this work attempts to study ζ behavior by comparing its diffusion characteristics and interactions with the more stable TCR β unit of the TCR/CD3 complex. Single particle tracking experiments were performed to access dynamic information, comprising the diffusion coefficients, diffusion modes and mobile fractions of these two TCR/CD3 subunits.

Additionally, the micropatterning technique combined with fluorescent recovery after photobleaching (FRAP) was performed as an approach to further investigate the interaction kinetics of the TCR/CD3 complex and ζ .

For better understanding of the experimental and analytical procedures presented in this work, the following sections provide an overview of the structure and function of the TCR/CD3 complex in the T cell membrane environment, as well as the physical background of the imaging techniques applied to visualize them. The theoretical part is followed by the presentation of the experimental strategies, the outcome and analysis of the performed measurements.

1.2 The immune system

The immune system's ability for detecting and reacting to pathogens and cellular abnormalities is orchestrated by a variety of different cell types. Depending on the recognition and triggered defence mechanisms, the immune response can be categorized into the innate or the adaptive immune system. The innate immune system provides a general, fast and non-specific defence against pathogens. A more specific reaction is governed by the adaptive immune system, where B- and T lymphocytes target specific pathogens. When B lymphocytes (B cells) are activated they secrete antibodies, also called immunoglobulins, which specifically bind to foreign antigens that initially stimulated their production. Antibodies neutralize the harmful effects of pathogens, by blocking their ability to bind to receptors on host cells [13].

The basic building blocks of antibodies are two identical pairs of polypeptide chains consisting of a heavy and light subunit. Figure 1 illustrates how these structures are held

together by disulphide bonds, forming a flexible Y-shape that is structured by a stem and two arms, termed Fragment antigen binding (Fab) fragments, when isolated from the whole antibody. The polypeptide chains can functionally be separated into variable heavy and light (VH/VL) domains located at the tips of the Fab fragments and constant heavy and light (CH/CL) domains, which comprise the area of the stem and bottom part of the arms. The constant region is fairly similar within all classes of antibodies, whereas the variable part features structural variation among B cells allowing numerous antigens to be identified [14]. The specific and noncovalent binding of antibodies to antigens is a trait that is widely used in biological sciences and fluorescence microscopy.

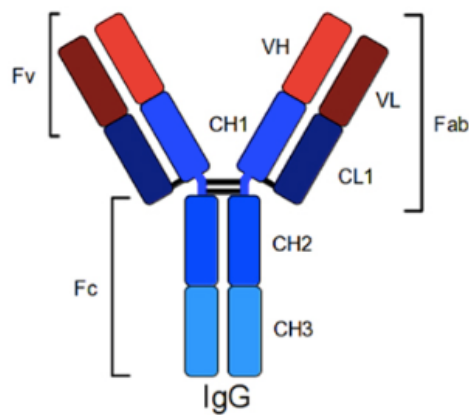


Figure 1: Depiction of a full size antibody: CH, constant heavy chain; CL, constant light chain; IgG, immunoglobulin, VH, variable heavy chain; VL, variable light chain [15].

The other important unit participating in the protective immune mechanism are T lymphocytes (T cells) which control the cell-mediated immune response. T cells react by either directly eliminating the virus-infected-host cell or by producing signal molecules that activate other cell types to destroy it. A defining structure of T cells is the T cell receptor (TCR) which has evolved to recognize foreign peptide fragments displayed on antigen presenting cells (APCs).

1.2.1 TCR/CD3 complex

The TCR/CD3 complex is formed by eight transmembrane proteins, comprising TCR $\alpha\beta$, CD3 $\epsilon\gamma$, CD3 $\epsilon\delta$ heterodimers, and a ζ homodimer (Figure 2). The majority of T cells expresses TCRs composed of α and β heterodimeric polypeptide chains, while a smaller fraction is formed by TCR γ and TCR δ chains [16]. In the scope of this work only the TCR $\alpha\beta$ will be discussed and analysed in detail.

The TCR $\alpha\beta$ chains are covalently linked together by a disulphide bond and are structured in an antibody-like extracellular domain, a transmembrane part and a short intracellular segment. Both polypeptides contain a constant and a variable region, displaying structural similarity to the Fab fragment of antibodies (Figure 2). The constant region is membrane

bound, while the variable region extends extracellularly and functions as binding site for antigens, determining antigen specificity. This arrangement is responsible for the recognition of peptide antigens presented by major histocompatibility complex (MHC) molecules expressed on the surface of APCs (antigen presenting cells) (Figure 2). Due to its short intracellular tail the TCR $\alpha\beta$ lacks intracellular signalling domains and is therefore not directly involved in signal transduction. Only through the TCRs constitutive association with the CD3 complex, consisting of CD3 $\epsilon\gamma$, CD3 $\epsilon\delta$, and $\zeta\zeta$ dimers can intracellular signalling and therefore T cell activation be initiated. These transmembrane peptides contain immunoreceptor tyrosine-based activation motives (ITAMs) that confer intracellular signal propagation [17].

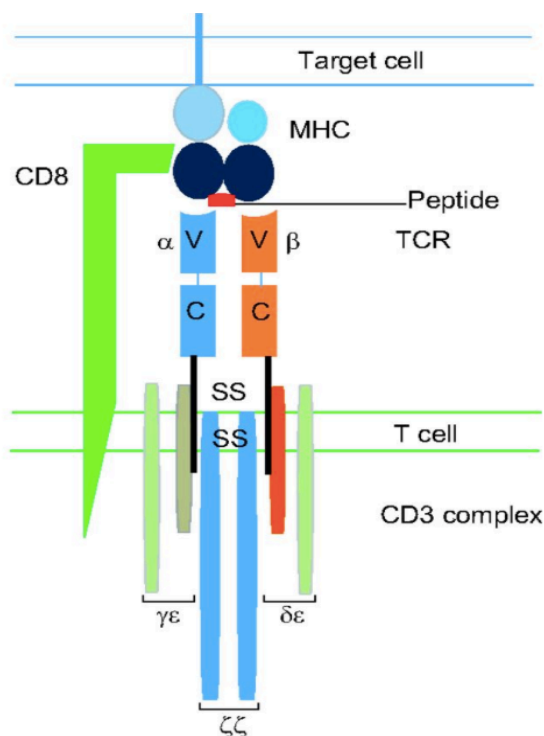


Figure 2: Structure and organization of the TCR/CD3 complex proteins, composed of an extracellular domain, a transmembrane region and a cytoplasmic tail where the immunoreceptor tyrosine activation motifs (ITAMs), responsible for intracellular signalling, are located. 'S' symbolizes the disulphide bonds. Interaction of the TCR through the co-receptors CD8 (or CD4) with the target peptide sequence of an antigen presented by the major histocompatibility complex (MHC) [18].

1.2.2 TCR/CD3 complex assembly and expression

For a T cell mediated immune response, the components of the TCR/CD3 complex must first be synthesized, assembled and properly expressed on the plasma membrane to form a functional unit.

The process begins with the synthesis of TCR α , TCR β , CD3 ϵ , CD3 γ and CD3 δ subunits, which are translocated to the endoplasmic reticulum (ER), where partial complexes of TCR $\alpha\beta$ and CD3 $\epsilon\gamma$ or CD3 $\epsilon\delta$ heterodimers are formed (Figure 3). After a retention period in the ER these partly assembled proteins reach the Golgi apparatus where they are completed by

association with the ζ molecules. Contrary to the other subunits, ζ is not retained in the ER and progresses to the Golgi apparatus independently. The formation of the TCR/CD3 complex is driven by ionic interaction between complementary charges residing on amino acid residues in the transmembrane segments of the CD3, ζ and TCR $\alpha\beta$ (Figure 3) [19]. Only full complexes are thought to be able to leave the Golgi apparatus and are stably expressed as functional receptors on the plasma membrane of T cells [20].

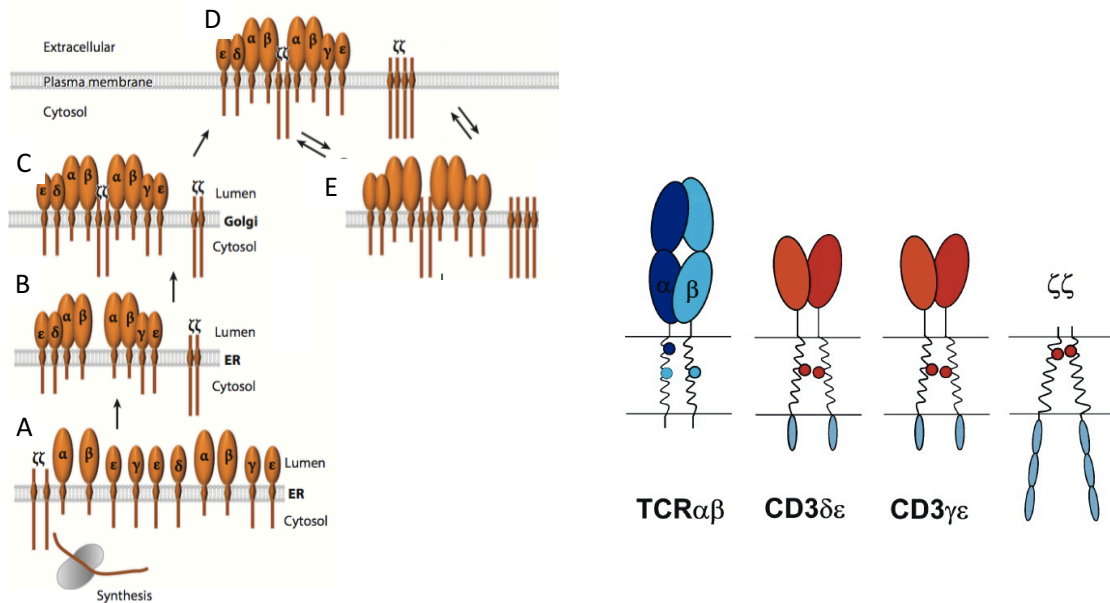


Figure 3: Left images: Synthesis and assembly of the TCR/CD3-complex on the plasma membrane. Image modified from [16]. A: TCR/CD3 subunits (except for ζ) are synthesized and translocated to the ER. B: Partial complexes form in the ER and can progress to the Golgi apparatus where ζ joins them. C: Full complexes can be delivered and stably expressed on the membrane. D: Stably expressed TCR/CD3 complex on the cell surface. Contrary to the other subunits, ζ can be independently expressed on the plasma membrane. E: TCR/CD3 complexes undergo cycles of endocytosis. Right image: Three basic residues are found in the TM domains of the TCR $\alpha\beta$ heterodimer (blue dots) while a pair of acidic residues is present in each of the three associated signalling dimers (red dots) [19].

At the cell surface TCR $\alpha\beta$ and $\zeta\zeta$ dimers are covalently linked by disulphide bonds. The other subunits are not covalently linked but stably associated, in contrast to TCR $\alpha\beta$ which features a weaker interaction with CD3 $\epsilon\gamma$, CD3 $\epsilon\delta$ or $\zeta\zeta$ dimers. Contributing to this destabilizing effect is the fact that $\zeta\zeta$ can be expressed independently at the plasma membrane and experiences a shorter half-life than the other subunits resulting in a faster turnover within the membrane. Satoru Ono et al [11] reported that $\zeta\zeta$ rapidly exchanges with newly synthesized $\zeta\zeta$, suggesting that this single component in a multi-subunit receptor exhibits independent transportation and association-dissociation dynamics from the rest of the complex. Additionally, ζ chains are more likely to be observed in endosomal compartments compared to the other TCR/CD3 constituents [16].

The ζ chain is built of a short extracellular domain, a transmembrane region and a long cytoplasmic tail (Figure 3) featuring three ITAMs and three basic-rich sequences (BRS) instead of a single copy as on the other CD3 subunits (Figure 4). Interestingly, in the resting TCR the CD3 ϵ and ζ ITAMs have been proposed to be in tight contact with the inner leaflet of the plasma membrane and to detach upon TCR ligation [21].

These findings support the idea of a more independent ζ /TCR/CD3 association which functional relevance has not been discovered yet.

1.2.3 T cell activation

It is the cooperation of several T cell receptor constituents that triggers the activation of T cells, generating an immune response.

In contrast to immunoglobulins which interact directly with free pathogens, the TCR/CD3 complex only recognizes peptide fragments that are associated with Major Histocompatibility Complex (MHC) molecules, displayed on the surface of antigen presenting cells (APC) (Figure 2). Functionally, T cells can be discriminated into two major classes, which are distinguished by the expression of the transmembrane glycoproteins CD4 and CD8. During antigen recognition, depending on the type of T cell, the TCR associates with MHC molecules through the co-receptors CD4 or CD8. They differ in their interaction with the two MHC classes, CD4 binding to MHC class II and CD8 connecting to MHC class I molecules. CD4 is present in T-helper cells where the response leads to the activation of other effector cells including macrophages, B cells and dendritic cells. CD8 receptors are found on cytotoxic T cells, which are specialized to destruct any cell that they specifically recognize [22].

Binding of the TCR complex to peptide-MHC molecules induces the formation of microclusters at the T cell-APC interface, defined as the immunological synapse. This engagement results in the transmission of an intracellular signal governed by the CD3-subunit, initiating T cell activation [16].

Figure 4 illustrates the main steps leading to the activation of T cells. Ligation of the TCR complex triggers the phosphorylation of the ITAMs, a process that is mediated by the lymphocyte cell-specific protein tyrosine kinase (Lck) which is a protein associated with the cytoplasmic tails of the CD4 and CD8 co-receptors. Lck is recruited to the engaged TCR/CD3 complex, where it phosphorylates the ITAMs of the ζ and CD3 subunits. This triggers the recruitment and binding of ζ -chain-associated protein kinase 70 (ZAP-70) to the doubly phosphorylated ITAMs where consequently ZAP-70 itself is phosphorylated by Lck. In turn, ZAP-70 phosphorylates the transmembrane adaptor LAT, which recruits the scaffold protein SLP-76 and the phospholipase C- γ (PLC- γ). The activation of PLC- γ allows downstream transmission of signalling by controlling the production of second messengers such as diacylglycerol and free intracellular calcium (Ca^{2+}) ([23], [24]).

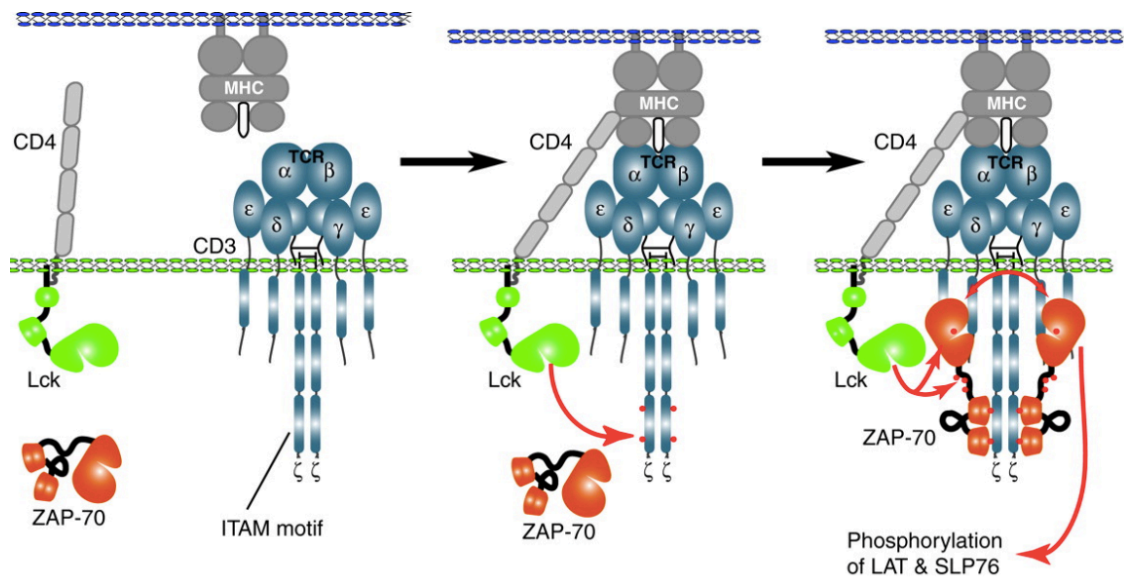


Figure 4: T cell activation. Interactions between the TCR and the peptide-MHC results in the activation of CD4 (or CD8) –associated Lck which is recruited to the proximity of the cytoplasmic domains of CD3 complex where it phosphorylates the ITAMs. The red dots portray phosphorylated ICAMs. The doubly phosphorylated ζ ITAMs interact with ZAP-70, which is then also phosphorylated by Lck, leading to the activation of ZAP-70. Active ZAP-70 subsequently phosphorylates LAT and SLP-76, which recruit many other signalling molecules and lead to T-cell activation, proliferation, and differentiation (not shown) [25].

In the resting state of the TCR BRS motifs bear a positive charge which promote association of the cytoplasmic CD3 and ζ domains with the negatively charged phospholipids in the inner leaflet of the plasma membrane (Figure 5). This configuration of the CD3 and ζ tails impedes ITAM phosphorylation by preventing Lck access. Several theories have been proposed to explain the mechanisms that regulate the interaction of the CD3 and ζ tails with the membrane. Some studies suggest that TCR engagement induces dissociation of the CD3 and ζ ITAMs from the membrane and therefore makes them more approachable for Lck, enhancing phosphorylation (Figure 5A) [26]. Alternatively, ITAMs are speculated to be in a more dynamic equilibrium between the membrane and cytosol and upon TCR ligation and Lck activation phosphorylated ITAMs are no longer capable of associating with the membrane [27] (Figure 5B). Another theory proposes that initial signalling in a small number of TCRs leads to a local Ca^{2+} release which modulates the charge property of lipids causing membrane dissociation of the CD3 and ζ tails in unengaged TCRs [28]. The resulting enhanced accessibility of ITAMs to Lck leads to a ligand independent phosphorylation (Figure 5C).

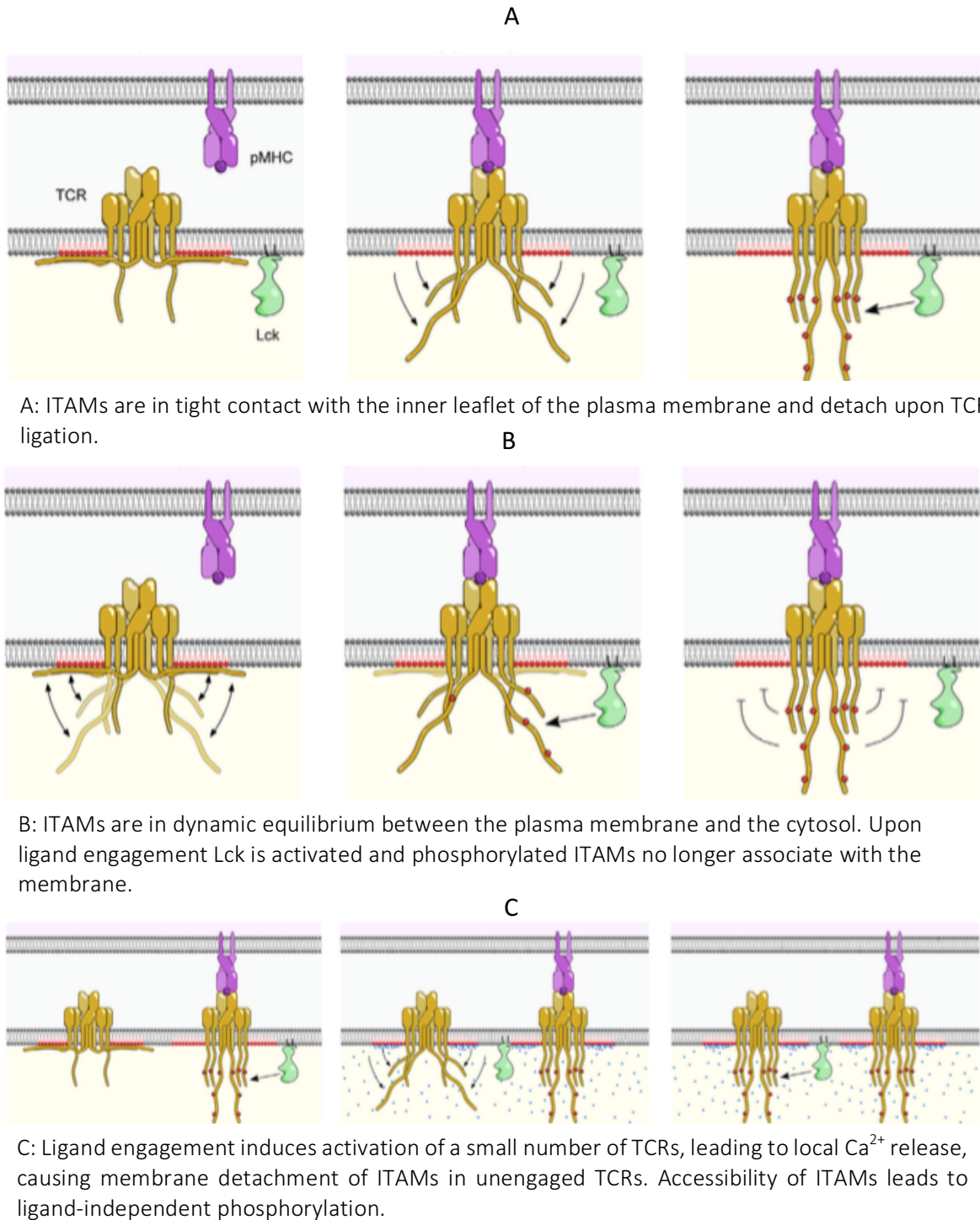


Figure 5: Effects of membrane charges on TCR signalling [29].

1.3 Seeing single molecules

With the invention of the light microscope tiny structures previously invisible to the human eye have become visible. Over the last couple of years many different imaging techniques have emerged, providing ways to see inside the cell, allowing scientists to observe molecules in motion and follow the actions of proteins.

1.3.1 Basics of light microscopy

The optical microscope is a system of lenses that produces a magnified image of a small object, allowing us to extend our vision into the microsphere. Light is diffracted by the structures of the illuminated specimen, where small structural details result in a wider diffraction angle.

The structural and functional principles are illustrated in Figure 6, showing a modern infinity microscope that consists of an objective lens, a tube lens and an eyepiece lens. The specimen is located at the front focal plane of the objective lens so that when light is diffracted by the structures it passes through the objective lens and leaves it as parallel rays. The space between the objective and the tube lens provides a path of parallel light where additional optical elements can be placed. The parallel light is collected and converged by the tube lens, producing an image at the intermediate image plane. The magnification of the image in the intermediate plane is given by the focal lengths of the two lenses:

$$M = \frac{f_{tl}}{f_{obj}} \quad (1)$$

This intermediate image can further be magnified by the eyepiece lens on to the observer's retina. In modern microscopy systems, light is detected directly by cameras such as Electron Multiplying Charge-Coupled Devices (EMCCD), thus omitting the eyepiece.

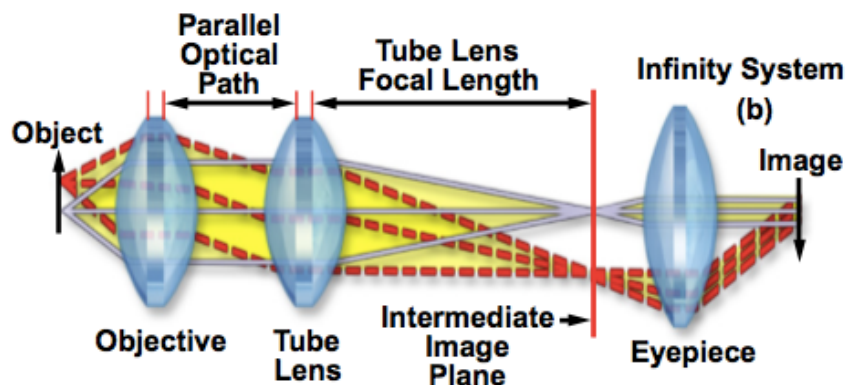


Figure 6: In the imaging process the objective system collects light rays from each point on the object and converges them to a single point at the intermediate image plane. By further passing through the eyepiece the resulting magnified image can be visualized on to the observer's retina [30].

Another defining feature of the objective is the numerical aperture (NA) which determines the objective's capacity to collect light (Figure 7). Emitted light that does not reach the objective causes a loss of image detail, which leads to an impaired spatial resolution. The NA is therefore an important measure of the microscope's resolving power given by:

$$NA = n \sin \alpha \quad (2)$$

Its value depends on the refractive index n of the medium in which the sample is immersed in and on α , the one-half angular aperture of the objective.

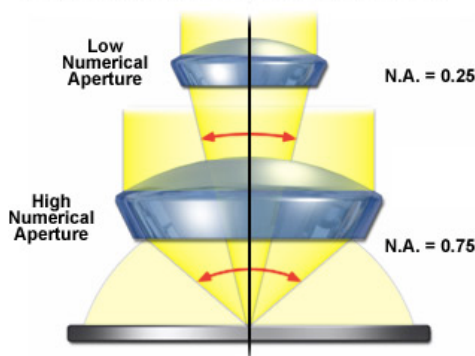


Figure 7: Objective numerical aperture comparison [31]. A higher NA is capable of collecting more light, thus improving spatial resolution.

1.3.2 Fluorescence microscopy

Much of our knowledge regarding biological processes and structures at the cellular and subcellular level has come from the ability to directly visualize them [32]. In biological and medical sciences, fluorescence microscopy is a widely used method that enables the observation of specific cell components through molecule-specific labelling and using light microscopy. Contrast is generated by the emission of light by fluorescently labelled probes, while the background remains dark.

The observation of fluorescent molecules (fluorophores) is based on the absorption and subsequent emission of light, a transition which happens in the timescale of nanoseconds. This process is frequently illustrated by the Jablonski energy diagram which is presented in Figure 8A. The diagram shows the distinct energy levels involved in the absorption ($h\nu_{ex}$) and emission ($h\nu_{em}$) of light by a fluorophore, where the singlet ground state (S_0), as well as the first excited singlet states (S_1 , S_1') are illustrated as horizontal lines. When light from an external source is absorbed by the fluorophore in the ground state (S_0), the molecule reaches a higher energy state (S_1). This excitation process requires the wavelength of the illuminating light source to be within the potential electronic transition energies of the molecule. The fluorophore can leave the excited energy state by the emission of photons. In the Jablonski diagram the transition between energy states associated with absorption or emission of a photon are represented by the straight vertical arrows.

During the molecule's relaxation process from the excited to the ground state, vibrational energy is dissipated, allowing the fluorophore to enter a relaxed excited state (S_1). This loss in energy shifts the emission spectrum to longer wavelengths, a phenomenon defined as Stokes' Law, which describes the difference in maximum excitation and emission wavelengths. Figure 8B demonstrates the spectral shift towards longer wavelengths, also showing a lower intensity peak for the fluorophore emission than for the absorption curve. With an increasing Stokes' shift the overlap between the excitation and emission wavelength is minimized, increasing the detected signal. By additionally inserting optical filter combinations the separation of excitation from emission light can be enhanced and therefore a maximum fluorescence intensity achieved [33].

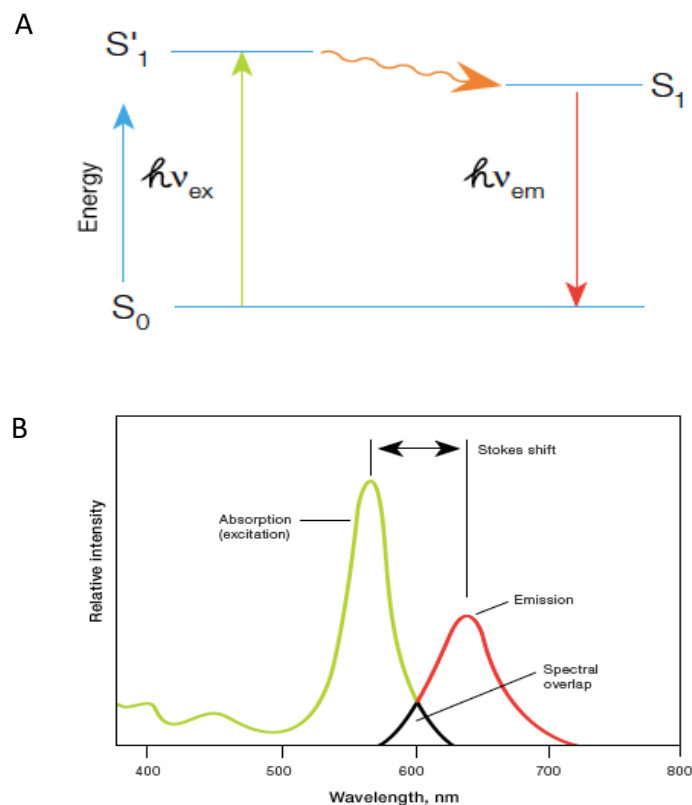


Figure 8: The principle of fluorescence microscopy. A: Fluorescence Jablonski Diagram, describing the excitation and emission energies of fluorophores B: Excitation and emission spectra plotting the fluorescence intensity of a fluorophore over the range of excitation/emission wavelengths. Stokes shift: emitted photons are of lower energy than the excitation light, resulting in a shift the maximum wavelengths [124].

Conventional fluorescence microscopy is limited by relatively low spatial resolution because of the diffraction of light. The resolution limit of about ~ 200 nm in lateral direction and ~ 500 nm along the optic axis is larger than many subcellular structures, leaving them too small to be observed in detail [34].

1.3.2.1 Fluorescent labels

Today, there is a variety of different approaches available to label proteins for fluorescence microscopy, and choosing the proper method depends on the experimental requirements. In single particle tracking (SPT) the molecule of interest is attached to a fluorophore and its emission is observed over a certain time. These experiments often face the challenges of coping with fluorophore bleaching and detecting weak signals above background noise due to cellular autofluorescence, which degrade temporal resolution and spatial localization accuracy. Low photobleaching rates would allow for longer observation times, enabling a better classification of the dynamic system. Therefore, high brightness and photostability are essential characteristics for fluorescent labels to ensure successful applications of Single Particle Tracking (SPT) experiments. High fluorophore brightness is caused by a high extinction coefficient which describes its capacity to absorb light and enter the excited state, and by a high quantum yield defined as the ratio of emitted photons compared to the number of absorbed ones [35]. Another important fluorophore characteristic is the fluorescence lifetime which specifies the average time the molecule spends in the excited state. For single molecule imaging, short lifetimes (<5ns) are preferable since they increase the number of excitation and emission cycles, therefore providing a greater number of photons to be detected [36].

However, not only the photophysical properties can influence the measurement outcome, but also the differences in physical and chemical structures between various fluorophores could lead to different diffusion results. The size, the electric charge and the hydrophobicity of fluorophores conjugated to biological targets can alter the target's mobility and ability to interact with its environment [37]. Single molecule tracking data is often acquired with total internal reflection microscopy, where the cell membrane at the interface with the adhesion surface is imaged. Large fluorophores could affect the structure and biological function of the labelled protein, resulting in an altered diffusion rate. The electrostatic interaction between the fluorophores and charged cell structures or applied adhesion surfaces could cause unspecific binding and disturbances in the natural state of the protein of interest. It is therefore important that a fluorophore is specific to its target to minimize artefacts in the data obtained from single molecule images. Recent studies have investigated the effects of a fluorophore's hydrophobicity, reporting that hydrophobic organic dyes show much higher non-specific binding to cell adhesion surfaces ([9], [38], [10]). Fluorophores bound to the coated coverslips introduce misleading emitted signals which could mistakenly be identified as immobile membrane-bound targets.

The influence on the quality of the SPT data of both the chemical and the optical properties of the fluorescent probe requires a careful choice of fluorophore according to the biological process being investigated.

Fluorescent proteins:

It was in the early 1960s when the Green Fluorescent Protein (GFP) was discovered and

extracted from jellyfish. The discovery that this protein can be genetically encoded to the biomolecule of interest has led to its use for fluorescent investigations in living cells. With this fusion method external cell modifications are avoided and the addition of a specificity module which attaches the label to the biomolecule of interest is not needed. This is considered to be the most specific labelling technique, resulting in relatively low background signal. Today there is a variety of GFP mutants, including the Yellow Fluorescent Protein (YFP), photo-switchable Cyan Fluorescent Protein 2 (PS-CFP2), Enhanced GFP (EGFP) and many more [39]. However, fluorescent proteins, such as the green fluorescent protein (GFP), are larger than organic dyes (~27 kDa [40]) making them more likely to perturb the activity of the protein under study.

Organic dyes:

An advantage of organic fluorophores is their high brightness and small structure (~1-2nm, ~0.2-1 kDa [41]), allowing their attachment to a variety of molecules including proteins [42], antisense DNA strands [43], mRNA [44], polymer chains [45], and antibodies [46], making them suitable candidates for single particle tracking measurements. Common methods to couple organic dyes to the proteins of interest include protein tags or antibodies (see 1.3.2.2).

The large supply of different organic dyes offers a variety of spectral characteristics but also comes with a diversity of physiochemical and photophysical properties, differing in brightness, photostability, electrostatic charge and hydrophobicity [38]. Table 1 presents some characteristics of dyes used in this work. Dyes which are excited by blue light, such as Alexa Fluor 488, tend to be smaller and more charged than red dyes, such as Abberior STAR 635 [38].

Properties of organic dyes

Properties	Alexa Fluor 488	Alexa Fluor 555	Abberior STAR 635	Alexa Fluor 647
λ_{\max} excitation [nm]	490	555	635	665
λ_{\max} emission [nm]	525	580	655	650
Fluorescence lifetime [ns]	4.1	0.3	2.8	1.0
Quantum yield	0.92	0.10	0.88	0.33
Net Charge	-3.94	-	0	-
Polarity	polar	-	polar	-
Hydrophobicity [LogD]	-8.02	-	0.58	-3.72
Data Sources	[47], [48], [38], [49]	[47], [48], [49]	[50], [38]	[47], [48], [38], [49]

Table 1: Properties of some organic dyes. There are differences in the net molecular charges and hydrophilicities of Alexa 488 and Abberior STAR635. Hydrophobicity is expressed by the log of the distribution coefficient which is a measure of the expected ratio of dye concentrations in water and a non-polar solvent (octanol) [38]. Molecules with a negative value of logD (e.g. Alexa Fluor 488) are hydrophilic whereas molecules with a positive logD are more hydrophobic.

The near-infrared silicon-rhodamine (SiR) fluorophore features high photostability, allowing its use for SPT experiments. SiR can be coupled specifically to intracellular proteins in live cells by using different labelling techniques such as SNAP-tag [51].

1.3.2.2 Labelling strategies

The visualization of cellular components can be realized by coupling a fluorophore to a specific ligand which is attached to the molecular structure of interest. This can be realized in different forms, such as using antibodies or protein tags to link the target molecule with a fluorophore.

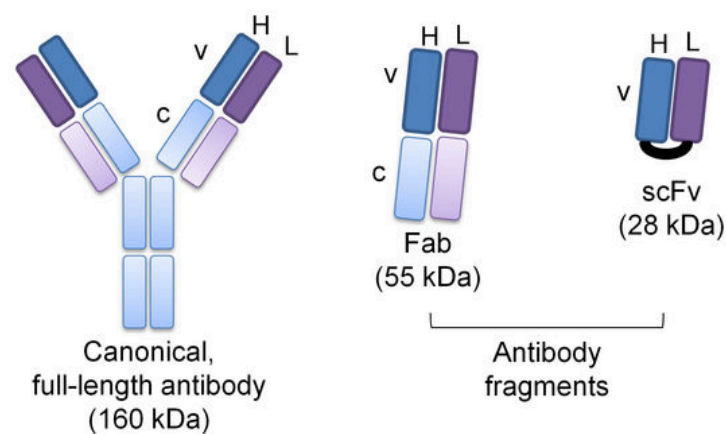


Figure 9: Comparison of a full antibody and various antibody fragment types. CH, constant heavy chain; CL, constant light chain; Fab, antigen binding fragment; scFv, single chain variable fragment, VH, variable heavy chain; VL, variable light chain [52].

Immunofluorescence:

The specific binding ability of antibodies can be employed in many biological applications in fluorescent microscopy to target and label antigens within cells by coupling a fluorescent tag to the antibody.

This imaging technique is known as immunofluorescence, where the fluorophore is either conjugated directly to a primary antibody or to a secondary antibody directed against the species of the primary antibody (Figure 10).

Different antibody-related ligands can be synthesized by chemical or genetic mechanisms, producing smaller fragments with the same specific antigen recognition function. This is realized in form of Fabs or single chain fragments variable (scFv), which are recombinant

antibody fragments consisting of a variable light chain (VL) covalently connected to a variable heavy chain (VH) (Figure 9) [14].

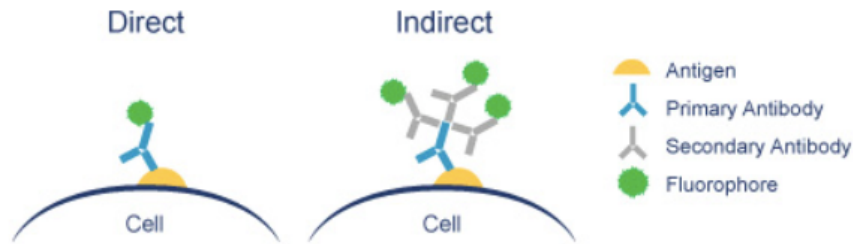


Figure 10: Direct and indirect labelling of antibodies. Fluorophores can either be conjugated to a primary antibody which is directed against a target, or via a secondary antibody directed against the species of the primary antibody [53].

Protein tags:

Another labelling approach includes protein tags such as Halo [54], SNAP [55], and CLIP [56]. The most versatile of these tags is the SNAP-tag, a 20kDa mutant of the DNA repair protein O6-alkylguanine-DNA alkyltransferase that can be fused to any protein of interest. It reacts specifically with benzylguanine derivatives (Figure 11), enabling a specific and covalent attachment of the SNAP-tag with a fluorescent probe [57]. Proteins expressed as SNAP-tag fusions can be tagged with suitable fluorescent molecules such as the biocompatible fluorophore silicon–rhodamine (SiR) fluorophore [51].

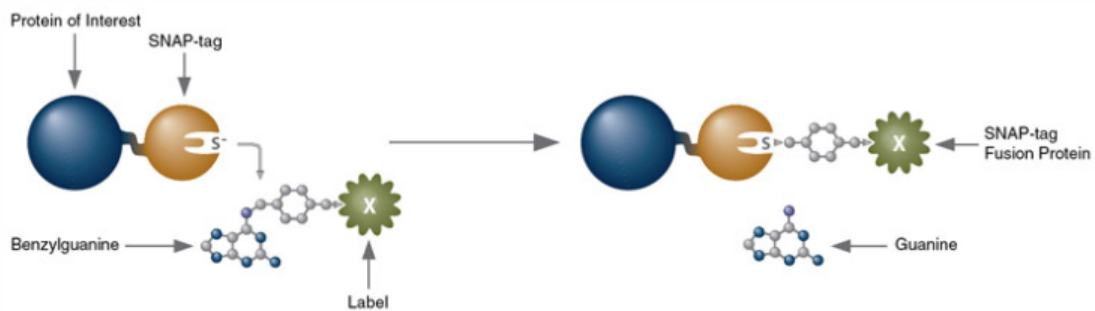


Figure 11: SNAP-tag fused to the protein of interest forms covalent bond with benzylguanine – containing “X” label releasing guanine [57].

When analyzing the dynamic properties of membrane proteins, it is important to consider the functional effects of attaching a linking molecule to a membrane protein. Featuring the same antigen recognition function, single chain fragment variable (scFv) and antibodies differ in their structural appearance. ScFv are characterized by a small size with a molecular weight of approximately 28 kDa whereas antibodies are much larger molecules weighing up to 160 kDa [52]. This enhanced structure might lead to a slowing down of protein diffusion and stronger interaction with the membrane environment and glass substrate. Furthermore, the labelling technique needs to be specific to its target to minimize artefacts

due to unspecific binding (e.g. to other membrane structures) in the data obtained from single molecule diffusion experiments.

1.3.3 Total Internal Reflection Fluorescence Microscopy

Total Internal Reflection Fluorescence Microscopy (TIRFM) is a wide-field illumination technique often employed in fluorescence microscopy applications to improve the signal-to-noise ratio by minimizing background signals. This imaging modality is based on the total reflection of excitation light at the interface between two media featuring different refractive indices (n_1 and n_2), whenever the light beam travels from medium of high refractive index to a medium of lower refractive index (Figure 12 B). The refractive behaviour of light at this contact area is described by Snell's law:

$$n_1 \sin \theta_1 = n_2 \sin \theta_2 \quad (3)$$

with θ_1 and θ_2 being the two respective angles to the surface normal.

Above the critical angle θ_c the angle of refraction exceeds 90° , and total internal reflection occurs, a phenomenon that depends on the refractive indices of the two media. An evanescent field is generated at the interface between the two media, with an intensity that exponentially decreases with distance from the interface. By extending less than hundred nanometre into the specimen, this illumination technique suppresses unwanted background fluorescence from the out of focus plane and therefore improves the signal-to-noise ratio.

Using this method, experiments can be designed to investigate molecular structures on membranes of cells that are adherent to the cover glass. The technique is realized by shifting the position of the excitation laser towards the rim of the objective at its back focus. In this way fluorophores that are located on the surface-adherent plasma membrane can be excited by the evanescent field and fluorescence from these emitters can be collected by the microscope optics without perturbation by cytosolic fluorescence.

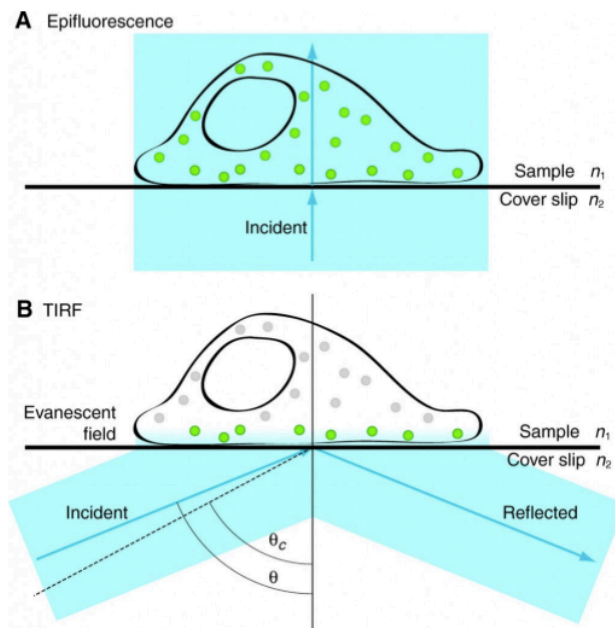


Figure 12: Illumination techniques. A: illumination scheme of Epifluorescence. B: The basic concept of total internal reflection fluorescence: With adjustment of the laser excitation incidence angle to a value greater than the critical angle, the illuminating beam is totally reflected and an evanescent field is generated in the specimen medium immediately adjacent to the interface. The fluorophores nearest to the glass surface are selectively excited by interaction with the evanescent field, minimizing background noise [58].

1.3.4 Adhesion surfaces

Total internal reflection microscopy is often applied in single molecule studies to visualize fluorescent membrane constituents at the coverslip and basal cell surface. An important prerequisite for performing microscopic measurements on cells is the proper attachment of the specimen, commonly realized by pre-treating glass coverslips. The composition of the adhesion surface is crucial for the cells' ability to attach, but the nature of the material could also interfere with membrane dynamics. Surface interactions caused by electrostatic charges or binding to external molecular structures could perturb the mobility and function of the protein of interest, yielding misleading fluorescent signals ([8], [9]). The chemical and physical composition of the adhesion materials could trigger reactions with the used fluorophores, affecting the measured diffusion coefficients and mobile populations, two important parameters for tracking experiments.

In this study four commonly used strategies for presenting adhesion surfaces to T cells are examined in their influence on the mobility of the TCR and will be further discussed.

1.3.4.1 Poly-D-Lysine

Poly-D-Lysine (PDL) and Poly-L-Lysine (PLL) are positively charged polymers that are commonly used in biological experiments to enhance cell adhesion to glass surfaces [59]. Both molecules provide a positive charge to the otherwise negatively charged glass slide and

therefore the cell attachment is formed by the electrostatic attraction of the positively charged PDL-/PLL-coated glass slide and the negatively charged glyocalix at the plasma membrane. In this case, cells are immobilized through Coulomb forces, hence the attachment to the glass surface is non-specific to any cellular constituents [60]. The main difference between PDL and PLL is that PDL precursors are artificial products, while PLL precursors occur naturally. PDL is therefore resistant to enzymatic degradation whereas PLL is affected by proteases released by cells which might lead to an impaired cell adherence [61].

1.3.4.2 Fibronectin

Fibronectin is often used for enhancing cell adhesion to glass substrates. The cell attachment to a Fibronectin-coated surface is mediated by integrins which are specific transmembrane glycoproteins that bind to special binding sites known as the RGD-sequence (Arginylglycylaspartic acid) of Fibronectin molecules ([62], [63]). Hence, cell adhesion is formed by a more specific interaction with the coating material, as opposed to the less specific attraction of charges based on PDL/PLL substrates.

1.3.4.3 Supported lipid bilayer with ICAM-1

The formation of supported lipid bilayers is based on the fusion of liposomes with the glass coverslip and provides a more physiological adhesion surface for cells [64]. This method requires the use of adhesion molecules to anchor cells to the surface for imaging. When imaging T cells the intercellular adhesion molecule 1 (ICAM-1) is incorporated in the supported lipid bilayer and cells adhere to the surface by specific binding to this ligand. The integrin LFA-1, expressed on T cells, interacts with ICAM-1, providing a specific cell attachment [65].

1.3.4.4 Micropatterning

Micropatterning methods can be used in biological research to gain insight into interaction mechanisms of membrane proteins. By seeding cells on patterned surfaces their response to specific environmental and molecular cues can be studied. This technique enables the detection of protein-protein interactions on cell membranes by combining micro-structured surfaces with fluorescence microscopy. The idea is to enrich membrane proteins in specific patterns within the plasma membrane on live cells, by using patterned glass surfaces with a bound ligand to the protein of interest. While there are different methods to realize patterns on cell surfaces, such as photolithography and soft lithography, all require adhesion proteins to mediate cellular attachment [66]. In this work microcontact printing, a form of soft lithography, will be discussed in more detail. This method utilizes polydimethylsiloxane (PDMS) polymer stamps featuring patterns with different sizes and shapes. The stamp is

immersed into a solution of the material of interest and then stamped to a substrate to transfer the material to the substrate.

Schwarzenbacher et al described a method to characterize interactions between fluorescently labelled membrane molecules, acting as 'prey' and 'bait', in live cells [67].

Antibodies acting as specific ligands ('bait') to the fluorescently labelled membrane proteins ('prey') are arranged in micropatterns on the glass surface, where the intermediate gaps are passivated. When cells expressing the prey proteins are plated on such surfaces, the prey will follow the antibody distribution in case of interaction between bait and prey. For strong interactions a pronounced co-patterning of the fluorescent prey can be observed whereas no interaction yields a homogenous prey distribution. In addition, micropatterned surfaces provide a beneficial addendum to FRAP experiments which can extract information on the interaction dynamics of both proteins [68] (Figure 13).

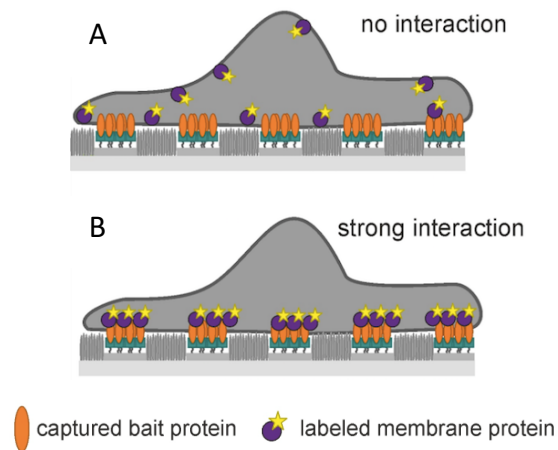


Figure 13: Schematic representation of the micropatterning principle [69]. A: No interaction between bait and fluorescently labelled prey proteins. B: Strong interaction between proteins.

1.3.5 Highly Inclined and Laminated Optical sheet illumination

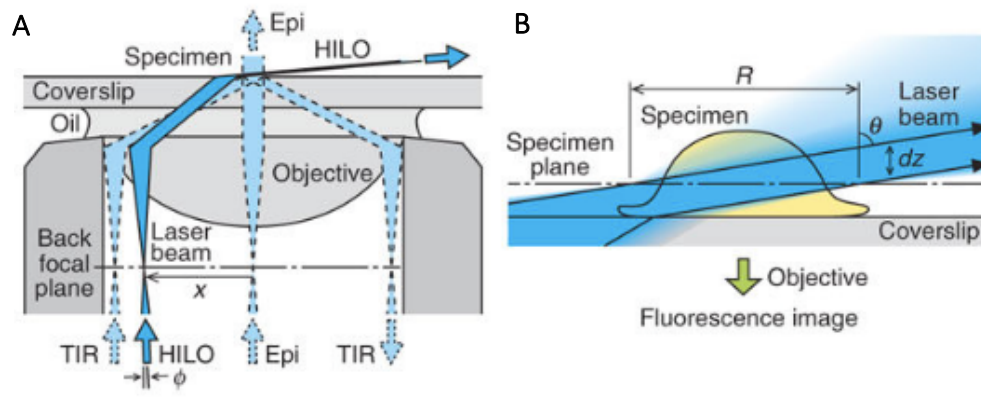


Figure 14: Highly Inclined and Laminated Optical sheet illumination. A: Realization principle of HiLO compared to TIRF and Epi illumination. B: Optical sectioning of a cell using a highly inclined laser beam [125].

To visualize single molecules on regions, more distant to the basal adhesion surface of the cell, an excitation method called Highly Inclined and Laminated Optical (HiLO) sheet illumination can be applied. An axially thin light sheet is realized by adjusting the position of the incident laser beam, yielding a large angle of refraction (Figure 14A). This imaging technique enables single molecule observation with reduced background fluorescence since only a single plane of the cell is being illuminated (Figure 14B).

1.4 Resolution limit

Resolution is defined as the minimal distance between two points that can still be distinguished by an observer or camera system as separate entities. Due to the diffraction pattern of an object point and the finite size of the objective's aperture not all diffracted waves from the object can be transmitted, leading to a loss of high-frequency spatial information. As a result, the object point is blurred into a finite sized spot featuring a characteristic diffraction profile (Figure 15B). The intensity distribution of this smeared-out spot is described by the point spread function (PSF) and its analytical derivation, the Airy function.

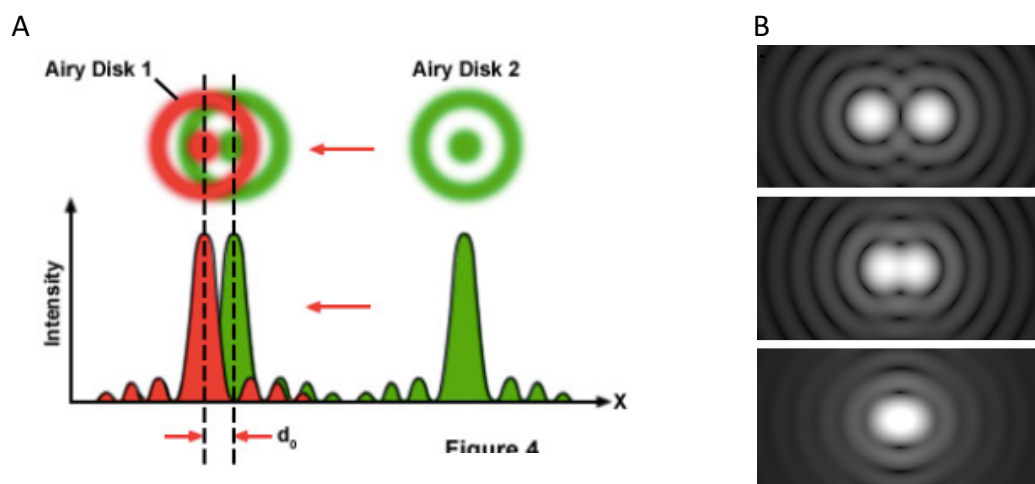


Figure 15: The image is represented by point light sources that appear as Airy diffraction patterns at the microscope's intermediate image plane. A: According to the Rayleigh criterion, the two point sources (green and red) presented by their PSF and Airy functions are resolvable when the first diffraction minimum of one image point coincides with the maximum of the other [70]. B: The upper image shows two objects whose Airy discs are sufficiently far apart to be resolved. The image in the middle represents the Rayleigh criterion. As the objects are placed closer together, the resulting diffraction patterns merge and become non-resolvable (bottom image) [71].

The minimum distance two points need to have to still be resolvable can be determined by:

$$d = \frac{0.61 \cdot \lambda}{n \sin \alpha} = \frac{0.61 \cdot \lambda}{NA} \quad (4)$$

Equation (4) presents the Rayleigh criterion of resolution which relates the resolving limit of a microscope (d) with the wavelength of light (λ) used to illuminate the sample and the numerical aperture (NA) of the objective lens (Figure 15A). For a conventional light microscope with an NA of 1.4 and visible light illumination ($\lambda = 460 \text{ nm}$) the resulting resolution reaches $\sim 0.2 \text{ }\mu\text{m}$. This resolution boundary becomes an obstacle when studying subcellular structures which are smaller than the wavelength of visible light and therefore aren't resolvable with conventional microscopy.

1.5 Membrane Dynamics

1.5.1 The composition and organization of the plasma membrane

The performance of the adaptive immune system is based on the efficiency of molecular responses at a cellular level. Many cellular functions such as T cell signalling are regulated

by membrane associated proteins and their cooperation and interaction with other functional subunits of the cell ([72], [73]). The dynamic organization of cellular components on the plasma membrane is essential for immunological processes since it provides the interface where many transmembrane signal transduction events occur [29].

Reaction kinetics form the physical basis of intermolecular protein-binding interactions, and require several membrane constituents to come together [74]. At low protein concentrations, the probability of two proteins associating with each other increases with their lateral diffusion rate, since proteins fixed at random locations on the plasma membrane have little chance for meeting. It is in this context that the diffusion modes and kinetics of membrane proteins direct their functions and studying these lateral diffusion behaviour leads to a better understanding of subcellular actions [75].

Different factors are believed to govern the diffusion mechanisms of membrane constituents. For one, the environment of the cell surface appears to have an impact on protein mobility. The plasma membrane is a complex and dynamic system organized by various lipids and proteins, probing the cell surface [76]. The "*fluid mosaic*" model by Singer and Nicolson describes the plasma membrane as a homogenous fluid bilayer of phospholipids, mosaicked with freely diffusing proteins [77] (Figure 16). Over the past two decades however, numerous studies have corrected this simple picture of the membrane by observing how the distribution of membrane constituents shapes a highly heterogeneous and crowded environment [78].

Interactions with structures from the environment can affect protein diffusion, giving rise to different modes of lateral membrane mobility which deviate from free Brownian motion, as predicted by the "*fluid mosaic*" model. Studies have reported a lower protein diffusion rate on the cell surfaces compared to synthetic membranes [4]. Binding events with anchored membrane and cytoskeletal components can induce a constraining effect to confine the diffusion of membrane proteins. As a result of the crowded membrane conditions, anomalous lateral diffusion has been observed ([79], [80]). Possible mechanisms underlying the diffusion properties of membrane proteins and receptors could further be associated with the galectin lattice that cross-links glycoproteins or the activity of the tyrosine kinase domain ([81], [82]). Associations with the actin cytoskeleton or actin binding proteins have been suggested to alter the diffusional behaviour of membrane receptors [5], [83]. When studying T cells a significant decrease of TCR mobility has been observed upon an increase in intracellular Ca^{2+} levels during T cell activation [5]. Recent studies have discussed possible effects of charged membrane domains, formed by an asymmetrical distribution of charged lipids, suggesting that electrostatic interactions influence the actions and function of proteins associated with the charged plasma membrane ([29], [84]). Further, interactions with extracellular matrix proteins or protein complexes on other cells, including receptor-ligand associations, might also modulate the mobility [85].

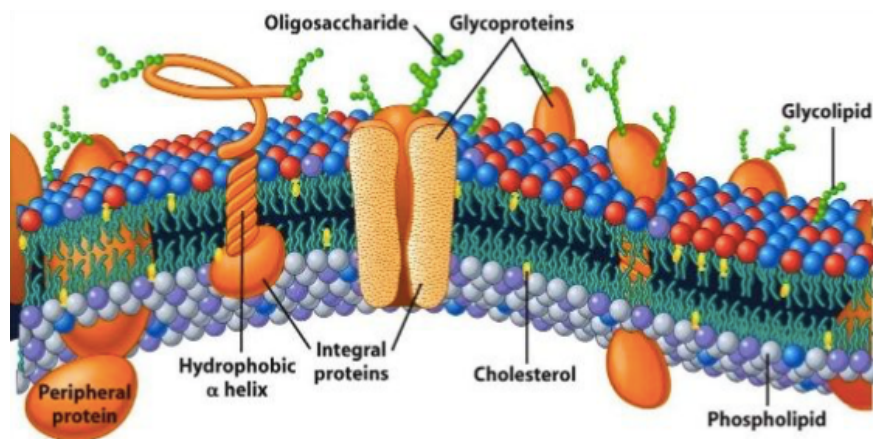


Figure 16: Illustration of the plasma membrane environment according to the “fluid mosaic” model by Singer and Nicolson, revealing the presence of different lipids and proteins. [126]

1.5.2 Methods to determine diffusion

Today there are several microscopy techniques capable of identifying and visualizing the various modes of protein mobility. Amongst these methods are fluorescence recovery after photobleaching (FRAP) and single-particle tracking (SPT).

1.5.2.1 Fluorescence Recovery after Photobleaching (FRAP)

Fluorescence Recovery after Photobleaching (FRAP) is an imaging technique that can provide dynamic information of proteins using fluorescence microscopy ([86], [87]). In this method a high concentration of fluorescently labelled membrane proteins is imaged and a small region of interest (ROI) on the plasma membrane is photobleached (Figure 17A). The recovering fluorescence, mediated by the replacement of the bleached molecules by the unbleached molecules, is monitored using time-lapse imaging. The time-dependence and the intensity of the recovered fluorescent signal (Figure 17B) provide information on the protein’s mobility and can be used to quantify the rate of lateral diffusion and turnover rates. FRAP curves are also a useful tool to determine the mobile and immobile fractions of the molecules under study. A partial recovery of the initial fluorescence is attributed to immobile photobleached molecules, which do not contribute to the recovery signal. To get quantitative information FRAP curves are fitted to appropriate models, yielding the characteristic half time which is the time required for the recovery to reach half of its initial value ([88], [89]).

The FRAP technique can provide millisecond temporal resolution for the collective diffusion of membrane particles but fails to capture the dynamic heterogeneity of individual

membrane proteins. Also, the spatial resolution achievable in FRAP is restricted by the size of the diffracted spot ($\sim 250\text{nm}$), limiting its application for nanoscale processes [90].

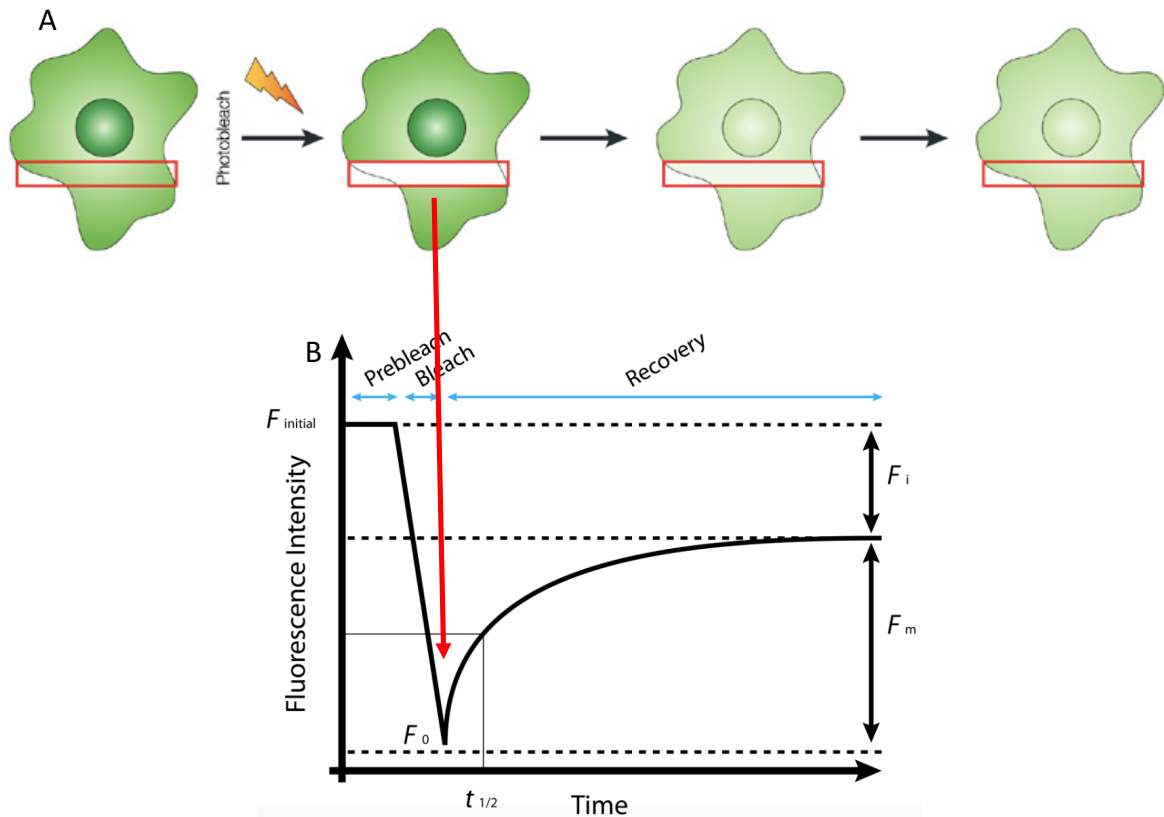


Figure 17: Fluorescence recovery after photobleaching. A: Illustration of a cell expressing fluorescent molecules, which is imaged with low light levels before and after photobleaching the strip outlined in red. Recovery of fluorescent molecules from the surrounding area into the photobleached region is monitored over time [91]. B: The plot shows the fluorescence recovery into the photobleached region as a function of time. F_{initial} is fluorescence intensity before bleaching; F_0 the fluorescence intensity immediately after bleaching; F_m the mobile fraction (fraction that contributes to the recovery); F_i the immobile fraction (fraction that does not contribute to the recovery); $t_{1/2}$ describes half time recovery [92].

1.5.2.2 Single Particle Tracking

Single Particle tracking (SPT) is able to resolve the positions of individual molecules with ~ 10 nm accuracy and a temporal resolution in the milliseconds range, providing access to single molecule behaviour on the cell surface ([90], [93]). Successful application of SPT relies on a low density of fluorescently labelled molecules which are imaged and on capturing their motion in a series of images. Digital image processing methods are applied to reconstruct trajectories from the recorded signals, enabling the analysis of the diffusion of each single particle.

The experimental and theoretical realization of SPT involves:

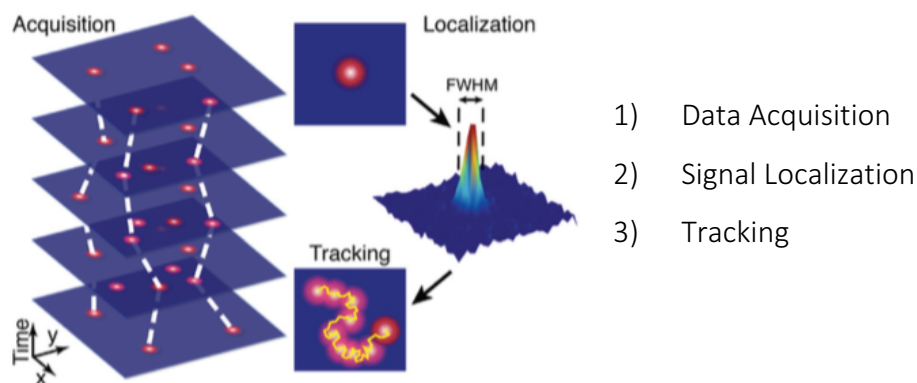


Figure 18: Schematic representation of the three main steps in single particle tracking [94]. A series of images featuring sparsely labelled molecules (red dots) is recorded in acquisition mode. In the localization step the positions of the particles are retrieved which are linked to generate trajectories that describe the motion of the particle.

1) Acquisition:

For SPT acquisition a fluorescent dye is introduced in the probe and its emission is recorded as a time series of images through an optical set up by a high-speed camera. The molecules under study need to be followed over a sufficiently long time, with their track length being reduced by photobleaching of the fluorophores. Introducing only a low density of fluorescently labelled particles allows to resolve each single one (see chapter 1.4) and enables their highly precise localization. While the spatial precision is usually in the order of several nanometres, the temporal resolution is limited by the frame rate of the camera system. Most commonly, wide-field detectors based on charged coupled devices (CCD) are used for signal detection, enabling large data outputs and high sensitivity [95]. For two-dimensional cell membrane studies, the most favourable illumination scheme is based on total internal reflection fluorescence (TIRF) excitation (see chapter 1.3.3).

The acquisition can be influenced by the choice of certain imaging parameters, including the number of frames, illumination and delay time and excitation intensity. The sum of the delay time, the period waited before the next consecutive image is taken, and the illumination time is defined as the time lag which determines the frequency of observation. The selection of the time lag duration enables to study the diffusion at different time scales, but can strongly affect the quantification of diffusion modalities molecules [96]. A long illumination time can result in images with blurred spots formed by the average movement of the molecule during the illumination. On the other hand, too short illumination times decreases the number of collected photons during light exposure, leading to a lower localization precision. One way to compensate the effects of a reduced illumination time is to increase the excitation intensity. However, too high excitation powers can enhance photobleaching resulting in shorter trajectories.

2) Localization:

SPT relies on computer intensive data analysis to find and localize single fluorescent emitters in sometimes very noisy images. After data acquisition the output of a SPT measurement consists of a time-series of diffraction limited images featuring bright spots that correspond to the fluorescent particles. For the assessment of dynamic properties data processing needs to be performed, in order to obtain the particle coordinates which can then further be connected to trajectories. Various localization methods and algorithms are available for this task, which are based on estimating the particle positions in each frame by finding the centre of the point spread function (PSF) [97]. The PSF of an imaging system can be approximated by a Gaussian and commonly used fitting methods include least-squares (LS) and the maximum likelihood estimation (MLE). For LS, the differences between the predicted and the actual signal are calculated, and their squares are summed and minimized. The MLE is the set of parameters, such as coordinates, intensity, background etc. that maximize the likelihood function for a particular spot image, represented by its PSF [98]. The localization of a fluorescent dye cannot be determined with infinite accuracy and the average deviation from the real position is given by the localization error. Optimization of localization methods is crucial to avoid errors in the detection since positional uncertainties might induce artefacts and limitations in the determination of diffusion constants and molecular motion patterns [99].

3) Tracking:

After determining the coordinates in each frame, trajectories are reconstructed by connecting the nearest dots from frame to frame, a process described as tracking or linking. There are different approaches for the linking of localizations, one common realization being the nearest neighbour analysis, which connects respective points by finding the minimum distance in consecutive frames. Improvements to this algorithm are required in the case of absent fluorophores in some frames which result in missing frames within the tracks. In this work a Nearest Neighbour approach with additional options to include gaps within tracks was utilized as described in [100].

Because each particle is monitored individually, SPT can be used to elucidate dynamic heterogeneity within the membrane environment by extracting the lateral diffusion coefficients and modes of motion.

1.5.3 Diffusion Analysis from SPT

An important parameter for characterizing the lateral diffusional motion of a molecule is its diffusion coefficient (D), which can be derived by the diffusion equation of Fick's second law [101]. The solution of Fick's equation corresponds to a Gaussian distribution that broadens symmetrically over time written as:

$$p(x, t)dx = \frac{1}{\sqrt{4\pi Dt}} \cdot \exp\left(-\frac{x^2}{4Dt}\right) dx \quad (5)$$

For a particle that starts moving from a position $\mathbf{x} = 0$ at the starting time $\mathbf{t} = 0$, the probability density function for diffusion describes the probability of finding the particle at a time \mathbf{t} in an interval $[\mathbf{x}, \mathbf{x}+d\mathbf{x}]$. The first moment of the distribution yields the particle's average position, which in the case of random diffusion, would be at its starting point, $\mathbf{x} = 0$. The second momentum is a measure for the width of the Gaussian distribution and corresponds to the mean squared displacement of the particle which gives its average distance from the starting point after a certain time \mathbf{t} :

$$\langle x^2 \rangle = 2nDt \quad (6)$$

The proportionality factor is given by the diffusion coefficient D and the number of dimensions n .

For a particle moving in a two dimensional space (e.g. the plasma membrane) with the coordinates $\mathbf{r} = (\mathbf{x}, \mathbf{y})$, the mean square displacement is given by:

$$\langle r^2 \rangle = 4Dt \quad (7)$$

MSD Analysis

A common approach to extract information from the generated trajectories in single particle tracking experiments is to calculate the mean square displacement (MSD) [102]. Apart from using this method to determine the rate of lateral diffusion, specified as the particle's diffusion coefficient (D), certain modes of motion can be distinguished by their characteristic MSD versus time relationships [101]. These diffusion parameters describe a particles mobility within a specific surrounding, e.g. the cellular membrane.

From a two-dimensional single molecule trajectory, the MSD can be extracted from each track by averaging over the distances measured between discrete time intervals. The MSD is evaluated as a function of time lag (t_{lag}) and the overall observation time. For a diffusing particle whose position \mathbf{x} is captured at n points, the MSD for a single track is calculated according to:

$$\langle r^2 \rangle = MSD_{\Delta t=i} = \frac{1}{n-i} \sum_{t=1}^{n-i} (x_t - x_{t+i})^2 \quad (8)$$

where i gives the size of the introduced gap between consecutive points, determining the distance between the first (or second etc.) and the third (or fourth etc.) position of each track (Figure 19A).

This equation represents the time-averaged MSD, providing temporally averaged information of the diffusion process. This relation is graphically represented in Figure 19B. Each data point in the MSD plot is the averaged displacement over different t_{lag} s and due to the finite trajectory length, less data is available at larger time lags, which could lead to misleading results [103]. Therefore, diffusion parameters should be determined by fitting the MSD curve to the first two time points [104], as the short t_{lag} region provides the most data.

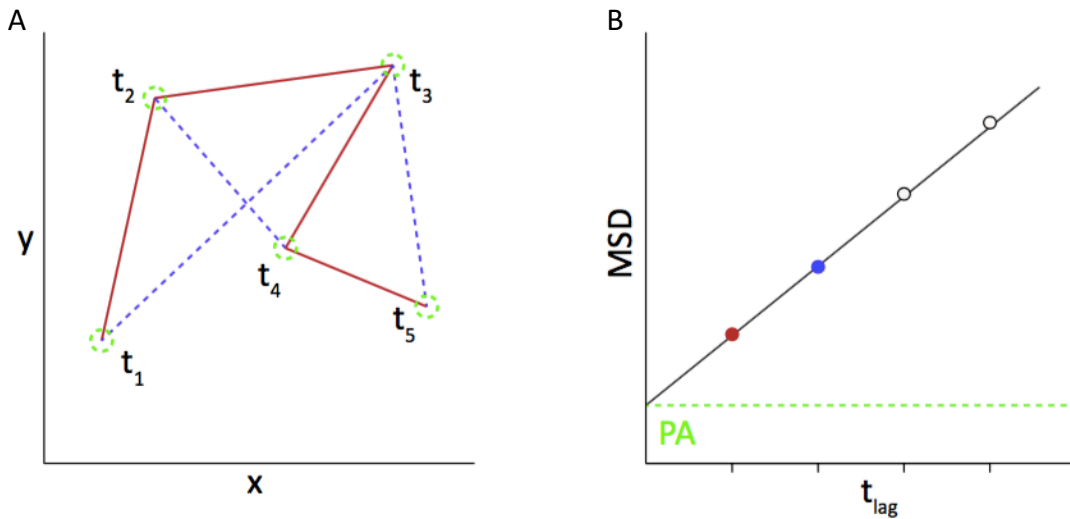


Figure 19: MSD analysis: A: Observations of the single particle positions at different time points t . Continuous red lines indicate the displacement corresponding to single steps, dotted blue lines to double steps during two time intervals. B: Mean squared displacements are plotted according to the t_{lag} , which defines the discrete steps of the MSD. The offset in the MSD plot derives from the limited positional accuracy (PA) of the localization algorithm, indicated by the green dashed line and circles in A & B.

Uncertainties in determining the particle's exact positions are accounted for by an additional term in (7), resulting in:

$$\langle r^2 \rangle = 4Dt + 4\sigma^2 \quad (9)$$

where $4\sigma^2$ is the offset of the MSD (Figure 19), which derives from the limited positional accuracy (PA) of the localization algorithm [105].

Because diffusion is a stochastic process, for a small number of tracked points a particle undergoing Brownian motion might appear to undergo a sub-diffusive or directed trend over

a certain period of time [103]. The time-averaged MSD can be further averaged over multiple trajectories to further increase statistics [106]. While this additional averaging yields a smoother MSD curve, it prevents the detection of heterogeneities in the individual particle behaviour. However, differences in diffusion characteristics between grouped subsets of particles can still be extracted by studying the distribution of squared displacements [107].

Analysis of Multiple diffusion components:

An alternative approach to extract information on the mobility is to analyse SPT data by examining the probability distribution function of the squared displacements [107]. By considering a biexponential fit to the cumulative density function (CDF) of the square displacements (10), the data can be fitted to a slower and faster moving population, revealing multi component mobilities. The diffusion coefficients D_1 and D_2 account for the diffusion rate of the faster (α) and the slower fraction ($1 - \alpha$) respectively. In addition, this method gives information on the ratio of mobile to immobile molecules.

$$CDF = 1 - \alpha \cdot e^{-\frac{x^2}{MSD_1}} - (1 - \alpha) \cdot e^{-\frac{x^2}{MSD_2}} \quad (10)$$

Analysing the distribution of squared displacements provides access to individual diffusion coefficients of different fractions of mobility, an advantage which is lost in ensemble averaging MSD studies.

Diffusion Modes

Individual tracer molecules in the plasma membrane exhibit a variety of different diffusion modes (Figure 21), which can be identified with MSD analysis [103]. The dependence of the MSD on t_{lag} is related to the type of motion performed by the particle and therefore the shape of the plotted MSD curve is characteristic to the diffusion mode [105] (Figure 20).

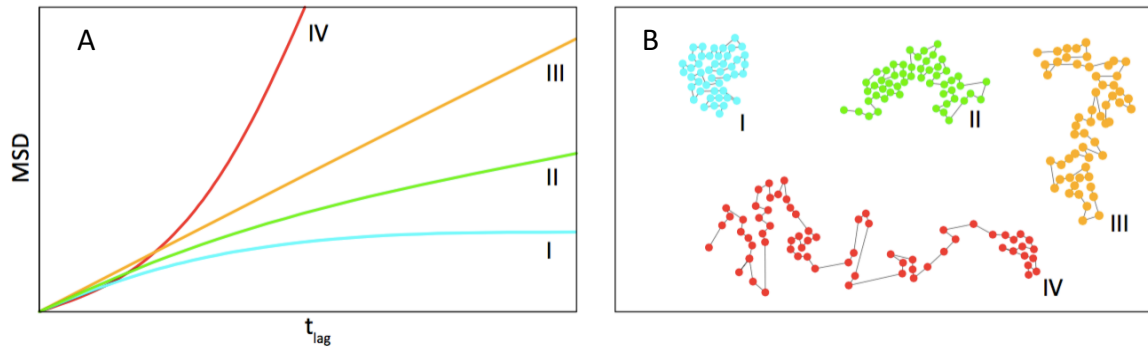


Figure 20: A: MSD plots for representative types of diffusion in 2D. Brownian motion shows a linear behavior (orange line), while anomalous sub-diffusion displays a sublinear behavior (green line). Directed motion (red line) is characterized by a positive curvature of the MSD and the blue line shows the case for confined diffusion. B: Schematic representation of particle trajectories according to their MSD curves depicted in A: (I) confined motion, (II) anomalous sub-diffusion, (III) Brownian motion, (IV) directed diffusion.

Brownian motion: If the MSD increases linearly in time, the particle moves randomly without a certain direction, and the diffusion process is defined as Brownian motion [103]. For this type of movement, the diffusion coefficient D is constant over time and can be estimated from a linear fit to the short time lag region of the MSD plot according to $MSD(t) = 4Dt$ (Figure 20, III).

Confined diffusion: Apart from random motion, SPT measurements have detected a confined motion of particles moving on cell membranes and different diffusion models have emerged trying to explain the existence of this phenomenon. One explanation of the confinement is based on the temporary trapping of receptors within sub-microdomains on the plasma membrane, imposed by the actin cytoskeleton. According to this model the long range diffusion of molecules is restricted, while short range diffusion within each compartment is more rapid and defined by Brownian motion ([108], [109]). Alternatively, confined diffusion may be interpreted as anomalous diffusion which is affected by the heterogeneous and crowded membrane environment [110].

Anomalous sub-diffusion: The high concentrations of interacting lipids and proteins in the cell membrane are believed to be the cause of another mobility mode known as anomalous diffusion ([111],[112],[113]). Figure 20 (II), shows the case of this diffusion type which is characterized by a sublinear increase of the MSD following the relation $MSD \propto t^\alpha$. The time dependence of the diffusion coefficient is measured by the exponent α , ranging from 0.1 to 0.9. For Brownian diffusion α equals to 1 and the equation reduces to $MSD(t) = 4Dt$. Ken Ritchie et al. [96] showed that parameters characterizing simple Brownian motion are not affected by time-related experimental conditions, whereas in the case of anomalous sub-diffusion a strong influence was observed, resulting in a reduction of the diffusion coefficient for longer time scales. The dependence of the diffusion parameters on the observation time

could therefore be used as a measure to identify anomalous sub-diffusion [96].

Directed motion: Active transport of membrane proteins can be initiated by e.g. endocytosis or actin-transport, resulting in directed motion which is observed when the MSD shows a time dependence with an $\alpha > 1$, characterized by a positive curvature of the graph (Figure 20).

Immobilization: Complete immobilization of particles can occur when particles are bound to immobile membrane elements, such as large protein complexes anchored to the cytoskeleton. This diffusion mode is characterized by a much lower diffusion coefficient than what would be expected by Brownian motion and an $\alpha < 0.1$.

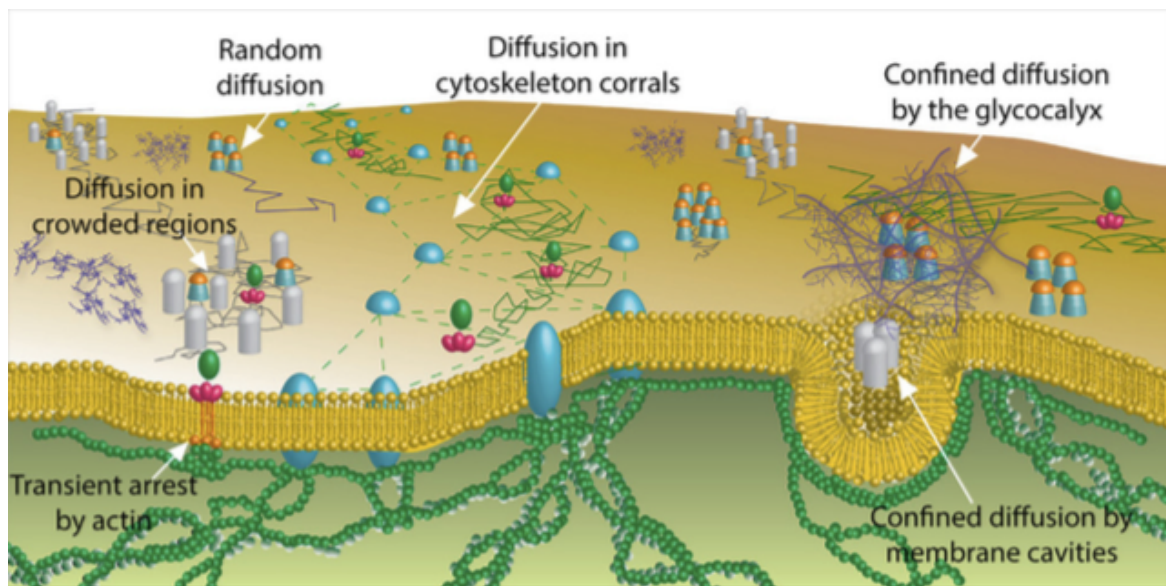


Figure 21: Schematic representation of the diverse lateral diffusion modes of membrane proteins on the heterogeneous cell surface environment [94].

2 Materials & Methods

2.1 Cell Culture

Primary 5c.c7 T cells were isolated from murine spleen and cultured in sterile filtered T Cell Medium (TCM) which was made by supplementing 500 ml RPMI-1640 (Lonza, Basel, Switzerland) with 50 ml heat-inactivated Fetal Bovine/Calf Serum (FBS/FCS, Sigma-Aldrich, St. Louis, USA), 5 ml Non-Essential Amino Acids (Lonza, Basel, Switzerland), 5 ml Penicillin/Streptomycin, 5 ml Sodium Pyruvate (Sigma-Aldrich, St. Louis, USA) and 50 μ M Mercapto-ethanol (AppliChem, Gatersleben, Germany). The T cells were maintained in the incubator at 37°C with 5% CO₂.

For retroviral transduction of primary murine T cells, Phoenix-ECO [114] cells were cultured in Dulbecco's Modified Eagle Medium (DMEM, Sigma-Aldrich, St. Louis, USA), supplemented with 10% FBS, Penicillin, Streptomycin (Lonza, Basel, Switzerland) and L-Glutathione (Sigma-Aldrich, St. Louis, USA). The cells were kept incubated at 37° C with 5% CO₂ and passaged every 3–4 days to ensure a 70-80% confluence for optimal transfection.

For cell transfection with ζ -GFP, used for micropatterning experiments, primary murine lymph node T cells were used and treated similarly to the aforementioned splenocytes.

ζ diffusion experiments were performed on stably transfected Jurkat T cells expressing ζ -SNAP-tag proteins which were cultured in RPMI-1640 (Sigma-Aldrich, St. Louis, USA) medium in the incubator. Transfection was performed with the same retroviral transfection protocol as described in 2.1.2, using ζ -SNAP plasmids.

2.1.1 Transformation of E. coli and Midi Preparation

For reproduction of ζ -GFP plasmid for T cell transduction, the plasmid DNA was transfected into bacteria in a medium culture (midi prep). For this preparation competent Escherichia coli bacteria were thawed and 20 μ l KCM buffer (KCl - CaCl₂ - MgCl₂), 9 μ l dH₂O and 1 μ l of the ζ -GFP plasmid were added. First, the dilution was incubated for 10 minutes on ice, followed by additional 10 minutes at room temperature. 1 ml lysogeny broth (LB) medium was added and the resulting mixture was incubated for one hour on a Thermomixer Comfort (Eppendorf, Hamburg, Germany) at 37 °C and 400 rpm. 100 μ l of the bacteria dilution were plated on an ampicillin coated 10 cm petridish and incubated over night at 37 °C. The next day, a single colony from the plate was picked and incubation was carried out on the Thermomixer at 37 °C with a constant shaking at 400 rpm within 1 ml of LB medium. After eight hours, 50 ml of medium were added and left for incubation on the Thermomixer overnight. The following day, midiprep was done by using the GeneJET Plasmid Midiprep Kit (Thermo Fisher Scientific, Waltham, USA) according to protocol for plasmid purification. The final plasmid concentration was determined photometrically using a Synergy H1 Multi-Reader (BioTek, Winooski, USA).

2.1.2 T cell Transduction

The transduction of primary murine T cells was performed according to the protocol described in [115]:

Day 0	The Phoenix-ECO cells were seeded in a 10 cm petri dish with 10 ml of complete DMEM media to reach 70-80% confluence before transfection the next day and T cells were isolated at MUW.
Day 1	Phoenix-ECO cells were transfected with 15 µg ζ-GFP plasmid and 9 µg pclECO plasmid using TurboFect Transfection Reagent (Thermo Fisher Scientific, Waltham, USA) and Opti-MEM medium (Life Technologies, Carlsbad, USA). 6-8 hours later the medium was exchanged to 5ml of full supplemented DMEM.
Day 2	The isolated T cells were collected from MUW and cultured in T Cell Medium at 37° C with 5% CO ₂ .
Day 3	48 hours after transfection, prior to transduction, the viral supernatant from the Phoenix-ECO cells was collected and spun down to remove cell debris. At the same time 4 million T cells were spun down (300 rpm, 22°C, full brake, 3 minutes) and resuspended in 4 ml of the virus-containing supernatant. 10 µg/ml Polybrene (Sigma-Aldrich, St. Louis, USA) and 9 µg/ml IL-2 (eBioscience, San Diego, USA; 50 U/ml) were added. The cells were plated on a 24-well plate, one million cells per well and the plate was sealed with parafilm. The sample was centrifuged for 90 minutes in a pre-warmed (32° C) centrifuge with the centrifugal settings set to a relative centrifugal force (rcf) of 2000g, acceleration at five and brake set to zero. At the end of centrifugation 1 ml of TCM and 9 µg/ml IL-2 were added and cells were kept in incubator at 37° C with 5% CO ₂ .
Day 4	The next day, cells were split 1:2 and 1 ml TCM was added resulting in 2 ml per well. 50 µg/ml Blastidine was added to select transduced cells.
Day 6	Transduced cells were isolated by density gradient centrifugation using Histopaque 1119 (Sigma-Aldrich, St. Louis, USA). The remaining cells were resuspended in TCM with 9 µg/ml IL-2 at 1 million cells per ml.
Day 7-9	Days on which experiments could be performed.

2.2 Sample preparation

2.2.1 Labelling

(i) scFv labelling:

For the comparison of TCR β diffusion on different adhesion surfaces tracking experiments were performed with primary T cells using fluorescently labelled anti-TCR β single chain fragments (scFv) derived from the monoclonal antibody H57. Low density labelling was achieved by using scFv conjugated to the fluorescent dyes Alexa Fluor 488 (AF488), Alexa Fluor 555 (AF555) or Abberior STAR635 (AS635) mixed 1:5 with unlabeled scFv. Labeling was achieved by adding 0.5 μ l of the scFv mixture to 50 μ l cell suspension, yielding a final concentration of 2 μ g/ml of fluorescent scFv, while maintaining labelling at saturation (10 μ g/ml). The sample was incubated for 15 minutes on ice and washed three times with imaging buffer (Hank's balanced salt solution (HBSS) supplemented with 2% FBS).

For combined micropatterning and FRAP experiments, transfected primary murine T cells were labelled in saturation with Alexa Fluor 647 (AF647)-scFv, following the same incubation protocol.

(ii) SNAP labelling

SNAP-Cell 647-SiR (New England Biolabs (NEB), a far-red fluorescent substrate, was used to label the SNAP-tag fusion proteins on the transfected Jurkat T cell surfaces. SiR-SNAP dyes were dissolved in imaging buffer at a concentration of approximately 0.3 μ g/ml and 1 μ l was added to 200 μ l cell suspension to achieve a final concentration of 5 nM. After the first incubation period of 15 minutes at 37°C, the probe was washed once with imaging buffer (HBSS + 2% FBS) followed by a second 30-minute incubation at 37°C and two further washing cycles.

(iii) Antibody labelling

Full length antibodies H57 conjugated with AF647 at a stock concentration of 0.5 mg/ml were dissolved in PBS to obtain a 50 μ g/ml concentration. 1 μ l was added to 50 μ l cell suspension to achieve a final concentration of 1 μ g/ml. Following the same procedure as for scFv, the sample was incubated for 15 minutes on ice and afterwards washed three times with imaging buffer (HBSS + 2% FBS).

2.2.2 Surface preparation

For all tracking experiments, NuncTM LabTEKTM Chambers (Thermo Fisher Scientific, San Diego, USA) were used which were stored in Ethanol (Sigma-Aldrich, St. Louis, USA).

For the diffusion measurements on different adhesion surfaces LabTEK chambers were prepared with #1.5 glass slides (Menzel, Jena, Germany) that were cleaned with 100%

Ethanol, rinsed with distilled water (dH₂O) and dried with nitrogen (N₂). The cleaned glass slides were glued to the chambers by a two-component dental glue.

For the preparation of PDL and FN coated surfaces, coverslips were immersed in solutions of 50 µg/ml PDL or 50 µg/ml FN (Sigma-Aldrich, St. Louis, USA) for 45-60 minutes at room temperature and then washed with PBS to remove any traces of unabsorbed molecules.

For the formation of supported lipid bilayers glass coverslips were first cleaned with 100% ethanol, washed with dH₂O and plasma cleaned for 10 minutes to remove any organic residues. A vesicle stock solution containing 90% 1-Palmitoyl-2-oleoylphosphatidylcholine (POPC) and 10% Nickel chelated 1,2-dioleoyl-sn-glycero-3-[[N-(5-amino-1-carboxypentyl)iminodiacetic acid) succinyl] (DOGS) was diluted 1:10 with Phosphate Buffered Saline (PBS, Lonza, Basel, Switzerland). 150 µl of the vesicle suspension were added to each well and incubated for 10 minutes. After the wells were rinsed with PBS to eliminate any free lipids, 330 µl were removed from each well leading to a remaining volume of 350 µl per well. Additional 50µl of PBS containing 0.3µl ICAM-1 were added to each well and incubated for 75 minutes. After incubation the wells were washed twice with PBS without exposing the bottom of the well to the air.

For preparation of micro-patterned surfaces biotinylated αCD3 antibodies were incubated on coverslips featuring streptavidin patterns according to the following protocol:

The basic preparation steps are illustrated in Figure 22 (1-4). The production of micro-structured surfaces was based on µ-contact printing by PDMS stamps bearing circular features with a diameter of 1 µm. For the experiments the stamps were first rinsed with 100 % ethanol and dH₂O, dried with N₂ and incubated with 50 µg/ml streptavidin (AppliChem) dissolved in PBS for 30 minutes at room temperature (1). Stamps were dried with N₂ flow (2), placed on epoxy glass slides (Schott) (3), and kept in a parafilm padded petri dish with a wet paper towel in the fridge for 24 hours. Upon removal of the stamps, the patterned areas were confined by Secure-Seal hybridization chambers (Grace Biolabs) and incubated with 50 ug/ml solution of fibronectin (dissolved in 1% PBS) for 60 minutes to passivate the interspaces. This step was followed by washing with 1% PBS and a 30-minute incubation with 10 µg/ml biotinylated αCD3-antibody (clone: KT3, Thermo Fisher Scientific, San Diego, USA) dissolved in PBS with 1% BSA (bovine serum albumin, Sigma-Aldrich) (4). The same protocol was adapted for the control patterns prepared with biotinylated GFP antibody (Novus). After the antibody incubation the samples were rinsed with PBS.

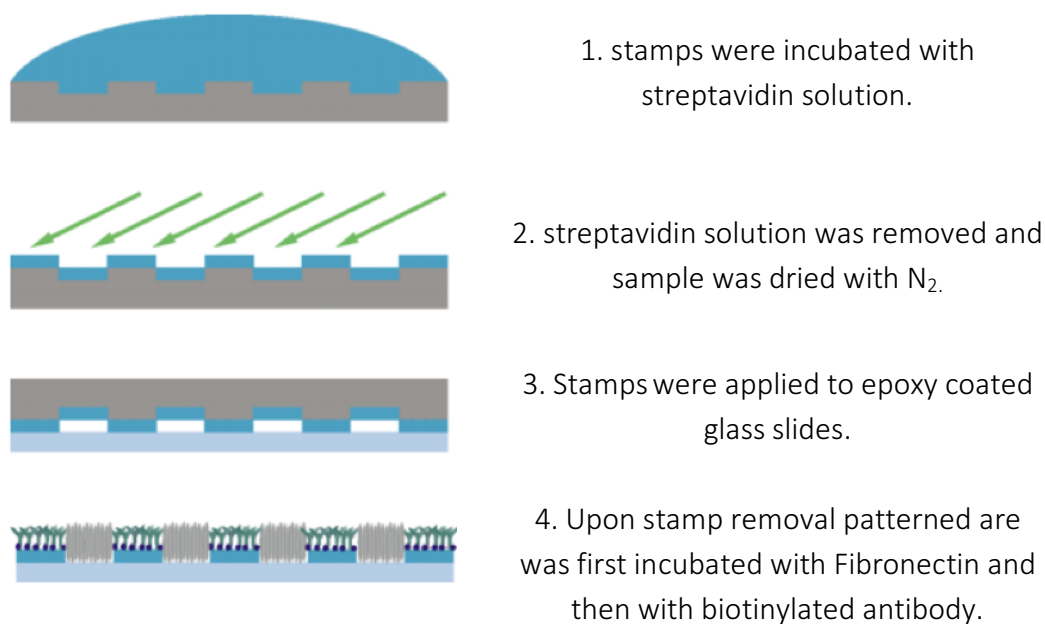


Figure 22: Illustration of the micropatterning protocol. Figure modified from [116].

2.3 Setup

All experiments were performed on the homebuilt microscope set-up referred to as SDT1. Excitation light was provided by a blue laser at 488 nm and a red laser at 640 nm. The blue laser line passed acousto-optical modulators (AOMs; Isomet, Springfield, USA) and both lasers were transmitted through multiple mirrors to reach an inverted light microscope, a Zeiss Axiovert 200 (Zeiss, Jena, Germany). An oil-immersion α -plan Apochromat (Zeiss, Jena, Germany) objective with an NA of 1.46 was used, enabling objective-based TIRF and HiLO microscopy. The separation of excitation and emission was achieved with a quad band TIRF filter (ZT405/488/532/640rpc, Chroma, Bellows Falls, USA) and FITC/Cy5 filter set (Chroma, Bellows Falls, USA) was used for GFP imaging. The emitted light was detected with an Andor iXon Ultra EMCCD camera (Belfast, UK) which was kept at -60°C during measurements to reduce thermal noise. A DV2 Multichannel Imaging System (Tuscon, USA) was used for two color experiments.

The set-up equipment comprising the laser shutter, the AOM, the EMCCD camera and the TIRF and HiLO illumination was operated by an in-house programmed LabVIEW (National Instruments, Austin, USA) package.

2.4 Single particle tracking

2.4.1 Image recording

All tracking experiments were done at room temperature using imaging buffer composed of HBSS containing 2% FBS, and within 45 minutes after cell seeding. Illumination times of 2-5 ms and delay times of 45-48 ms were used, resulting in a t_{lag} of 50 ms between image acquisitions; a total of 200 frames were recorded.

t_{lag} measurements:

To study the influence of t_{lag} on the diffusion coefficient and further identify anomalous diffusion, single particle tracking experiments were conducted with acquisition rates of 2, 10, 50 and 100 ms for 200 frames. The 2 ms t_{lag} movies were realized by measuring in *Cropped-Mode* [117], a camera setting which allows for higher frame rates.

2.4.2 Diffusion Data Analysis

Localization:

Image analysis was performed by self-written ImageJ macros. The ImageJ plugin *thunderSTROM* [118] provides a fitting method for the raw data. A pre-filtering in form of a wavelet (B-Spline) filter of order 3 and scale 2 was applied and the approximate particle positions were found by searching for local maxima. Maxima were identified by applying a threshold of 1.5 times the standard deviation of the first wavelet level, which were previously determined in the pre-filtering step in an 8-neighbourhood. Using an integrated Gaussian as PSF, the sub-pixel localization of each detected diffraction-limited spot was obtained. This fitting process was realized by applying MLE with a radius of 6 pixels and an initial sigma of 1.6 pixel.

Tracking:

Tracking was achieved by the analysis software *particle_tracking_2D*, an in-house implementation [119] derived from an algorithm created by Gao et al [100]. Tracks were generated by frame-to-frame linking of particles and the connection of the segments was based on three user-defined parameters:

- (i) The maximum distance (d_{max}), expressed in pixels, is defined as the furthest distance a particle can travel in consecutive frames and still be identified as the same particle.
- (ii) The number of connections determining the minimum track length (l_{min}).
- (iii) The maximum number of frames a particle is not detected due to blinking, photobleaching or missed localization but is still linked if it reappears (fr_{omit}).

These tracking parameters were adjusted to the imaging conditions during the tracking experiments, considering the duration of applied t_{lag} :

	d_{max} [px]	l_{min} [#]	f_{omit} [#]
$t_{lag} = 100$ ms	3	2	1
$t_{lag} \leq 50$ ms	2	2	1

MSD analysis:

MSD analysis was applied to classify the mobility of the single particle trajectories by the in-house software *msdplot*. The MSDs were plotted against the time lag and the diffusion coefficient was determined by fitting the function $MSD=4Dt_{lag}+4\sigma^2$, where σ denotes the localization precision in 2 dimensions and $4\sigma^2$ appoints the offset of the plotted MSD-curve. The diffusion coefficients were determined from the first two data points.

In addition, an anomalous diffusion fit was applied using the function $MSD \propto 4D_{\alpha}t_{lag}^{\alpha}+4\sigma^2$, yielding the exponent α . The α coefficient was calculated to help further characterize the motion, by defining directed motions with $\alpha > 1.1$, Brownian motion with $0.9 < \alpha < 1.1$ and anomalous sub-diffusion $0.1 < \alpha < 0.9$.

The average number of tracked particles and their track lengths were evaluated by *msdplot* and a minimum track length of 5 frames was used for analysis. To further increase statistics, averaging over the ensemble composed of multiple trajectories resulted in the time-ensemble averaged MSD.

Furthermore, a bi-exponential equation was fit to the cumulative density function (CDF) of the square displacements by the in-house program *explot*, as described in 1.5.3.

2.5 FRAP experiments

Transfected primary murine T cells expressing ζ -GFP and additionally labelled with TCR β -scFv-AF647 were seeded on the micropatterned surfaces and imaged using imaging buffer (HBSS+2%FBS). To analyze the fluorescence recovery process of ζ -GFP and TCR β -scFv-AF647 in the enriched patterns, an area comprising 2-3 spots was defined by the set-up apertures. Depending on the size of the cell, the appointed region of interest (ROI) covered about 25-33% of the basal membrane surface. Image sequences were acquired according to the following protocol: a prebleach image was taken with an illumination time of 2 ms and at a low laser power, followed by a 1000 ms photo-bleaching pulse with high laser intensity. After a recovery period of 50 ms a movie of 100 recovery images was recorded with 1000 ms between frames. Timing protocols were generated by an in-house programmed LabVIEW (National Instruments, Austin, USA) package.

2.5.1 FRAP data analysis

Image analysis of the FRAP measurements on single spots was performed by using ImageJ and an in-house algorithm implemented in MATLAB (Mathworks), as described in [67]. In all the collected FRAP frames, taken before and after bleaching, the fluorescent intensity was measured in the bait-captured areas (F_{on}) above the bait-free areas (F_{off}) as a function of time. F_{on} was determined by framing the bait-captured spot and plotting its intensity values for the sequence of images. The signals contributing to F_{off} came from a square shaped area encircling the F_{on} pattern, providing information of the intensity in the bait free areas of the membrane (Figure 23). FRAP data were analyzed by calculating:

$$\Delta F = \frac{(F_{on} - F_{off})}{(F_{on} - F_{off})_0}$$

ΔF describes the fluorescence at the bait-captured area (F_{on}) above the bait-free area (F_{off}), normalized by the pre-bleach image, $(F_{on}-F_{off})_0 = \Delta F_0$.

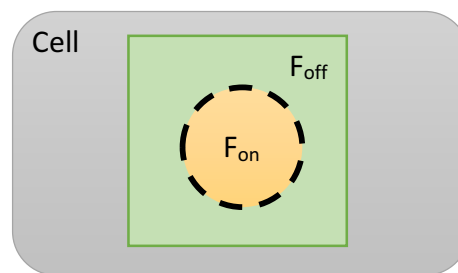


Figure 23: Illustration of the areas contributing to the bait-captured signals (F_{on}) and the bait-free signals (F_{off}).

3 Results

3.1 TCR diffusion analysis

In this work, single molecule tracking experiments were performed to investigate to which degree the diffusion behavior of the TCR membrane protein might be affected by different experimental conditions. Essential aspects of sample preparation for microscopic examination were considered, investigating the effects of different cell adhesion strategies and fluorescent labelling techniques.

3.1.1 Different t_{lag} measurements

Parameters characterizing confined diffusion are affected by time-averaging over the t_{lag} . In case of anomalous sub-diffusion, reduced diffusion coefficients are the consequence of longer time scales during the measurements [96]. When examining the results presented in Figure 24, a high anomalous sub-diffusive fraction seems to govern TCR mobility. To study the influence of t_{lag} on the diffusion coefficient and further identify anomalous diffusion, TCR β labelled with scFv conjugated to Abberior STAR 635 was tracked with acquisition rates of 2, 10, 50 and 100ms for 200 frames. The results are presented in Figure 24A, showing the diffusion constants of trajectories averaged over individual recordings. The distribution of the diffusion coefficients measured at different t_{lags} are presented in Figure 24B. The values of the diffusion coefficient D decreased with increasing t_{lag} , indicating the presence of anomalous sub-diffusion.

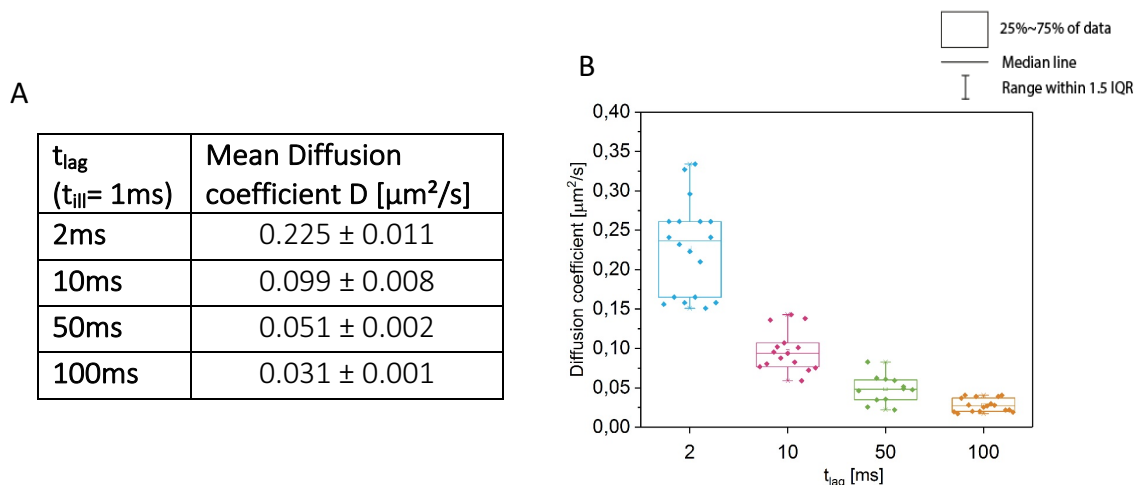


Figure 24: Experiments on primary murine T cells labelled with scFv-AF488 were performed in room temperature on Poly-D-Lysine coated coverslips. To study the effects of t_{lag} on the estimated diffusion coefficients trajectories were recorded with an illumination time of 1ms and different delay times of 1 ms, 9 ms, 49 ms and 99 ms, yielding a reduction in diffusion rate with an increasing t_{lag} (A). B: The distribution of diffusion coefficients at different t_{lags} (2 ms, 10 ms, 50 ms, 100 ms) shows severe reductions in diffusion rates for longer t_{lags} .

3.1.2 TCR β diffusion on different adhesion surfaces

Single Particle Tracking experiments were performed to investigate the diffusion characteristics of the TCR/CD3 complex on the commonly used cell adhesion surfaces Fibronectin (FN), Poly-D-Lysine (PDL) and a Supported Lipid Bilayer system (SLB). The receptor was labelled using anti-TCR β scFv covalently bound to the organic dye AF488, which allowed for tracking TCR β movement on the plasma membrane. The particles were monitored using fluorescence imaging in TIRF mode, capturing the diffusion at the interface between the basal surface of the cell membrane and the adhesion surface (Figure 25).

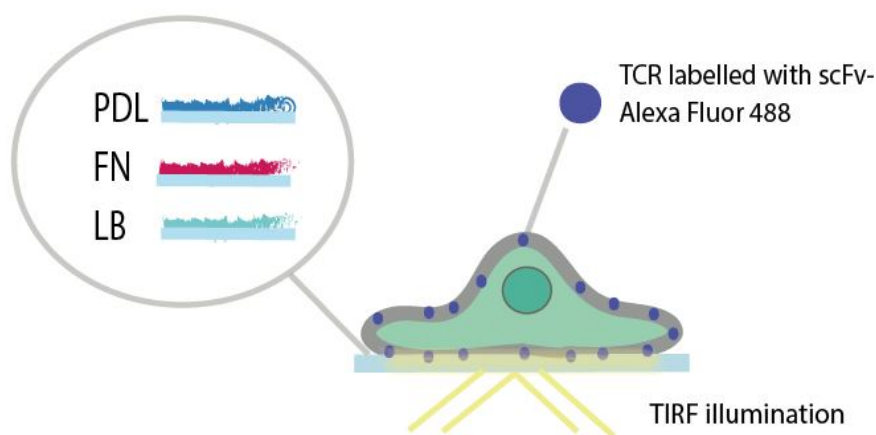


Figure 25: Schematic illustration of the experimental set up. T cells sparsely labelled with scFv-AF488 were plated on glass coverslips featuring PDL, FN or SLB. TIRF illumination excites fluorophores on the basal cell membrane at the interface to the adhesion surface.

Two minutes upon seeding, cell attachment was observed for all three surface conditions, making them suitable for the adhesion of T cells for microscopic imaging purposes. Figure 27A shows exemplary images of these fluorescent probes bound to T cells of differently coated slides. A series of 200 images was recorded with a t_{lag} of 50ms. The resulting diffusion characteristics are presented in Table 2. In general, low mobility was observed for the tracked molecules. The diffusion coefficients, retrieved by the linear fit to the first two data points of the MSD graph, were similar for all coated glass slides ranging from 0.03-0.06 $\mu\text{m}^2/\text{s}$.

Modes of Diffusion:

The trajectories were further evaluated by visual analyzation of the MSD plots as their shape might be indicative of different modes of diffusion. Additionally, the α coefficient was calculated to further characterize the motion. The ensemble MSD plots, averaged over the trajectories taken from at least 20 cells for each surface, show an anomalous sub-diffusive trend and are overlaid for comparison and presented in Figure 26A.

On average 15-60 tracks were captured per recording and their MSDs were averaged over the individual movies. When examining these trajectories heterogeneities in their diffusion

modes were visible. The majority of plots for all three surfaces featured negative curvature (Figure 26), showing a sub-diffusive time dependence, indicating that there is little directed motion of the TCR in the presented experiments and a large population representing anomalous sub-diffusion. The results are presented in Table 2, where also the fractions of Brownian, sub-diffusive and directed motion on each surface are revealed.

To aid in the diffusion analysis and to further visualize the different modes of motion the distributions of D and α were examined for the different adhesion surfaces and are presented in Figure 27B, C. The histograms of the calculated diffusion and α coefficients confirm the different types of TCR mobility: a predominantly sub-diffusive diffusing fraction ($0.1 < \alpha < 0.9$), a free diffusing fraction ($0.9 < \alpha < 1.1$) and a directed motion fraction ($\alpha > 1.1$).

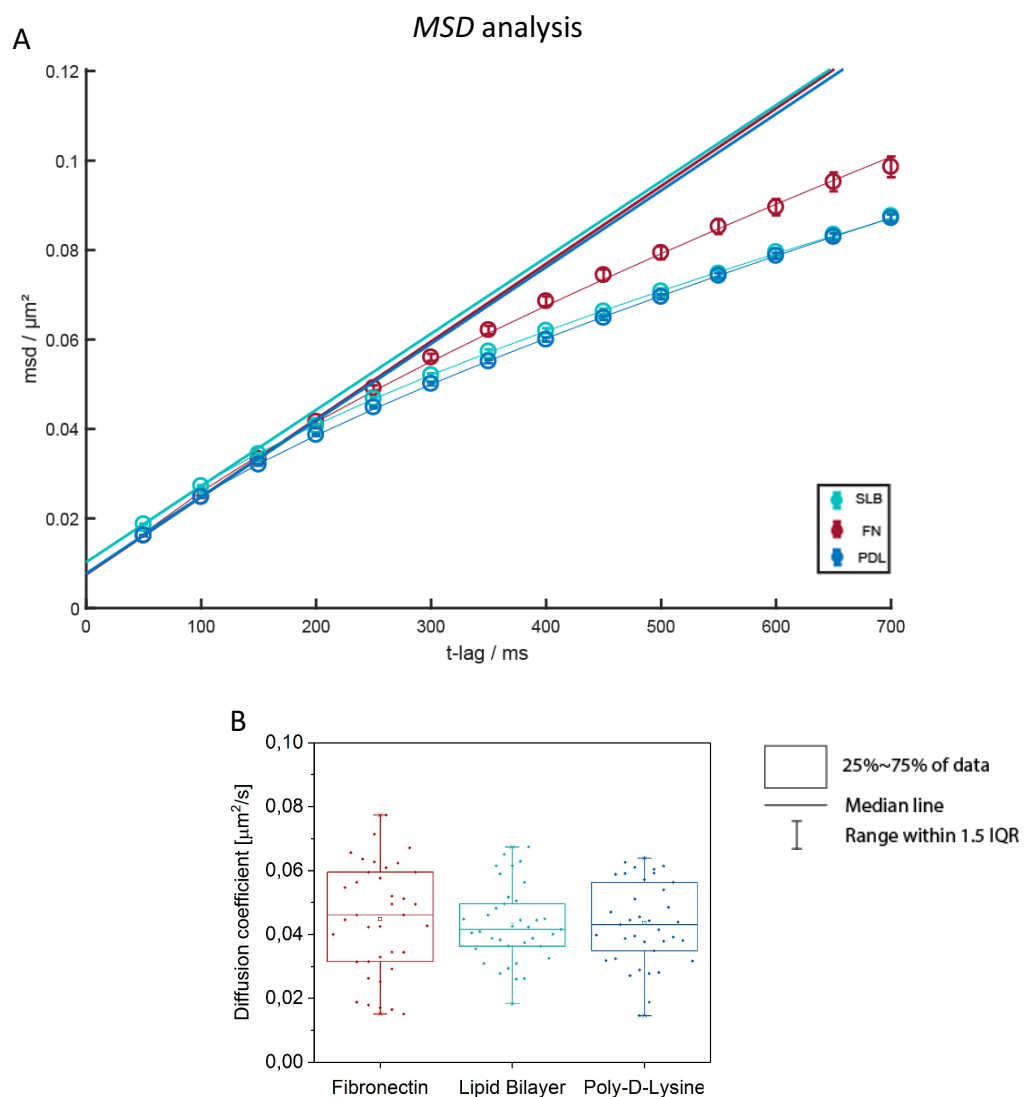


Figure 26: MSD analysis. A: Ensemble MSD curves for cells imaged with TIRFM on FN (red), PDL (blue) and SLB (turquoise). Tracks were acquired at room temperature with an illumination time of 2ms and total t_{lag} of 50ms. Linear fits to the short t_{lag} region were used to determine the diffusion coefficients and the anomalous fit was applied to obtain α values. B: Distribution of diffusion coefficients from trajectories averaged cell by cell.

Analysis of Multiple diffusion components:

The tracked receptors have indicated the presence of both a mobile population and a fraction that is relatively immobile over the time scale of the experiment. To identify multiple diffusion components the trajectories were evaluated through *explot*, where fitting to a biexponential function revealed the presence of a slower diffusing fraction of about 30-40% in the diffusion of TCR β on all three surfaces (Figure 28). With average diffusion rates of $D_1 \approx 0.012-0.018 \mu\text{m}^2/\text{s}$, this mobility component is identified as the immobile fraction. The faster diffusion component is similar on all three surfaces, yielding values of $D_2 \approx 0.060-0.067 \mu\text{m}^2/\text{s}$. Figure 28 shows the ratio of mobile to immobile fractions and the diffusion behavior for the two mobility components.

Diffusion properties on different adhesion surfaces

<i>scFv-AF488</i> $t_{lag} = 50\text{ms}$	Fibronectin	Poly-D-Lysine	Supported Lipid Bilayer
Mean diffusion coefficient D [$\mu\text{m}^2/\text{s}$]	0.043 ± 0.002	0.044 ± 0.011	0.046 ± 0.014
Mean α coefficient	0.74	0.69	0.63
Number of tracks	2926	3411	2470
Mean track length	17.7	21.4	18.1
TCR diffusion	68% mobile ($D_2 \approx 0.060 \pm 0.011 \mu\text{m}^2/\text{s}$) 32% immobile ($D_1 \approx 0.017 \pm 0.006 \mu\text{m}^2/\text{s}$)	67% mobile ($D_2 \approx 0.066 \pm 0.019 \mu\text{m}^2/\text{s}$) 33% immobile ($D_1 \approx 0.012 \pm 0.005 \mu\text{m}^2/\text{s}$)	67% mobile ($D_2 \approx 0.066 \pm 0.021 \mu\text{m}^2/\text{s}$) 33% immobile ($D_1 \approx 0.018 \pm 0.006 \mu\text{m}^2/\text{s}$)
Diffusion modes			
- Sub-diffusive	69%	62%	79%
- Free	20%	15%	18%
- Directed	11%	23%	3%

Table 2: TCR β diffusion characteristics for cells resting on Fibronectin, Poly-D-Lysine and Supported Lipid Bilayers. The results were obtained with MSD and *explot* analysis. The mean diffusion coefficients and α values represent the ensemble average over all tracked receptors retrieved by the linear fitting of the first two data points.

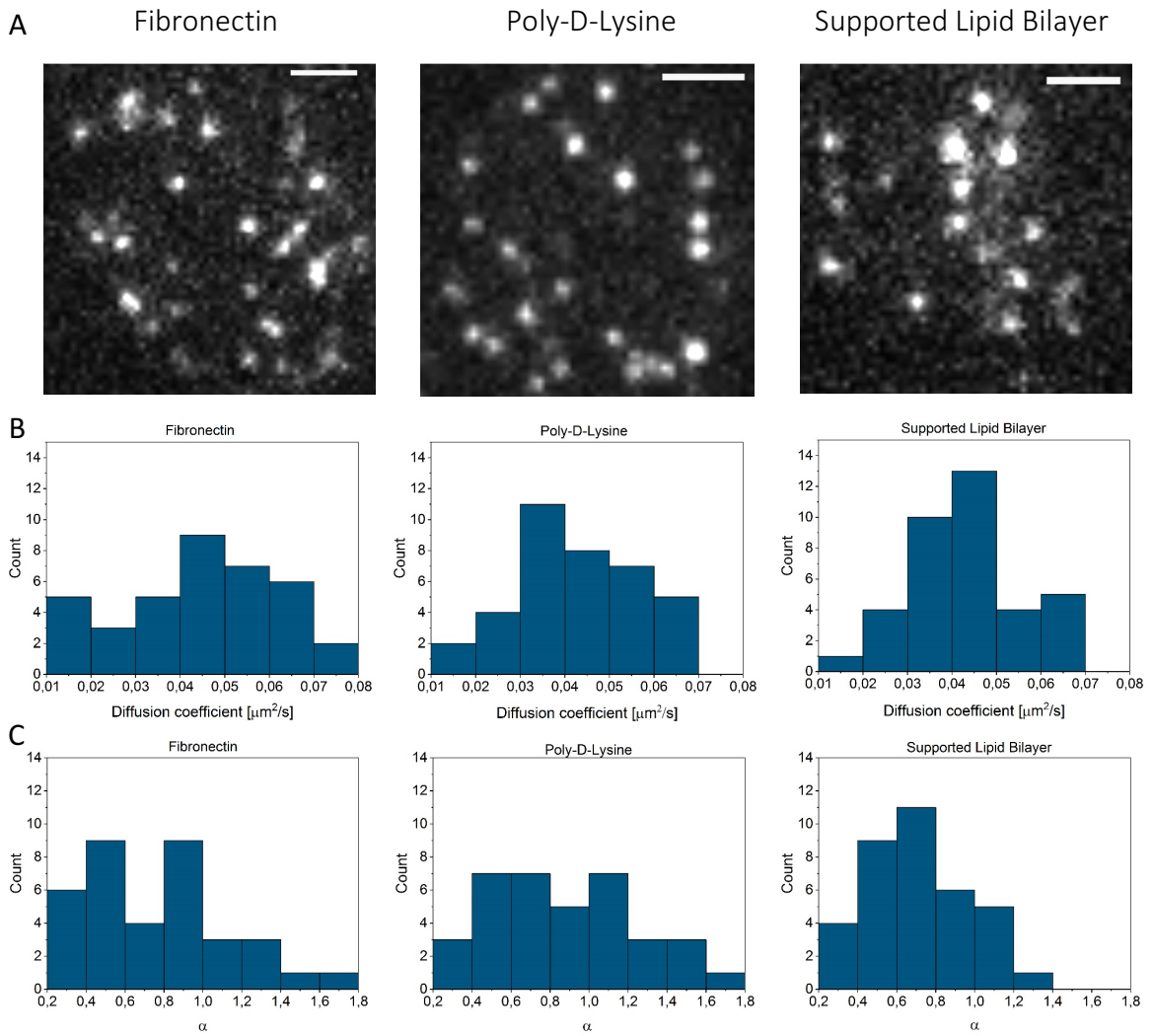


Figure 27: A: Sample of single molecule imaging results on the basal surface of primary murine T cells labelled with scFv-AF488 using TIRFM. The cells were seeded on FN, PDL and SLB coated coverslips. The scale bar is $2\mu\text{m}$. B, C: Distribution of the diffusion coefficients (B) and α values (C) for all three surfaces, based on MSD calculations of trajectories averaged over individual cells measurements.

Explot analysis

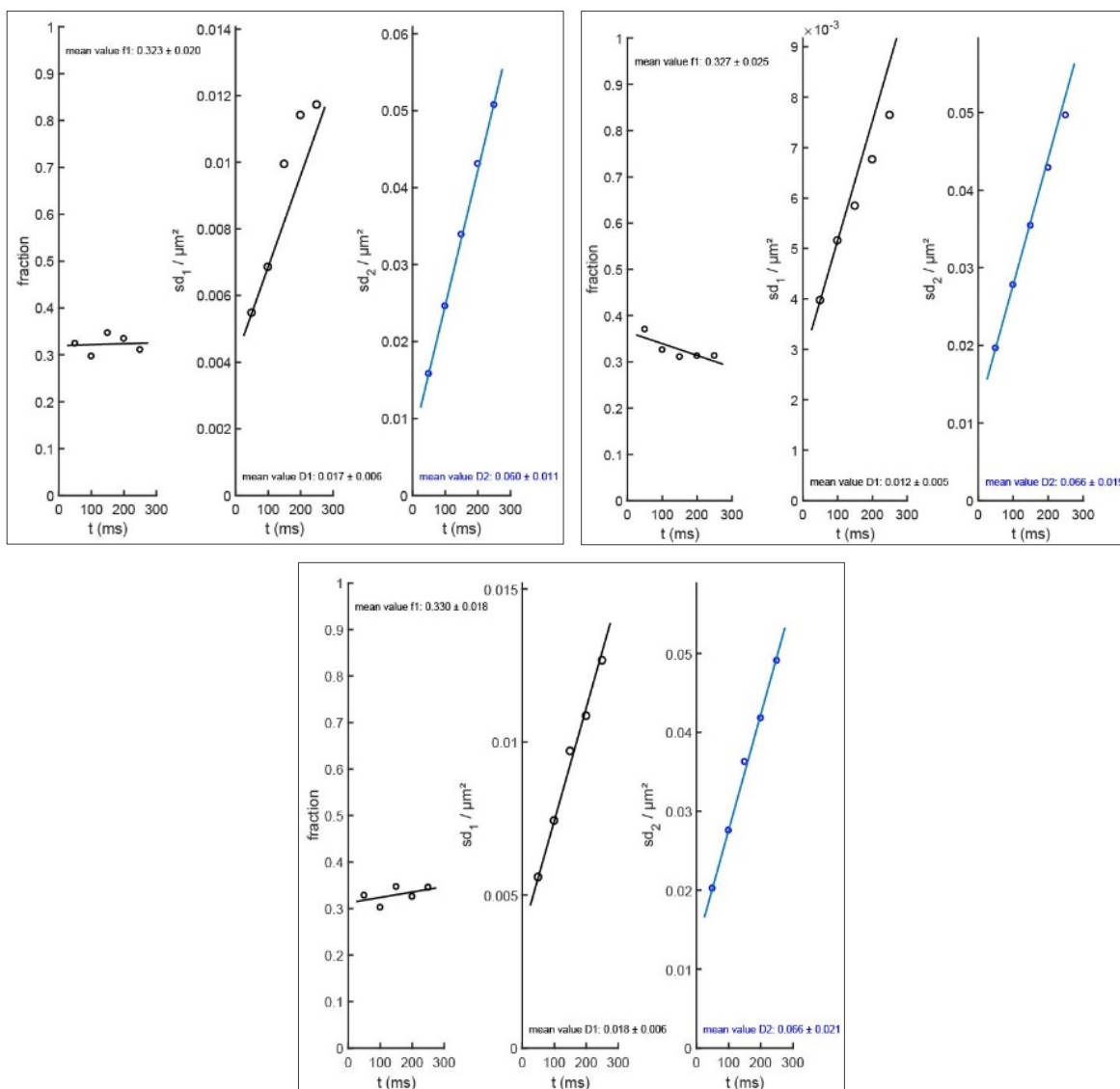


Figure 28: *Explot* analysis yielding the diffusion behaviour of a slower (middle panels) and a faster (right panels) diffusion component of the trajectories obtained on FN (upper left image), PDL (upper right image) and a SLB system (bottom image). The mobility ratio is given in the left panels.

3.1.3 Labelling strategies

In this section the results of different labelling strategies applied in tracking experiments are presented.



3.1.3.1 Different Fluorophores

To test the effects of different organic dyes on the diffusion properties of the TCR, tracking experiments were performed with scFv conjugated to the different fluorophores AF488, AF555 or

Figure 29: Illustration of the different labelling strategies evaluated in this work.

Abberior STAR 635 on PDL-coated glass slides. The results of the MSD and *explot* analysis are presented in Table 3. Figure 30 shows all ensemble MSDs, indicating a slower motion for particles labelled with scFv- AF555.

Diffusion properties for different organic dyes

Fluorophore	Mean diffusion coefficient D [μm^2]	α value	Mobile/immobile population	Mean track length
Alexa Fluor 488	0.044 ± 0.011	0.69	67% mobile ($D_2 \approx 0.066 \pm 0.019 \mu\text{m}^2/\text{s}$) 33% immobile ($D_1 \approx 0.012 \pm 0.005 \mu\text{m}^2/\text{s}$)	21.4
Alexa Fluor 555	0.025 ± 0.001	0.53	64% mobile ($D_2 \approx 0.043 \pm 0.018 \mu\text{m}^2/\text{s}$) 36% immobile ($D_1 \approx 0.006 \pm 0.003 \mu\text{m}^2/\text{s}$)	21.5
Abberior STAR 635	0.051 ± 0.002	0.57	75% mobile ($D_2 \approx 0.076 \pm 0.021 \mu\text{m}^2/\text{s}$) 25% immobile ($D_1 \approx 0.021 \pm 0.006 \mu\text{m}^2/\text{s}$)	24.4

Table 3: Diffusion characteristics derived from MSD and *explot* analysis for TCR labelled with scFv coupled to different fluorophores. Tracks were acquired with an illumination time of 2ms and total t_{lag} of 50ms.

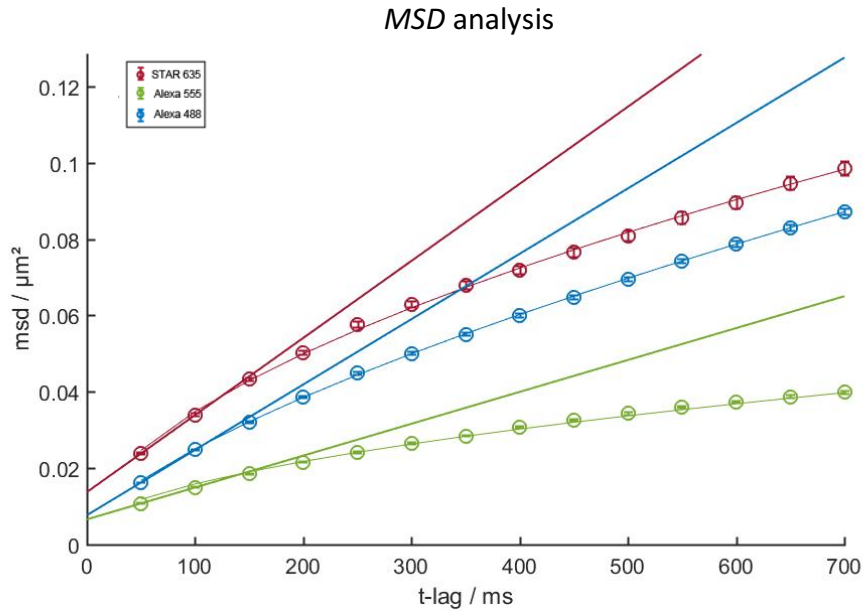


Figure 30: MSD analysis of tracking experiments using different organic dyes (red: Abberior STAR635, blue: AF488 and green: AF555) shows a relatively confined motion, with a slower diffusion of AF 555 (green). Tracks were acquired at room temperature with an illumination time of 2ms and total t_{lag} of 50ms.

3.1.3.2 Antibody measurements

To determine the effects of larger probing molecules on the diffusion of the TCR and investigate their interactions with the coating surfaces, full antibody H57 conjugated to AF647 were tracked on all three surfaces. The MSD analysis (Table 4) shows a lower diffusion rate for $\text{TCR}\beta$ labelled with antibodies compared to measurements using scFv (Figure 31). Similar diffusion coefficients ($D \sim 0.03 \mu\text{m}^2/\text{s}$) and α values (~ 0.55) were obtained on FN, PDL and SLB (Figure 32).

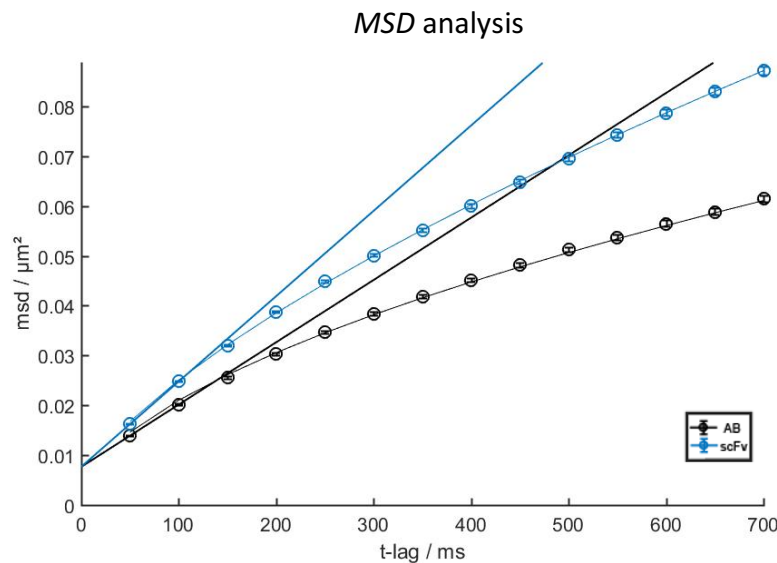


Figure 31: MSD analysis with antibody measurements with a t_{lag} of 50 ms on PDL coated cover slips. Ensemble MSD plots from tracking experiments performed with $\text{TCR}\beta$ labelled with a whole antibody conjugated to AF647 (black) and a scFv labelled with AF488 (blue).

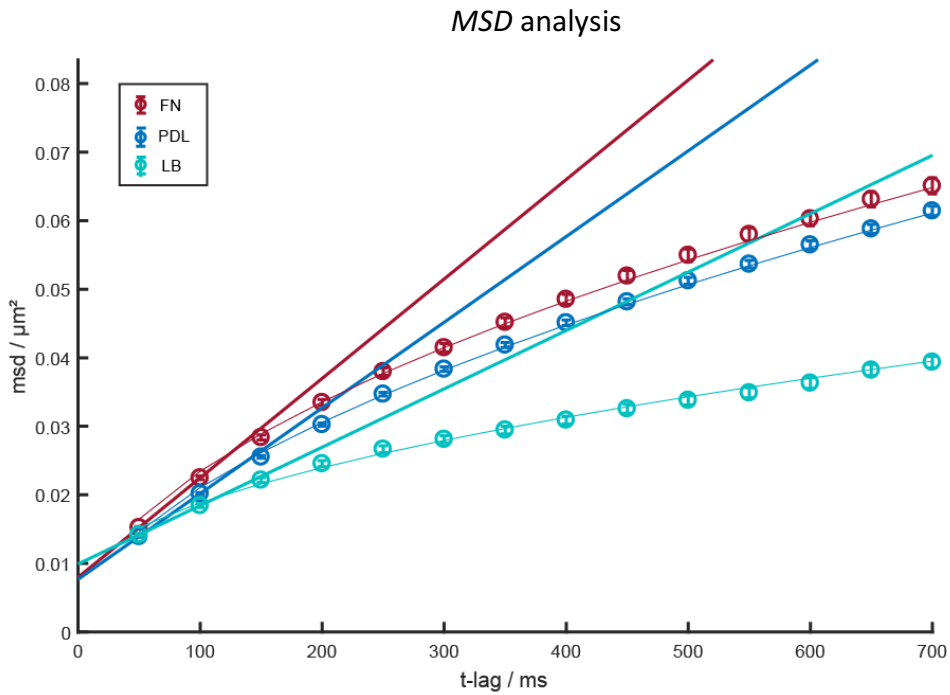


Figure 32: MSD analysis of TCR β labelled with full antibody H57 conjugated to Alexa Fluor 647 and the three adhesion surfaces Fibronectin (red), Poly-D-Lysine (blue) and a Supported Lipid Bilayer system (turquoise). Tracks were acquired with a t_{lag} of 50 ms.

Diffusion properties using antibodies

	Fibronectin	Poly-D-Lysine	Supported Lipid Bilayer
Mean Diffusion coefficient [μm^2]	0.035 ± 0.002	0.031 ± 0.001	0.021 ± 0.001
Mean α value	0.54	0.57	0.54
Mobile/immobile population	66% mobile ($D_2 \approx 0.060 \pm 0.026 \mu\text{m}^2/\text{s}$) 34% immobile ($D_1 \approx 0.009 \pm 0.004 \mu\text{m}^2/\text{s}$)	64% mobile ($D_2 \approx 0.054 \pm 0.020 \mu\text{m}^2/\text{s}$) 36% immobile ($D_1 \approx 0.010 \pm 0.004 \mu\text{m}^2/\text{s}$)	62% mobile ($D_2 \approx 0.051 \pm 0.026 \mu\text{m}^2/\text{s}$) 38% immobile ($D_1 \approx 0.008 \pm 0.004 \mu\text{m}^2/\text{s}$)

Table 4: Diffusion characteristics measured on different surfaces for TCR labelled with full antibody conjugated to Alexa 647.

3.1.3.3 Hilo vs. TIRF

The TIRFM performance was further compared to HiLO, an excitation method that enables the measurement of TCR diffusion on the apical surface of the cell, where the membrane proteins are unlikely to be affected by any interactions with the coated surface. Single particle tracks of TCR β labelled with scFv-AF488 were acquired under these conditions using PDL-coated coverslips. A decrease in diffusion rate for TCR β imaged on the apical surface (Figure 33B) was observed. Sample images recorded under the two imaging conditions (Figure 33A) show that TIRFM provided better contrast and therefore facilitated better identification of single molecules compared to HiLO. Due to the impaired image quality and the diminished z-resolution of HiLO the results were more challenging to evaluate.

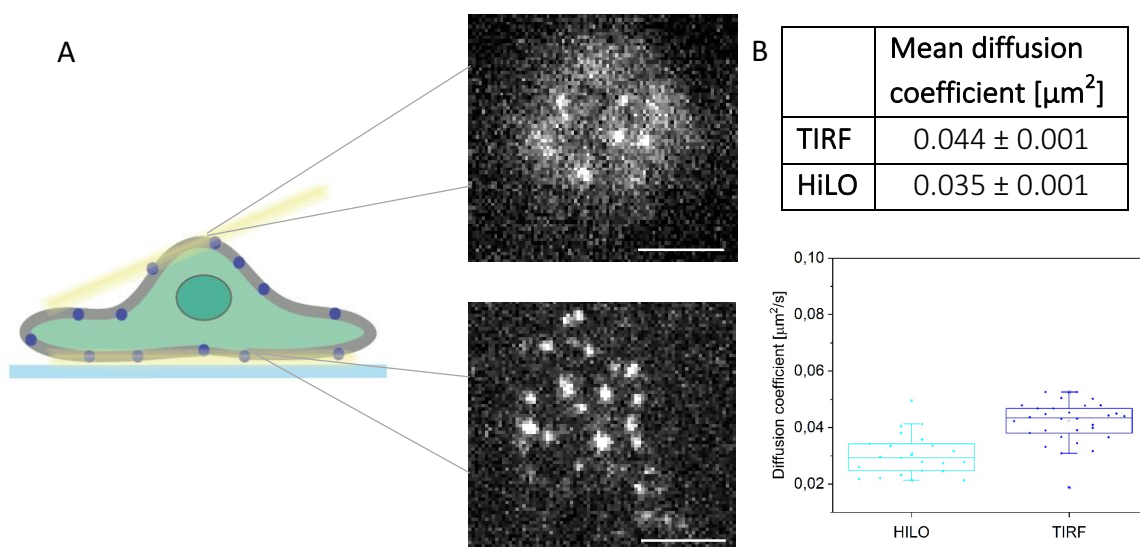


Figure 33: Capturing the TCR on the basal and apical surface of the cell. Tracking measurements were performed on more than 20 cells. Movies of 200 images were recorded with a t_{lag} of 50ms. A: Primary murine T cell labelled with low density of scFv-AF488 seeded on PDL coated coverslips. The same cell was imaged by TIRF (lower image) and HiLO (upper image) microscopy. The scale bar is $4\mu\text{m}$. B: Results of the diffusion coefficients and their distribution.

3.2 Interaction kinetics between TCR β and ζ

In the second part of this work I studied the association behavior of ζ with the other TCR/CD3 subunits by comparing its diffusion and interaction kinetics with the more stable TCR β domain of the TCR/CD3 complex.

3.2.1 Diffusion properties of ζ

The first approach to test possible differences between the two TCR components was to study and compare their diffusion characteristics. TIRFM and SPT was used to quantify movements of the TCR components within the T cell membrane of Jurkat T cells expressing a ζ -SNAP fusion protein labelled with SiR-SNAP. Primary murine T cells were used to measure the diffusion of TCR β labelled with scFv-AF488. The tracking experiments were all performed on Fibronectin-coated glass slides.

MSD analysis:

Single-particle trajectories of 3962 tracks from more than 20 cells demonstrate that the MSD time-dependence is sub-linear (Figure 34A), suggesting that the movement is anomalous, as in the case for TCR β presented above. The calculated mean diffusion coefficients (D) for both receptor subunits are presented in Table 5 and it seems as if ζ exhibits a slightly faster diffusion ($D \sim 0.07 \mu\text{m}^2/\text{s}$) than TCR β ($D \sim 0.04 \mu\text{m}^2/\text{s}$).

Explot analysis:

To gain more insight into the diffusion properties, the mobile and immobile populations were evaluated with *explot* (Table 5). The results of the bi-exponential fit (Figure 35) revealed a two-fraction population of ζ with different properties concerning their mobility: a slower, yet not fully immobile fraction of about 20% with a diffusion rate of $D_1 \approx 0.014 \pm 0.003 \mu\text{m}^2/\text{s}$, and almost 80% diffusing with $D_2 \approx 0.093 \pm 0.022 \mu\text{m}^2/\text{s}$. The *explot* evaluation of TCR β shows a more pronounced immobile fraction of about 32% with a diffusion coefficient $D_1 \approx 0.017 \pm 0.006 \mu\text{m}^2/\text{s}$; the remaining 68% feature a $D_2 \approx 0.060 \pm 0.011 \mu\text{m}^2/\text{s}$ (Table 5).

Evaluation of the diffusion modes revealed around 10% of the molecules exhibiting Brownian motion ($0.9 < \alpha < 1.1$), 76% diffusing with anomalous sub-diffusion ($0.1 < \alpha < 0.9$) and 14% featuring directed motion ($\alpha > 1.1$). The average time exponent for all mobile particles ($\alpha > 0.1$) is $\alpha = 0.72$.

ζ & TCRβ diffusion characteristics

	ζ	TCRβ
Labelling strategy	Sir-SNAP	scFv Alexa Fluor 488
Mean diffusion coefficient D [$\mu\text{m}^2/\text{s}$]	0.066 ± 0.004	0.043 ± 0.002
Mean α coefficient	0.61	0.74
Number of tracks	3962	2926
Mean tracks length	15.6	17.7
TCR diffusion	80% mobile ($D_2 \approx 0.093 \pm 0.022 \mu\text{m}^2/\text{s}$) 20% immobile ($D_1 \approx 0.014 \pm 0.003 \mu\text{m}^2/\text{s}$)	68% mobile ($D_2 \approx 0.060 \pm 0.011 \mu\text{m}^2/\text{s}$) 32% immobile ($D_1 \approx 0.017 \pm 0.006 \mu\text{m}^2/\text{s}$)
Diffusion modes		
- Sub-diffusion	76%	69%
- Free (Brownian)	10%	20%
- Directed	14%	11%

Table 5: Diffusion properties of ζ and TCRβ derived from *MSD* and *explot* analysis of trajectories acquired with a t_{lag} of 50ms on Fibronectin coated cover slips.

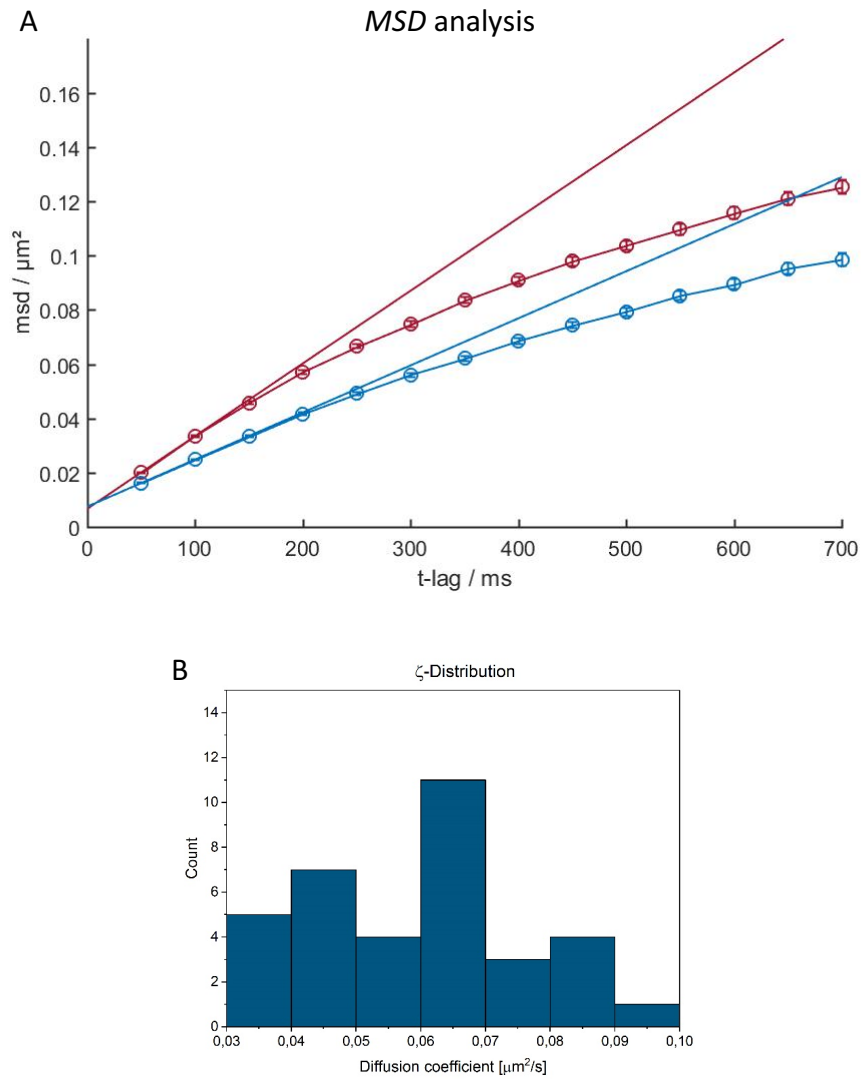


Figure 34: ζ diffusion properties retrieved from tracking experiments on transfected Jurkat T cells labelled with SiR-SNAP. The experiments were performed on glass slides coated with Fibronectin and images were recorded with a time-lag of 50ms. A: Time-averaged ensemble MSD plots of ζ -SiR-SNAP (red) and TCR β (blue) labelled with scFv-AF488. B: Distribution of the diffusion coefficients measured for ζ .

Explot analysis

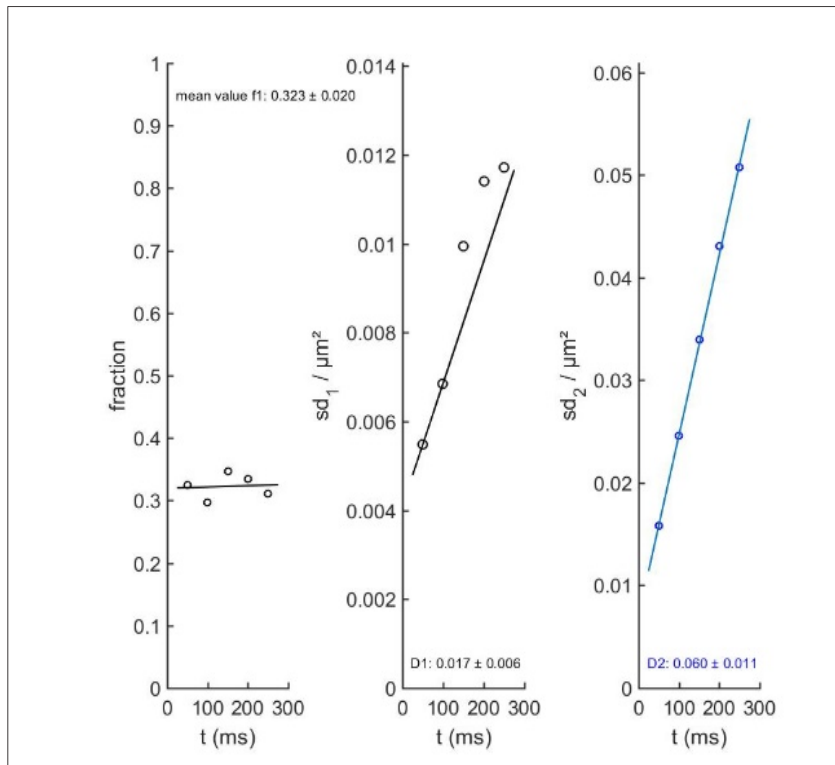
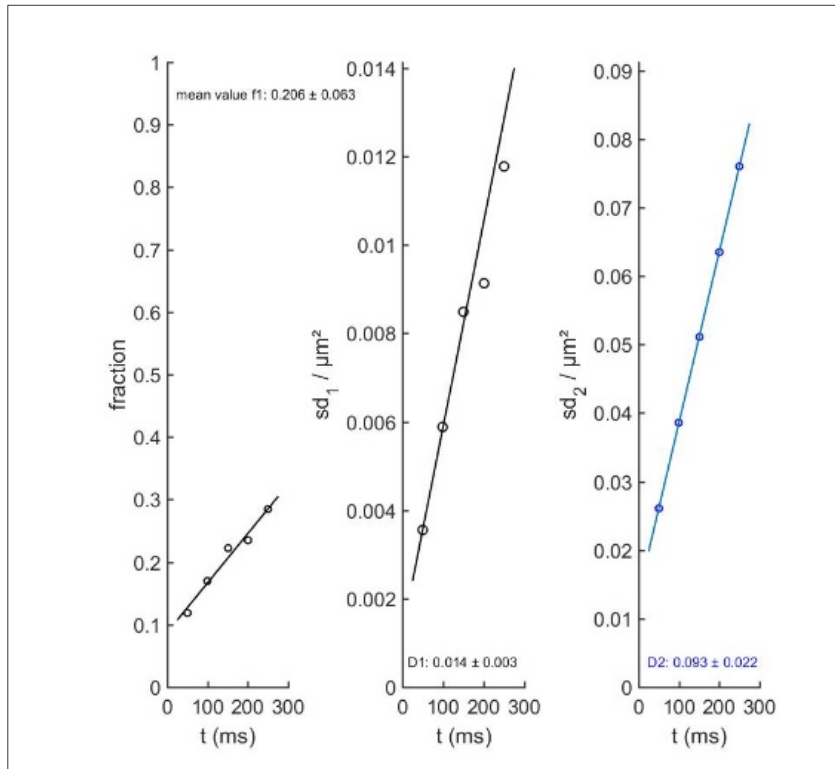


Figure 35: *Explot* analysis of ζ (upper image) and $TCR\beta$ (lower image) diffusion. The plots to the left show the immobile and mobile fractions. The middle and right panels describe the diffusion behaviour of the slower and faster components, respectively.

3.2.2 Micropatterning & FRAP

To study the interaction kinetics between ζ and TCR β within the TCR/CD3-complex, the micropatterning technique was extended with FRAP and the results are showcased in this section.

3.2.2.1 Micropatterning

Micropatterned surfaces were functionalized with α CD3 ϵ antibodies which target the CD3 ϵ domain of the TCR/CD3-complex. Therefore, CD3 ϵ operated as the fixed bait proteins within the patterns and the associated membrane proteins ζ and TCR β were assigned as fluorescently labelled prey.

The micropatterning approach was implemented by using transfected primary murine T cells expressing ζ -GFP and TCR β labelled with scFv-AF647. Control samples for pattern quality, such as shown in Figure 36A, were included in every experiment. The cells were plated on epoxy slides featuring α CD3 ϵ patterns and after 5-10 minutes micropatterns started to form at the plasma membrane which were visualized via TIRF microscopy (Figure 36B-C). The patterns were observed in dual-view mode by applying two color illumination. While patterns were often observed for TCR β (Figure 36B, C), ζ -GFP (Figure 36, D) showed patterns only rarely.

The characteristic pattern caused by the redistribution of fluorescently labelled receptors features bright spots which indicate that there is an interaction between CD3 ϵ (bait) and the patterned α CD3 ϵ antibody, made visible by a strong association of the fluorescently labelled ζ and TCR β (prey) with CD3 ϵ . The micropatterns were quantified by assigning a brightness and normalized contrast value ΔF to each spot [67], as described in the methods (2.5.1).

Normalized contrast values of the pre-bleached images range from ~ 0.5 to ~ 0.7 for both ζ and TCR β . On average, ζ -GFP pattern showed a higher initial contrast (~ 0.7) than TCR β (~ 0.6).

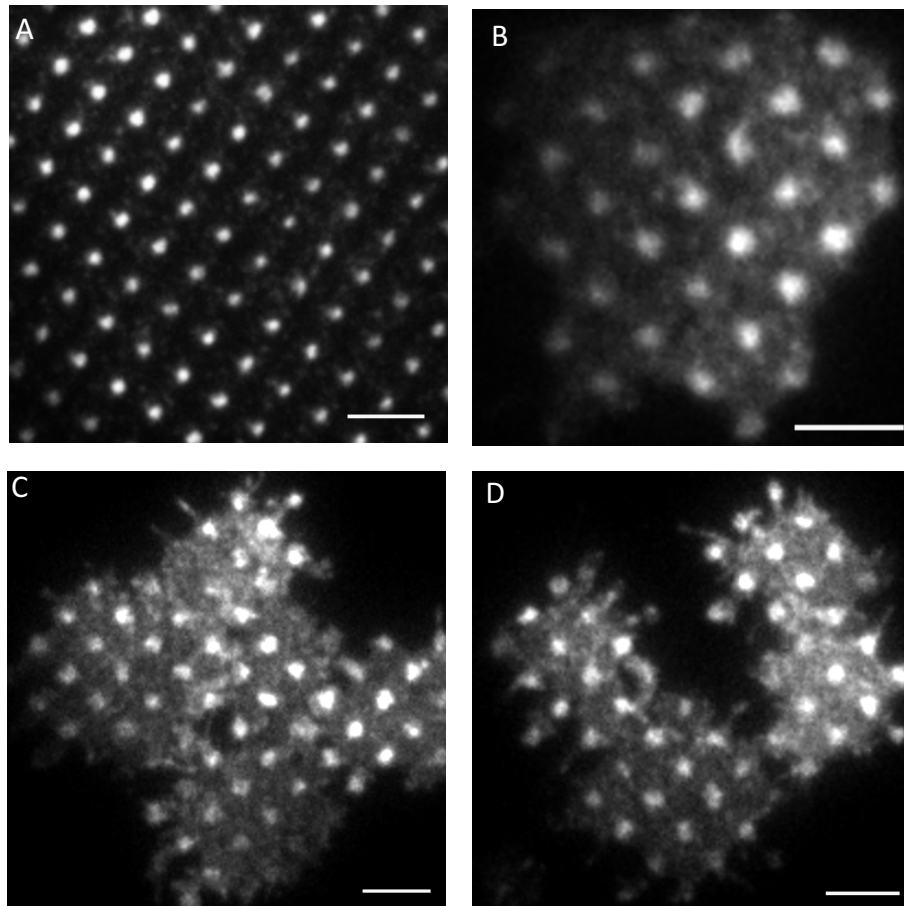


Figure 36: Micropatterning results. Interaction of streptavidin with biotin leads to the formation of antibody structures. Bait-prey interaction leads to an enrichment of fluorescently labelled ζ and $\text{TCR}\beta$ in the patterned spots. Samples were illuminated in TIRF configuration to minimize intracellular fluorescence signal disturbance. A: Control measurement featuring patterned spots which are formed by capturing AF647- labelled goat anti-mouse secondary antibodies on αGFP patterned surfaces. B, C, D: Cells plated on coverslips featuring $\alpha\text{CD3}\epsilon$ patterns which are targeted against the $\text{CD3}\epsilon$ -domain of the $\text{TCR}/\text{CD3}$ complex. B: Micropatterns visualized by blue laser excitation of ζ – GFP. C & D: Micropatterns on cells detected through $\text{TCR}\beta$ labelled with scFv-Alexa 647 by red laser excitation. The scale bar is $5\mu\text{m}$.

3.2.2.2 FRAP

FRAP experiments were performed by closing the aperture, thus, defining areas on the cell membrane which comprise 2-3 spots with high contrast (Figure 37). The selected regions were photobleached according to the protocol described in 2.5 and the recovery in those areas was followed for nearly 1.5 minutes (Figure 37). FRAP data was collected from 15 cells, resulting in more than 30 recorded spots. The TIRF images of the FRAP experiment in Figure 37 show images before, immediately after and 1.5 minutes after bleaching. On the images recorded immediately after photo bleaching ($t= 50 \text{ ms}$) no signal was detected. Within the experimental time scale of 1.5 minutes, a very low relative recovery of $\Delta F \approx 0.06$ was detected for ζ -GFP but no relative recovery was observed for $\text{TCR}\beta$.

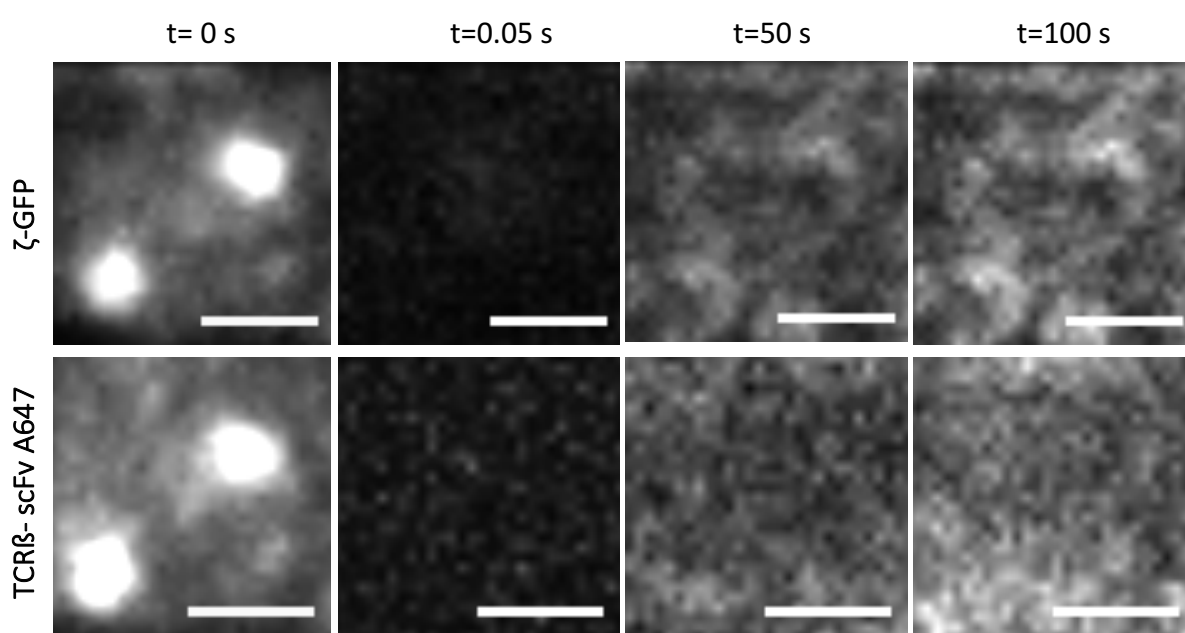


Figure 37: Time-lapse TIRFM images of micropatterns in cells expressing ζ -GFP and $\text{TCR}\beta$ labelled with scFv-Alexa647 were plated on $\alpha\text{CD3}\epsilon$ -antibody coverslips featuring $1\mu\text{m}$ pattern. Individual spots were selected for the FRAP experiments. Here the images show two spots before photobleaching and at the indicated times after photobleaching. Scale bar is $2\mu\text{m}$.

The recovery signal in the patterned spots was analyzed using in-house algorithms implemented in MATLAB as described in 2.5.1. To evaluate the fluorescence at the bait-captured area (F_{on}) above the bait-free area (F_{off}) for both ζ and $\text{TCR}\beta$, the recovery of the relative signals ΔF was plotted over the frame sequences featuring 1000ms time intervals. Figure 38 shows the recovery characteristics for ζ -GFP and $\text{TCR}\beta$ patterns, showing the average recovery of 30 ζ -GFP and $\text{TCR}\beta$ spots.

As depicted in Figure 38 the fluorescence recovery of ζ -GFP and $\text{TCR}\beta$ was slow on CD3 patterned surfaces, suggesting a strong bond of the molecules to the capture CD3 ϵ . Both membrane protein redistributions did not recover within the experimental time frame of 1.5 minutes.

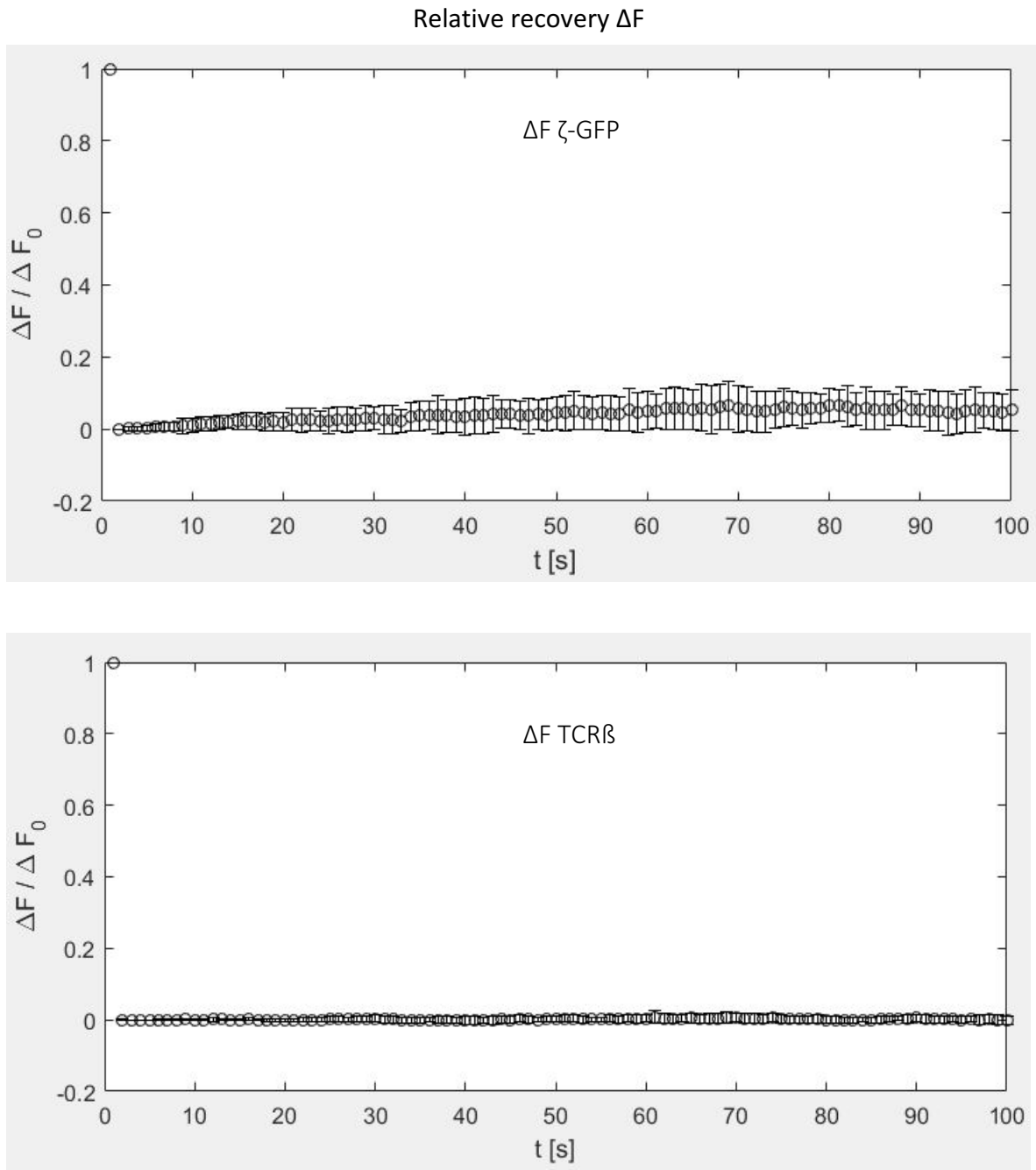


Figure 38: The recovery of the normalized contrast signal $\Delta F = (F_{\text{on}} - F_{\text{off}}) / \Delta F_0$ (y-axis), describing the fluorescence at the bait-captured area (F_{on}) above the bait-free area (F_{off}), was analyzed and plotted over the frame sequence. Post-bleach images were captured in 1000ms intervals, adding up to a total observation time of over 1.5 minutes. The plots present the mean recovery signals taken from 15 cells comprising over 30 spots. Upper plot: $\zeta\text{-GFP}$; lower plot: $\text{TCR}\beta\text{-scFv-AF647}$.

4 Conclusion

4.1 TCR diffusion analysis

4.1.1 Surfaces

The requirement for cells to be attached to an imaging platform for microscopic analysis of the plasma membrane can be met by providing specific adhesion surfaces. Cell membrane experiments are often performed with TIRFM capturing the diffusion on the basal cell membrane, a region which is exposed to the adhesion coating. While certain interactions between the plasma membrane and the adhesion surface are necessary for cell attachment they might also affect membrane protein behavior by causing non-specific binding to the substrate and perturbations in their activity, thereby influencing the obtained diffusion coefficients and mean squared displacements which are important parameters for evaluating protein kinetics ([8], [9]). In this study the quantitative assessment of possible cell-material interactions was achieved by comparing TCR diffusion properties on three commonly used strategies for representing resting T cells on surfaces: Fibronectin (FN), Poly-D-Lysine (PDL) and a supported Lipid Bilayer system (SLB).

The observations made by investigating the diffusional properties of the TCR using TIRFM are summarized in Table 2, showcasing the detected heterogeneity of protein mobility at the plasma membrane of T cells. Analysis of single-molecule trajectories on all adhesion surfaces revealed deviations from free Brownian motion, as indicated by the sub-diffusive trend of the ensemble MSD curves. Evaluation of the time dependence of the MSD for trajectories averaged over individual recordings showed various diffusion modes for TCR mobility, identified as Brownian motion, anomalous sub-diffusion and directed motion. However, the majority of the MSD plots featured a sublinear time dependence, indicating that there is little directed motion of the TCR in the presented T cell experiments. The finding that the diffusion rate decreases with a growing t_{lag} fortifies the existence of anomalous sub-diffusion for TCR mobility.

The heterogeneities in the mobility of the TCR are reflected in the width of the distribution of diffusion and α coefficients. The data shows a variety of α and D values ranging from 0.2 to ~ 1.8 and $0.02 \mu\text{m}^2/\text{s}$ to $0.08 \mu\text{m}^2/\text{s}$, respectively. While many studies suggest that the scatter in D originates from the randomness of a random walk and from interactions with other membrane structures, the varying diffusion rates, especially the slower population, could also originate from interactions of the labelled species with the adhesion surface [120]. For the three adhesion surfaces used in this work *exploT* analysis indicates that most TCRs on the plasma membrane exhibit a two component mobility, featuring a non-negligible slow mobility component ($\sim 30\%$) with a diffusion rate $D_1 \approx 0.015 \mu\text{m}^2/\text{s}$. Zanetti-Domingues et al. [9], have observed non-specific binding of proteins to surface coatings such as Poly-L-

Lysine (PLL) or FN, which would lead to measuring lower diffusion rates and a larger immobile population. Furthermore, Santos et al. [121], reported a perturbing effect of PLL coated surfaces on TCR mobility. According to their research, the positively charged PLL structures completely immobilizes TCRs, measuring a mean diffusion rate of $D = 0.018 \pm 0.01 \mu\text{m}^2/\text{s}$ at the basal membrane versus $D = 0.06 \mu\text{m}^2/\text{s}$ obtained at the apical surface of the T cell membrane, using single-molecule light sheet microscopy (smLSM). These values do not agree with the diffusion rates obtained from TIRF measurements on PDL in this work, yielding $D_1 \approx 0.012 \pm 0.005 \mu\text{m}^2/\text{s}$ for the slower mobility component but $D_2 \approx 0.066 \pm 0.019 \mu\text{m}^2/\text{s}$ for the faster population of acquired trajectories. If the immobilization caused by PLL can be explained by its electrostatic properties, it is difficult to reason why the presented results in this work do not yield the same results for the PDL-coated surface. The chemical difference between PDL and PLL, the first being an artificial product while the latter occurs naturally and is less resistant to enzymatic degradation, could contribute to the different diffusional outcomes [60]. It was also observed that PLL and Fibronectin coatings initiate Ca^{2+} signaling [121], leading to a Ca^{2+} increase that according to Dushek et al. [5], induces a significant decrease of TCR mobility. Supported lipid bilayers act as a more natural adhesion surface for cells and provide the most specific binding for cell attachment, since ICAM-1 specifically targets the integrin LFA-1 found on T cells [65]. However, it has been observed that organic dyes, often used for labelling receptors, can strongly interact with lipid bilayers, influencing receptor dynamics and possibly causing the sub-diffusive behavior observed in this work [10].

Even though the three surfaces show variances in their individual diffusion characteristics, the data indicates similar mean diffusion coefficients of $D \approx 0.045 \mu\text{m}^2/\text{s}$ and a similar mobile fraction ($\sim 70\%$), findings which are in agreement with previous studies ([5], [12]). These observations support the idea that the TCR is mobile on all three surfaces and is therefore not strongly affected by the used coating material. However, the non-negligible immobile fraction ($\sim 30\%$) found for all diffusion measurements and the sublinear behavior of the MSD curves might also originate from interactions with the adhesive surface and therefore a general influence of the adhesive surfaces on the plasma membrane constituents cannot be discarded. The diverse outcomes from different research groups highlights the possible variations in measurements based on the used techniques, suggesting that novel strategies are needed to study membrane dynamics away from adhesion surfaces to ensure unperturbed and comparable results.

4.1.2 Diffusion on the basal and apical membranes of T cells

HiLO tracking experiments were performed to compare the diffusion on the basal and apical cell surface on PDL-coated coverslips. The diffusion characteristics obtained from the HiLO measurements showed a slower mobility than when measuring in TIRF. This might be explained by the diminished z-resolution of HiLO, where assuming two-dimensional (2D) diffusion of 3D data can result in a slower and more confined motion. While measuring in TIRF provided enhanced image quality, the drawbacks of capturing 3D motion in 2D should

also be addressed as the cell membrane imaged on the glass slide is approximated by a plane. However, cell membranes are highly irregular surfaces where proteins are not restricted to the visualized plane but might also diffuse in z-direction. Particles moving away from the focal plane could impose a false confinement to the diffusion results and lead to slower diffusion rates. This problem could be resolved by implementing 3D tracking methods, to visualize protein dynamics away from adhesion surfaces and enabling full access to membrane dynamics [122].

4.1.3 Fluorophores

Apart from important photophysical properties including brightness and photostability, the size, electrostatic charge and hydrophobicity of a fluorophore need to be considered for SPT experiments, as these might cause unwanted interactions with the membrane environment and adhesion surfaces. A high dye net charge could be responsible for charge-based interactions with electrostatic membrane and substrate structures causing possible disturbances in molecule dynamics [48]. Other studies have observed that dyes featuring high degrees of hydrophobicity show increased levels of non-specific binding to substrates, resulting in lower measured values for D [38].

To investigate the effects of fluorophores on TCR mobility, the three chemically different organic dyes Alexa Fluor 488, Alexa Fluor 555 and Abberior STAR 635 have been used as fluorescent conjugates to anti-TCR β -scFv. Focusing on PDL coated substrates, single particle tracking experiments were performed to ascertain the diffusion behavior using fluorophores with different properties (see Table 1).

TCR labelled with scFv-Abberior STAR 635 yielded the highest mean diffusion coefficient ($D=0.051 \pm 0.002 \mu\text{m}^2/\text{s}$), followed by AF488 ($D=0.044 \pm 0.011 \mu\text{m}^2/\text{s}$), both values deviating from the low values obtained with AF555 ($D=0.025 \pm 0.001 \mu\text{m}^2/\text{s}$). Taking a closer look at the individual mobility components, Abberior STAR635 features the highest mobile fraction of $\sim 75\%$ with $D_2 \approx 0.076 \pm 0.021 \mu\text{m}^2/\text{s}$ and also the remaining slower population seems to be less immobile with $D_1 \approx 0.021 \pm 0.006 \mu\text{m}^2/\text{s}$. A fraction of 67% of the TCR visualized through AF488 was observed to have a faster diffusion component with $D_2 \approx 0.066 \pm 0.019 \mu\text{m}^2/\text{s}$ and a slower one with $D_1 \approx 0.012 \pm 0.005 \mu\text{m}^2/\text{s}$, both diffusion rates lower compared to Abberior STAR 635. The TCR diffusion was observed to be most immobile when conjugated to scFv-AF555, characterized by a fast diffusion component of 64% with $D_2 \approx 0.043 \pm 0.018 \mu\text{m}^2/\text{s}$ and an almost completely immobile fraction of 36% described by $D_1 \approx 0.006 \pm 0.003 \mu\text{m}^2/\text{s}$.

The results presented in this work indicate that the other dye conjugates have a lower mobility than Abberior STAR 635, which might be explained by its neutral electrostatic behavior. The Alexa Fluor dyes bear a negative net charge which might cause non-specific electrostatic interaction with positively charged cell structures or even the positively charged PDL ([48], [123]). By implementing techniques to measure protein mobility away

from the coverslip-cell interface, possible interactions of fluorophores with the surface material could be minimized. However, the influence of the heterogeneous cell membrane environment on the fluorophore should still be considered. Therefore, the choice of fluorophore should be considered, as this might affect the dynamic behavior as indicated by the different results obtained in this study.

4.1.4 Label Proteins

Measurements with TCRs labelled with full antibodies conjugated to AF647 revealed similar diffusion characteristics on all three coatings, featuring a slower diffusion compared to scFv, as indicated by the obtained mean diffusion coefficients. The immobile diffusion components are more pronounced on all three surfaces (~36%) with a $D_1 \approx 0.009 \pm 0.004 \mu\text{m}^2/\text{s}$. These observations could reflect the impact of the larger size of the antibody on the TCR movement and its interactions with the surrounding structures, compared to scFv. The conjugated scFv used in this work bind much closer to the membrane than full antibodies and are therefore less likely to affect surfaces interactions.

4.2 Interaction kinetics between TCR β and ζ

A common approach to study the TCR/CD3 complex is through visualization of its subunits, often fusing the ζ chain to a fluorescent protein. This work attempted to study ζ behavior by comparing its diffusion characteristics and interactions with the more stable TCR β unit of the TCR/CD3 complex.

4.2.1 Diffusion analysis

Tracking experiments were performed with transfected Jurkat T cells expressing ζ -SNAP-tag, labelled with SiR-SNAP to ensure ζ tracking and TCR β diffusion was measured on primary T cells labelled with scFv-AF488. MSD analysis revealed a higher mean diffusion rate measured for ζ ($D=0.066 \pm 0.004 \mu\text{m}^2/\text{s}$) than for TCR β ($0.043 \pm 0.002 \mu\text{m}^2/\text{s}$). Studying the distribution of squared displacements shows that ζ features a higher mobile fraction (~80%) with a faster diffusion rate ($D_2 \approx 0.093 \mu\text{m}^2/\text{s}$) than TCR β ($D_2 \approx 0.060 \mu\text{m}^2/\text{s}$). A faster ζ mobility has also been observed in previous studies [12]. MSD analysis further reveals the presence of multiple diffusion modes, highlighting a high sub-diffusive fraction of 76% and mean α coefficient of 0.61.

The observations made by diffusion analysis indicate a more mobile ζ diffusion, hinting to the presence of TCR-independent ζ within the membrane of Jurkat T cells. This assumption is supported by the dynamic differences observed between ζ and TCR β .

The higher and faster mobile ζ population observed in these experiments could be explained by free membrane-bound ζ chains, which are not associated with the TCR/CD3 complex. This

possibility is described in chapter 1.2.2. which also mentions a rapid turnover of ζ independent of the TCR/CD3 complex, hinting to a more dynamic interaction of ζ within the TCR/CD3 complex. Furthermore, electrostatic interactions of the ITAMS found on ζ with the inner leaflet of the membrane could stabilize free ζ within the membrane and thus support the idea of a TCR/CD3-independent ζ [21].

The factors causing possible differences in the interactions and dynamics between the TCR/CD3 subunits may be important for regulating TCR/CD3 stability at the plasma membrane and improving T cell sensitivity to antigen and TCR signal control.

To further investigate the observed differences between the dynamics of the two TCR/CD3 subunits, micro-patterning of CD3 ϵ was performed. Herewith, the interaction between the fixed prey proteins CD3 ϵ and the fluorescently labelled free bait proteins ζ or TCR β was studied.

4.2.2 Micropatterning and FRAP

The characteristic pattern caused by the redistribution of fluorescently labelled receptors features bright spots with contrast values ranging from ~ 0.5 to ~ 0.7 for both ζ and TCR β spots. These results confirm strong interactions between the patterned CD3 ϵ domains (bait) and the fluorescently labelled ζ and TCR β (prey).

Evaluation of the recovery signals of ζ and TCR β in the patterns shows that the pre-bleaching contrast value was not reached within the experimental time frame of 1.5 minutes. This observation indicates the existence of TCR/CD3 complexes with a high stability.

No recovery was observed for TCR β , whereas ζ showed slightly more recovery, which could be explained by the presence of cytosolic ζ -GFP. Alcover et al. [16] found that ζ is more readily observed in endosomal compartments than the other TCR/CD3 subunits and that ζ is in a continuous exchange with the other TCR/CD3 partial complexes, which could also explain the slight recovery. However, the low recovery does not exclude the existence of free membrane-bound ζ , since a high bait-prey surface density and strong bait-prey interactions within the patterns could hinder free membrane-bound ζ to access patterned areas and associate with the proteins.

The experimental time frame in this work was limited by 1.5 minutes. Even though the recovery signal seems constant for TCR β at all times and for ζ after ~ 70 frames, longer observation times could give more information on the interaction kinetics.

The results from the micropatterning and FRAP experiments do not represent or explain the differences found in the diffusion behaviour of the ζ and TCR β chains. Other factors contributing to the discrepancies in mobility should also be considered.

Transfected Jurkat T cells introduce exogenous ζ , which could affect differences in the dynamics. If TCRs are assembled with endogenous ζ , independent ζ -SNAP could be detected within the membrane, resulting in false conclusions concerning TCR/CD3/ ζ mobility.

In addition, differences found in the protein motilities could result from unspecific binding of the SiR-SNAP fluorophore. Unbound fluorophores may diffuse freely in the cytosol, briefly appearing in the focal plane and therefore resulting in misleading fluorescent signals.

The single particle tracking results presented in this work question the stability of the TCR/CD3/ ζ assembly, making it difficult to interpret and validate dynamic properties of the TCR/CD3 retrieved from ζ measurements.

Because the ζ chain is an essential part of the complex for membrane association and for accurate signal initiation, uncertainties in measuring ζ diffusion should be minimized. One approach would be to perform tracking experiments on wild type T cells. However, due to a lack of supply of antibodies against the short extracellular part of the ζ chain this labelling strategy is so far not achievable.

5 List of Figures

Figure 1: Depiction of a full size antibody.....	11
Figure 2: Structure and organization of the TCR/CD3-complex.....	12
Figure 3: Synthesis and assembly of the TCR/CD3-complex on the plasma membrane.	13
Figure 4: T cell activation.....	15
Figure 5: Effects of membrane charges on TCR signalling.....	16
Figure 6: Light microscopy.....	17
Figure 7: Objective numerical aperture comparison.....	18
Figure 8: The principle of fluorescence microscopy.....	19
Figure 9: Comparison of a full antibody and various antibody fragment types.....	22
Figure 10: Direct and indirect labelling of antibodies.....	23
Figure 11: Principle of SNAP-tag.....	23
Figure 12: Illumination techniques.....	25
Figure 13: Schematic representation of the micropatterning principle.....	27
Figure 14: Highly Inclined and Laminated Optical sheet illumination.....	28
Figure 15: Resolution.....	29
Figure 16: Illustration of the plasma membrane environment.....	31
Figure 17: Fluorescence recovery after photobleaching.....	32
Figure 18: Schematic representation of the three main steps in single particle tracking....	33
Figure 19: MSD analysis.....	36
Figure 20: MSD plots for representative types of diffusion in 2D.....	38
Figure 21: Schematic representation of the diverse lateral diffusion modes.....	39
Figure 22: Illustration of the micropatterning protocol.....	44
Figure 23: Evaluation of FRAP recovery signal.....	47
Figure 24: MSD analysis of t_{lag} measurements.....	48
Figure 25: Illustration of the experimental set up for different adhesion coatings.....	49
Figure 26: MSD analysis of diffusion on different adhesion coatings.....	50
Figure 27: Single molecule imaging results on the basal surface of T cells.....	52
Figure 28: Explot analysis of diffusion on different adhesion surfaces.....	53
Figure 29: Illustration of the different labelling strategies.....	53
Figure 30: MSD analysis of tracking experiments using different organic dyes.....	55
Figure 31: MSD analysis comparing antibody and scFv measurements.....	55
Figure 32: MSD analysis with antibody measurements on different surfaces.....	56
Figure 33: HiLO vs TIRF.....	57
Figure 34: ζ diffusion properties.....	60
Figure 35: Explot analysis of ζ and TCR β diffusion.....	61
Figure 36: Micropatterning results.....	63
Figure 37: Time-lapse TIRFM images of micropatterns.....	64
Figure 38: The recovery of the normalized contrast signal $\Delta F=(F_{on}-F_{off})/\Delta F_0$	65

6 References

- [1] M. M. Davis, M. Krosgaard, M. Huse, J. Huppa, B. F. Lillemeier, and Q. Li, "T Cells as a Self-Referential, Sensory Organ," *Annu. Rev. Immunol.*, vol. 25, no. 1, pp. 681–695, Apr. 2007.
- [2] A. Grakoui *et al.*, "The immunological synapse: a molecular machine controlling T cell activation.," *Science*, vol. 285, no. 5425, pp. 221–7, Jul. 1999.
- [3] M. L. Dustin, "The immunological synapse.," *Cancer Immunol. Res.*, vol. 2, no. 11, pp. 1023–33, Nov. 2014.
- [4] M. Frick, K. Schmidt, and B. J. Nichols, "Modulation of Lateral Diffusion in the Plasma Membrane by Protein Density," *Curr. Biol.*, vol. 17, no. 5, pp. 462–467, Mar. 2007.
- [5] O. Dushek *et al.*, "Effects of intracellular calcium and actin cytoskeleton on TCR mobility measured by fluorescence recovery," *PLoS One*, vol. 3, no. 12, pp. 1–7, 2008.
- [6] M. B. M. Meddens, S. de Keijzer, and A. Cambi, "High Spatiotemporal Bioimaging Techniques to Study the Plasma Membrane Nanoscale Organization," in *Fluorescence Microscopy*, Elsevier, 2014, pp. 49–63.
- [7] Y. Golan and E. Sherman, "Resolving mixed mechanisms of protein subdiffusion at the T cell plasma membrane," *Nat. Commun.*, vol. 8, no. May, pp. 1–15, 2017.
- [8] A. M. Santos *et al.*, "Capturing resting T cells: the perils of PLL," *Nat. Immunol.*, vol. 19, no. 3, pp. 203–205, Mar. 2018.
- [9] L. C. Zanetti-Domingues, M. L. Martin-Fernandez, S. R. Needham, D. J. Rolfe, and D. T. Clarke, "A Systematic Investigation of Differential Effects of Cell Culture Substrates on the Extent of Artifacts in Single-Molecule Tracking," *PLoS One*, vol. 7, no. 9, p. e45655, Sep. 2012.
- [10] L. D. Hughes, R. J. Rawle, and S. G. Boxer, "Choose Your Label Wisely: Water-Soluble Fluorophores Often Interact with Lipid Bilayers," *PLoS One*, vol. 9, no. 2, p. e87649, Feb. 2014.
- [11] S. Ono, H. Ohno, and T. Salt0, "Rapid Turnover of the CD3& Chain Independent of the TCR-CD3 Complex in Normal T Cells," *Immunity*, vol. 2, no. 639444, 1995.
- [12] B. Rosboth, "Single-Molecule Analysis of the T Cell Receptor and the zeta -Chain within the Membrane of T Lymphocytes," 2015.
- [13] Janeway CA Jr, Travers P, Walport M, *Immunobiology: The Immune System in Health and Disease.*, 5th ed. Garland Science, 2001.
- [14] M. Johnson, "Antibody Structure and Fragments," *Mater. Methods*, vol. 3, Dec. 2013.
- [15] A. Frenzel, M. Hust, and T. Schirrmann, "Expression of Recombinant Antibodies," *Front. Immunol.*, vol. 4, p. 217, Jul. 2013.
- [16] A. Alcover, B. Alarcón, and V. Di Bartolo, "Cell Biology of T Cell Receptor Expression and Regulation," *Annu. Rev. Immunol.*, vol. 36, no. 1, p. annurev-immunol-042617-053429, 2018.
- [17] M. E. Birnbaum *et al.*, "Molecular architecture of the $\alpha\beta$ T cell receptor-CD3 complex.," *Proc. Natl. Acad. Sci. U. S. A.*, vol. 111, no. 49, pp. 17576–81, Dec. 2014.
- [18] M. Sharpe and N. Mount, "Genetically modified T cells in cancer therapy: opportunities and challenges," *Dis. Model. Mech.*, vol. 8, no. 4, pp. 337–350, Apr. 2015.
- [19] M. E. Call, J. Pyrdol, M. Wiedmann, and K. W. Wucherpfennig, "The Organizing Principle in the Formation of the T Cell Receptor-CD3 Complex," *Cell*, vol. 111, no. 7,

- pp. 967–979, Dec. 2002.
- [20] M. E. Call and K. W. Wucherpfennig, “Molecular mechanisms for the assembly of the T cell receptor-CD3 complex,” *Mol. Immunol.*, vol. 40, no. 18, pp. 1295–305, Apr. 2004.
- [21] K. W. Wucherpfennig, E. Gagnon, M. J. Call, E. S. Huseby, and M. E. Call, “Structural Biology of the T-cell Receptor: Insights into Receptor Assembly, Ligand Recognition, and Initiation of Signaling,” *Cold Spring Harb. Perspect. Biol.*, vol. 2, no. 4, pp. a005140–a005140, Apr. 2010.
- [22] J. Charles A Janeway, P. Travers, M. Walport, and M. J. Shlomchik, “T Cell-Mediated Immunity,” 2001.
- [23] P. E. Love and S. M. Hayes, “ITAM-mediated signaling by the T-cell antigen receptor,” *Cold Spring Harb. Perspect. Biol.*, vol. 2, no. 6, p. a002485, Jun. 2010.
- [24] B. K. Gorentla and X.-P. Zhong, “T cell Receptor Signal Transduction in T lymphocytes,” *J. Clin. Cell. Immunol.*, vol. 2012, no. Suppl 12, p. 5, Oct. 2012.
- [25] ART WEISS LAB, “A sequential model for T-cell activation.” [Online]. Available: <https://artweisslab.ucsf.edu/sequential-model-t-cell-activation>. [Accessed: 26-Apr-2018].
- [26] C. Xu *et al.*, “Regulation of T Cell Receptor Activation by Dynamic Membrane Binding of the CD3 ϵ Cytoplasmic Tyrosine-Based Motif,” *Cell*, vol. 135, no. 4, pp. 702–713, Nov. 2008.
- [27] X. Guo *et al.*, “Lipid-dependent conformational dynamics underlie the functional versatility of T-cell receptor,” *Cell Res.*, vol. 27, no. 4, pp. 505–525, Apr. 2017.
- [28] X. Shi *et al.*, “Ca²⁺ regulates T-cell receptor activation by modulating the charge property of lipids,” *Nature*, vol. 493, no. 7430, pp. 111–115, Dec. 2012.
- [29] Y. Ma, K. Poole, J. Goyette, and K. Gaus, “Introducing Membrane Charge and Membrane Potential to T Cell Signaling,” *Front. Immunol.*, vol. 8, p. 1513, Nov. 2017.
- [30] “Molecular Expressions Microscopy Primer: Anatomy of the Microscope - Infinity Optical Systems Introduction.” [Online]. Available: <https://micro.magnet.fsu.edu/primer/anatomy/infinityintro.html>. [Accessed: 26-Apr-2018].
- [31] “ZEISS Microscopy Online Campus | Microscopy Basics | Fluorescence Microscopy.” [Online]. Available: <http://zeiss-campus.magnet.fsu.edu/print/basics/fluorescence-print.html>. [Accessed: 23-Apr-2018].
- [32] B. Huang, M. Bates, and X. Zhuang, “Super-resolution fluorescence microscopy,” *Annu. Rev. Biochem.*, vol. 78, pp. 993–1016, 2009.
- [33] M. J. Sanderson, I. Smith, I. Parker, and M. D. Bootman, “Fluorescence microscopy,” *Cold Spring Harb. Protoc.*, vol. 2014, no. 10, p. pdb.top071795, Oct. 2014.
- [34] S. W. Hell, “Toward fluorescence nanoscopy,” *Nat. Biotechnol.*, vol. 21, no. 11, pp. 1347–1355, Nov. 2003.
- [35] N. Shanker and S. L. Bane, “Basic Aspects of Absorption and Fluorescence Spectroscopy and Resonance Energy Transfer Methods,” in *Methods in cell biology*, vol. 84, 2008, pp. 213–242.
- [36] T. Ha and P. Tinnefeld, “Photophysics of fluorescent probes for single-molecule biophysics and super-resolution imaging,” *Annu. Rev. Phys. Chem.*, vol. 63, pp. 595–617, 2012.
- [37] M. P. Clausen and B. C. Lagerholm, “The probe rules in single particle tracking,” *Curr. Protein Pept. Sci.*, vol. 12, no. 8, pp. 699–713, Dec. 2011.
- [38] L. C. Zanetti-Domingues, C. J. Tynan, D. J. Rolfe, D. T. Clarke, and M. Martin-

- Fernandez, "Hydrophobic Fluorescent Probes Introduce Artifacts into Single Molecule Tracking Experiments Due to Non-Specific Binding," *PLoS One*, vol. 8, no. 9, p. e74200, Sep. 2013.
- [39] R. Y. Tsien, "THE GREEN FLUORESCENT PROTEIN," *Annu. Rev. Biochem*, vol. 67, pp. 509–44, 1998.
- [40] A. Follenius-Wund *et al.*, "Fluorescent Derivatives of the GFP Chromophore Give a New Insight into the GFP Fluorescence Process," *Biophys. J.*, vol. 85, no. 3, pp. 1839–1850, Sep. 2003.
- [41] "Fluorescent Dyes." [Online]. Available: <https://rockland-inc.com/fluorescent-dyes.aspx>. [Accessed: 26-Apr-2018].
- [42] T. Funatsu, Y. Harada, M. Tokunaga, K. Saito, and T. Yanagida, "Imaging of single fluorescent molecules and individual ATP turnovers by single myosin molecules in aqueous solution," *Nature*, vol. 374, no. 6522, pp. 555–559, Apr. 1995.
- [43] M. Xiao *et al.*, "Rapid DNA mapping by fluorescent single molecule detection.," *Nucleic Acids Res.*, vol. 35, no. 3, p. e16, 2007.
- [44] H. Y. Park, A. R. Buxbaum, and R. H. Singer, "Single mRNA Tracking in Live Cells," in *Methods in enzymology*, vol. 472, 2010, pp. 387–406.
- [45] M. J. Skaug, J. N. Mabry, and D. K. Schwartz, "Single-Molecule Tracking of Polymer Surface Diffusion," *J. Am. Chem. Soc.*, vol. 136, no. 4, pp. 1327–1332, Jan. 2014.
- [46] S. Scheffler, M. Sauer, and H. Neuweiler, "Monitoring antibody binding events in homogeneous solution by single-molecule fluorescence spectroscopy," *Zeitschrift fur Phys. Chemie*, vol. 219, no. 5, pp. 665–678, 2005.
- [47] "Alexa Fluor® Dyes Spanning the Visible and Infrared Spectrum—Section 1.3." [Online]. Available: <http://www.thermofisher.com/at/en/home/references/molecular-probes-the-handbook/fluorophores-and-their-amine-reactive-derivatives/alexa-fluor-dyes-spanning-the-visible-and-infrared-spectrum.html#datatable>. [Accessed: 16-Apr-2018].
- [48] N. Panchuk-Voloshina *et al.*, "Alexa Dyes, a Series of New Fluorescent Dyes that Yield Exceptionally Bright, Photostable Conjugates," *J. Histochem. Cytochem.*, vol. 47, no. 9, pp. 1179–1188, Sep. 1999.
- [49] "Fluorescence Quantum Yields (QY) and Lifetimes (τ) for Alexa Fluor Dyes—Table 1.5e." .
- [50] "Abberior STAR 635." [Online]. Available: <http://www.abberior.com/shop/Labels-by-Application/Confocal-Epi-SIM/Abberior-STAR-635::8.html>. [Accessed: 16-Apr-2018].
- [51] G. Lukinavičius *et al.*, "A near-infrared fluorophore for live-cell super-resolution microscopy of cellular proteins," *Nat. Chem.*, vol. 5, no. 2, pp. 132–139, 2013.
- [52] R. Doshi, B. R. Chen, C. R. T. Vibat, N. Huang, C.-W. Lee, and G. Chang, "In vitro nanobody discovery for integral membrane protein targets," *Sci. Rep.*, vol. 4, no. 1, p. 6760, May 2015.
- [53] "Direct vs indirect immunofluorescence | Abcam." [Online]. Available: <http://www.abcam.com/secondary-antibodies/direct-vs-indirect-immunofluorescence>. [Accessed: 26-Apr-2018].
- [54] G. V. Los *et al.*, "HaloTag: A Novel Protein Labeling Technology for Cell Imaging and Protein Analysis," *ACS Chem. Biol.*, vol. 3, no. 6, pp. 373–382, Jun. 2008.
- [55] X. Sun *et al.*, "Development of SNAP-Tag Fluorogenic Probes for Wash-Free Fluorescence Imaging," *ChemBioChem*, vol. 12, no. 14, pp. 2217–2226, Sep. 2011.
- [56] A. Gautier *et al.*, "An Engineered Protein Tag for Multiprotein Labeling in Living

- Cells," *Chem. Biol.*, vol. 15, no. 2, pp. 128–136, Feb. 2008.
- [57] Kai Johnsson, "SNAP-tag® Technologies: Novel Tools to Study Protein Function | NEB," *NEB expressions vol 3.3*, 2008.
- [58] A. L. Mattheyses, S. M. Simon, and J. Z. Rappoport, "Imaging with total internal reflection fluorescence microscopy for the cell biologist.," *J. Cell Sci.*, vol. 123, no. Pt 21, pp. 3621–8, Nov. 2010.
- [59] "Poly-lysine | Sigma-Aldrich." [Online]. Available: <https://www.sigmaaldrich.com/technical-documents/articles/biofiles/poly-lysine.html>. [Accessed: 21-Apr-2018].
- [60] D. Mazia, G. Schatten, and W. Sale, "Adhesion of cells to surfaces coated with polylysine. Applications to electron microscopy.," *J. Cell Biol.*, vol. 66, no. 1, pp. 198–200, Jul. 1975.
- [61] D. Mazia, G. Schatten, and W. Sale, "Adhesion of cells to surfaces coated with polylysine. Applications to electron microscopy.," *J. Cell Biol.*, vol. 66, no. 1, pp. 198–200, Jul. 1975.
- [62] D. M. Kalaskar, J. E. Downes, P. Murray, D. H. Edgar, and R. L. Williams, "Characterization of the interface between adsorbed fibronectin and human embryonic stem cells.," *J. R. Soc. Interface*, vol. 10, no. 83, p. 20130139, Jun. 2013.
- [63] A. J. García and D. Boettiger, "Integrin-fibronectin interactions at the cell-material interface: initial integrin binding and signaling.," *Biomaterials*, vol. 20, no. 23–24, pp. 2427–33, Dec. 1999.
- [64] T. J. Crites, M. Maddox, K. Padhan, J. Muller, C. Eigsti, and R. Varma, "Supported Lipid Bilayer Technology for the Study of Cellular Interfaces.," *Curr. Protoc. cell Biol.*, vol. 68, p. 24.5.1-31, Sep. 2015.
- [65] M. P. Stewart, C. Cabanas, and N. Hogg, "T cell adhesion to intercellular adhesion molecule-1 (ICAM-1) is controlled by cell spreading and the activation of integrin LFA-1.," *J. Immunol.*, vol. 156, no. 5, pp. 1810–7, Mar. 1996.
- [66] L. Wen-Wen, C. Zhen-Ling, and X.-Y. Jiang, "Methods for Cell Micropatterning on Two-Dimensional Surfaces and Their Applications in Biology.," *CHINESE J. Anal. Chem. Chin J Anal Chem*, vol. 37, no. 377, pp. 943–949, 2009.
- [67] M. Schwarzenbacher *et al.*, "Micropatterning for quantitative analysis of protein-protein interactions in living cells," *Nat. Methods*, vol. 5, no. 12, pp. 1053–1060, 2008.
- [68] A. M. Lipp *et al.*, "Lck Mediates Signal Transmission from CD59 to the TCR/CD3 Pathway in Jurkat T Cells," *PLoS One*, vol. 9, no. 1, p. e85934, Jan. 2014.
- [69] J. Weghuber, "Quantitative Protein-Protein Interaction Detection," *Lab. Journal-Bus. Web Users Sci. Ind.*, 2015.
- [70] "ZEISS Microscopy Online Campus | Microscopy Basics | Numerical Aperture and Resolution." [Online]. Available: <http://zeiss-campus.magnet.fsu.edu/articles/basics/resolution.html>. [Accessed: 23-Apr-2018].
- [71] S. Bliven, "Airy disk spacing near Rayleigh criterion.png - Wikimedia Commons," 2014. [Online]. Available: https://commons.wikimedia.org/wiki/File:Airy_disk_spacing_near_Rayleigh_criterion.png. [Accessed: 23-Apr-2018].
- [72] E. B. Watkins, C. E. Miller, J. Majewski, and T. L. Kuhl, "Membrane texture induced by specific protein binding and receptor clustering: active roles for lipids in cellular function.," *Proc. Natl. Acad. Sci. U. S. A.*, vol. 108, no. 17, pp. 6975–80, Apr. 2011.
- [73] A. D. Douglass and R. D. Vale, "Single-Molecule Microscopy Reveals Plasma

- Membrane Microdomains Created by Protein-Protein Networks that Exclude or Trap Signaling Molecules in T Cells," *Cell*, vol. 121, no. 6, pp. 937–950, Jun. 2005.
- [74] Z. Kalay, "Reaction kinetics in the plasma membrane," *Biotechnol. J.*, vol. 7, no. 6, pp. 745–752, Jun. 2012.
- [75] F. J. Alenghat and D. E. Golan, "Membrane Protein Dynamics and Functional Implications in Mammalian Cells," in *Current topics in membranes*, vol. 72, 2013, pp. 89–120.
- [76] J. H. Jeon, M. Javanainen, H. Martinez-Seara, R. Metzler, and I. Vattulainen, "Protein crowding in lipid bilayers gives rise to non-Gaussian anomalous lateral diffusion of phospholipids and proteins," *Phys. Rev. X*, vol. 6, no. 2, pp. 1–17, 2016.
- [77] M. J. Skaug, R. Faller, and M. L. Longo, "Correlating anomalous diffusion with lipid bilayer membrane structure using single molecule tracking and atomic force microscopy," *J. Chem. Phys.*, vol. 134, no. 21, p. 215101, Jun. 2011.
- [78] V. Horejshi and M. Hrdinka, "Membrane microdomains in immunoreceptor signaling," *FEBS Lett.*, vol. 588, no. 15, pp. 2392–2397, Aug. 2014.
- [79] S. Burov, J.-H. Jeon, R. Metzler, and E. Barkai, "Single particle tracking in systems showing anomalous diffusion: the role of weak ergodicity breaking," *Phys. Chem. Chem. Phys.*, vol. 13, no. 5, p. 1800, Jan. 2011.
- [80] F. Höfling and T. Franosch, "Anomalous transport in the crowded world of biological cells," Jan. 2013.
- [81] P. Lajoie *et al.*, "Plasma membrane domain organization regulates EGFR signaling in tumor cells," *J. Cell Biol.*, vol. 179, no. 2, pp. 341–56, Oct. 2007.
- [82] I. Chung, R. Akita, R. Vandlen, D. Toomre, J. Schlessinger, and I. Mellman, "Spatial control of EGF receptor activation by reversible dimerization on living cells," *Nature*, vol. 464, no. 7289, pp. 783–787, Apr. 2010.
- [83] J. C. den Hartigh, P. M. van Bergen en Henegouwen, A. J. Verkleij, and J. Boonstra, "The EGF receptor is an actin-binding protein," *J. Cell Biol.*, vol. 119, no. 2, pp. 349–55, Oct. 1992.
- [84] Y. Zhou *et al.*, "Membrane potential modulates plasma membrane phospholipid dynamics and K-Ras signaling," *Science (80-.)*, vol. 349, no. 6250, pp. 873–876, Aug. 2015.
- [85] T. K. Fujiwara *et al.*, "Confined diffusion of transmembrane proteins and lipids induced by the same actin meshwork lining the plasma membrane," *Mol. Biol. Cell*, vol. 27, no. 7, pp. 1101–19, Apr. 2016.
- [86] D. Axelrod, D. E. Koppel, J. Schlessinger, E. Elson, and W. W. Webb, "Mobility measurement by analysis of fluorescence photobleaching recovery kinetics," *Biophys. J.*, vol. 16, no. 9, pp. 1055–1069, Sep. 1976.
- [87] D. E. Koppel, D. Axelrod, J. Schlessinger, E. L. Elson, and W. W. Webb, "Dynamics of fluorescence marker concentration as a probe of mobility," *Biophys. J.*, vol. 16, no. 11, pp. 1315–29, Nov. 1976.
- [88] E. Sezgin and P. Schuille, "Fluorescence Techniques to Study Lipid Dynamics," *Cold Spring Harb. Perspect. Biol.*, vol. 3, no. 11, pp. a009803–a009803, Nov. 2011.
- [89] C. De Los Santos, C.-W. Chang, M.-A. Mycek, and R. A. Cardullo, "FRAP, FLIM, and FRET: Detection and analysis of cellular dynamics on a molecular scale using fluorescence microscopy," *Mol. Reprod. Dev.*, vol. 82, no. 7–8, pp. 587–604, 2015.
- [90] A. Dopico, *Methods in membrane lipids*. Humana, 2007.
- [91] J. Lippincott-Schwartz, N. Altan-Bonnet, and G. H. Patterson, "Photobleaching and photoactivation: following protein dynamics in living cells," *Nat. Cell Biol.*, vol.

- Suppl, pp. S7-14, Sep. 2003.
- [92] “frap curves | mybioscience scientific illustrations.” [Online]. Available: <http://mybioscience.org/2013/09/08/frap-images-for-under-pressure-the-cells-response-bsmb-meeting-in-cardiff/frap-curves/>. [Accessed: 23-Apr-2018].
- [93] H. Shen *et al.*, “Single Particle Tracking: From Theory to Biophysical Applications,” *Chem. Rev.*, vol. 117, no. 11, pp. 7331–7376, 2017.
- [94] C. Manzo and M. F. Garcia-Parajo, “A review of progress in single particle tracking: from methods to biophysical insights,” *Rep. Prog. Phys.*, vol. 78, no. 12, p. 124601, 2015.
- [95] X. Michalet, O. H. W. Siegmund, J. V Vallerga, P. Jelinsky, J. E. Millaud, and S. Weiss, “Detectors for single-molecule fluorescence imaging and spectroscopy,” *J. Mod. Opt.*, vol. 54, no. 2–3, p. 239, Jan. 2007.
- [96] K. Ritchie, X.-Y. Shan, J. Kondo, K. Iwasawa, T. Fujiwara, and A. Kusumi, “Detection of non-Brownian diffusion in the cell membrane in single molecule tracking,” *Biophys. J.*, vol. 88, no. 3, pp. 2266–77, Mar. 2005.
- [97] A. Small and S. Stahlheber, “Fluorophore localization algorithms for super-resolution microscopy,” *Nat. Methods*, vol. 11, no. 3, pp. 267–279, Mar. 2014.
- [98] M. Lindén, V. Čurić, E. Amselem, and J. Elf, “Pointwise error estimates in localization microscopy,” *Nat. Commun.*, vol. 8, p. 15115, May 2017.
- [99] A. Shivanandan, H. Deschout, M. Scarselli, and A. Radenovic, “Challenges in quantitative single molecule localization microscopy,” *FEBS Lett.*, vol. 588, no. 19, pp. 3595–3602, Oct. 2014.
- [100] Y. Gao and M. L. Kilfoil, “Accurate detection and complete tracking of large populations of features in three dimensions,” *Opt. Express*, vol. 17, no. 6, pp. 4685–704, Mar. 2009.
- [101] M. Bramehuber and G. J. Schütz, “In Vivo Tracking of Single Biomolecules: What Trajectories Tell Us About the Acting Forces,” Springer, Berlin, Heidelberg, 2012, pp. 293–329.
- [102] X. Michalet, “Mean square displacement analysis of single-particle trajectories with localization error: Brownian motion in an isotropic medium,” *Phys. Rev. E. Stat. Nonlin. Soft Matter Phys.*, vol. 82, no. 4 Pt 1, p. 41914, Oct. 2010.
- [103] H. Qian, M. P. Sheetz, and E. L. Elson, “Single particle tracking. Analysis of diffusion and flow in two-dimensional systems,” *Biophys. J.*, vol. 60, no. 4, pp. 910–21, Oct. 1991.
- [104] S. Wieser and G. J. Schütz, “Tracking single molecules in the live cell plasma membrane—Do’s and Don’t’s,” *Methods*, vol. 46, no. 2, pp. 131–140, 2008.
- [105] S. Wieser, M. Moertelmaier, E. Fuertbauer, H. Stockinger, and G. J. Schütz, “(Un)confined diffusion of CD59 in the plasma membrane determined by high-resolution single molecule microscopy,” *Biophys. J.*, vol. 92, no. 10, pp. 3719–3728, 2007.
- [106] E. Kepten, A. Weron, G. Sikora, K. Burnecki, and Y. Garini, “Guidelines for the Fitting of Anomalous Diffusion Mean Square Displacement Graphs from Single Particle Tracking Experiments,” *PLoS One*, vol. 10, no. 2, p. e0117722, Feb. 2015.
- [107] G. J. Schütz, H. Schindler, and T. Schmidt, “Single-molecule microscopy on model membranes reveals anomalous diffusion,” *Biophys. J.*, vol. 73, no. 2, pp. 1073–80, Aug. 1997.
- [108] A. Kusumi and Y. Sako, “Cell surface organization by the membrane skeleton,” *Curr. Opin. Cell Biol.*, vol. 8, no. 4, pp. 566–74, Aug. 1996.

- [109] T. Fujiwara, K. Ritchie, H. Murakoshi, K. Jacobson, and A. Kusumi, "Phospholipids undergo hop diffusion in compartmentalized cell membrane.," *J. Cell Biol.*, vol. 157, no. 6, pp. 1071–81, Jun. 2002.
- [110] M. J. Saxton, "Anomalous diffusion due to binding: a Monte Carlo study.," *Biophys. J.*, vol. 70, no. 3, pp. 1250–62, Mar. 1996.
- [111] T. J. Feder, I. Brust-Mascher, J. P. Slattery, B. Baird, and W. W. Webb, "Constrained diffusion or immobile fraction on cell surfaces: a new interpretation.," *Biophys. J.*, vol. 70, no. 6, pp. 2767–73, Jun. 1996.
- [112] A. Kusumi, Y. Sako, and M. Yamamoto, "Confined lateral diffusion of membrane receptors as studied by single particle tracking (nanovid microscopy). Effects of calcium-induced differentiation in cultured epithelial cells.," *Biophys. J.*, vol. 65, no. 5, pp. 2021–40, Nov. 1993.
- [113] P. R. Smith, I. E. Morrison, K. M. Wilson, N. Fernández, and R. J. Cherry, "Anomalous diffusion of major histocompatibility complex class I molecules on HeLa cells determined by single particle tracking.," *Biophys. J.*, vol. 76, no. 6, pp. 3331–44, Jun. 1999.
- [114] W. S. Pear, G. P. Nolan, M. L. Scott, and D. Baltimore, "Production of high-titer helper-free retroviruses by transient transfection.," *Proc. Natl. Acad. Sci. U. S. A.*, vol. 90, no. 18, pp. 8392–6, Sep. 1993.
- [115] S. Zhong, K. Malecek, A. Perez-Garcia, and M. Krogsgaard, "Retroviral Transduction of T-cell Receptors in Mouse T-cells," *J. Vis. Exp.*, no. 44, Oct. 2010.
- [116] A. Arnold, "Probing the Plasma Membrane Organization at the Nanoscale," Johannes Kepler Universität Linz, 2015.
- [117] L. Hille, "Aufbau eines Einzelmolekülfluoreszenzmikroskops," Wien, Techn. Univ., Dipl.-Arb., 2015, 2014.
- [118] M. Ovesný, P. Křížek, J. Borkovec, Z. Švindrych, and G. M. Hagen, "ThunderSTORM: a comprehensive ImageJ plug-in for PALM and STORM data analysis and super-resolution imaging," *Bioinformatics*, vol. 30, no. 16, pp. 2389–2390, Aug. 2014.
- [119] A. Reismann, "Einzelmolekulare Analyse des MDR 1-medierten Substrattransportes.," 2013.
- [120] M. J. Saxton, "Single-particle tracking: The distribution of diffusion coefficients," *Biophys. J.*, vol. 72, no. 4, pp. 1744–1753, 1997.
- [121] A. M. Santos *et al.*, "Capturing resting T cells: the perils of PLL," *Nat. Immunol.*, vol. 19, no. 3, pp. 203–205, Mar. 2018.
- [122] A. K. Gustavsson, P. N. Petrov, M. Y. Lee, Y. Shechtman, and W. E. Moerner, "3D single-molecule super-resolution microscopy with a tilted light sheet," *Nat. Commun.*, vol. 9, no. 1, pp. 1–8, 2018.
- [123] S. Mahmudi-Azer, P. Lacy, B. Bablitz, and R. Moqbel, "Inhibition of nonspecific binding of fluorescent-labelled antibodies to human eosinophils.," *J. Immunol. Methods*, vol. 217, no. 1–2, pp. 113–9, Aug. 1998.
- [124] "Detection Methods." [Online]. Available: <http://www.bio-rad.com/de-at/applications-technologies/detection-methods?ID=LUSQ6KKG4>. [Accessed: 14-Apr-2018].
- [125] M. Tokunaga, N. Imamoto, and K. Sakata-Sogawa, "Highly inclined thin illumination enables clear single-molecule imaging in cells," *Nat. Methods*, vol. 5, no. 2, pp. 159–161, Feb. 2008.
- [126] G. Karp, *Cell an Molecular Biology*, 5th ed. John Wiley & Sons, 2008.

